ADVANCED FLOW LITHOGRAPHY AND BARCODED PARTICLES

by

KI WAN BONG

B.S. Chemical and Biological Engineering, Seoul National University (2006)

Submitted to the Department of Chemical Engineering
in partial fulfillment of the requirements for the degree of

Doctor of Philosophy in Chemical Engineering

at the

MASSACHUSETTS INSTITUTE OF TECHNOLOGY

June 2012

Signature of Author_____
Department of Chemical Engineering
May 15, 2012

Certified by_____
Patrick S. Doyle
Professor of Chemical Engineering
Thesis Supervisor

Accepted by_____
Patrick S. Doyle
Professor of Chemical Engineering
Chairman, Department Committee on Graduate Students

Abstract

Advanced Flow Lithography and Barcoded Particles

by
Ki Wan Bong

Submitted to the Department of Chemical Engineering on May 15th, 2012,
in partial fulfillment of the requirements for the degree of
Doctor of Philosophy in Chemical Engineering

Anisotropic multifunctional particles have drawn much attention, leading to wide ranges of applications from biomedical areas to electronics. Despite their enormous potentials, particles with geometrically and chemically complex patterns are not widely used because existing methodologies have limitations in large scale, facile production and suffer from constraints of functionality and morphology. For example, the geometries of multifunctional particles prepared by liquid-phase particle synthesis have been mainly restricted to spheres, deformed spheres, or cylinders. This geometrical restriction has resulted from the tendency of liquid systems to adopt arrangements that minimize surface energy. Although template-assisted particle fabrication can overcome this, these methods are largely ineffective at producing particles with chemical anisotropy or patterning, as the precursor liquid is simply isolated in a non-wetting template and then crosslinked *in situ*. Currently, a technique that can provide both geometrical and chemical complexities to particles has been missing.

Distinguished with the above techniques, flow lithography (FL) has been emerging as a powerful synthesis tool that enables the creation of microparticles with complex morphologies and chemical patterns. Combining photolithography with microfluidic methods, FL has provided precise control over particle size, shape, and chemical patchiness. However, in the primitive versions of FL, particle geometry and chemical patterning has been restricted to 2D and 1D, respectively. Also, these techniques have required the use of polydimethylsiloxane (PDMS) devices, greatly limiting the range of precursor materials which can be processed in FL. Here, we present advanced flow lithography to achieve much higher degree of geometrical and chemical complexity than before. For example, lock release lithography (LRL) can be used to introduce three-dimensional (3D) morphologies, and provide chemical anisotropy in the x-y dimensions (in-plane dimensions) of particles. Also, hydrodynamic focusing lithography (HFL) was developed to offer z-directional (particle height direction) chemical anisotropy to particles. Lastly, oxygen-free flow lithography was a technique designed to extend current PDMS-based FL to any kinds of devices and allow for the creation of particles from previously inaccessible reagents such as organic solvents.

In this thesis, we have also demonstrated advanced barcoded particles as one application of advanced flow lithography. Previously, barcoded hydrogel particles were created as a promising diagnostic tool for high-throughput screening and multiplexed detection of biomolecules. Utilizing advanced flow lithography, we have added advanced functions to the hydrogel particles introducing magnetic beads, tri-layered structures or near-infrared sensing materials. As the first advanced barcoded particles, we present magnetic barcoded hydrogel particles that had led to practical applications in the efficient orientation and separation of the barcoded particles. Also, we show reinforced barcoded particles that combine the usually orthogonal characteristics of an open porous capture region for biomolecule detection with strong structural properties that resist deformation in flow. Finally, we demonstrate near-infrared barcoded particles which can exhibit label-free and real time detection of target molecules.

Thesis Supervisor: Patrick S. Doyle

Title: Professor of Chemical Engineering

Acknowledgments

It was a great fortune for me to meet Prof. Doyle as a research advisor. First of all, he has encouraged my naïve ideas and developed the ideas to systematic research projects. His encouragements have made me to think more creatively. Also, he has guided my researches towards quantitative ways which PhD students should bear in mind. Following his advices, I have experienced how rough ideas are changed to robust research papers, and sharpened my research attitudes for scientific problems. Furthermore, whenever I need his advices, he has set up immediate meetings and provided valuable comments. This is the care that I was eager to receive in PhD course. Lastly, he has been a warm and humane advisor to me. In particular, I deeply appreciated his great supports on my next career. On these reasons, I want to express my foremost thanks to my advisor, Prof. Patrick S. Doyle.

My committee members were Prof. T. Alan Hatton and Prof. Ned Thomas. In past 5 years, both of professors have inputted many scientific and precious comments on my researches. I thank Prof. Hatton about that he has been warm and generous to me. His door has been always opened when I need helps. I also thank Prof. Thomas about that he has actively discussed with me about my carrier goals. In spite of his busy schedules as Engineering Dean, he has considered my committee meetings as important as his official works. Again, I would express deep thanks to both of professors.

My undergraduate advisor, Prof. Hong H. Lee at Seoul National University, has also been a great mentor for my graduate life. I sincerely appreciate his cares, advices and encouragements.

I would like to also thank the Doyle group members. First, I cannot thank Steve Chapin enough. As a modest and steadfast friend, he has provided innumerable helps on research and sincere consultations for my PhD life. It was a cherishable moment to me that we encouraged each other in Nashville, Groningen, and Seattle conferences. Dan Pregibon

has been a kind, optimistic, and creative friend. I am very thankful for his devoted efforts in working with me and socializing me. I still remember when we sang a song together in his house. Priyadarshi Panda has thankfully taken charge of my refreshment and relax. We have also enjoyed doing experiments together on many nights. Jason Rich is my English teacher. Also, he has been a valued friend to share difficulties in both research and life. Sukyung Suh and Nakwon Choi are Korean lab mates who have exchanged useful information and discussions. Our main discussion areas were magnetic particles, electronics, and future life. Jing Tang is a dinner mate. We have sought to find good restaurants that satisfy our fastidious tastes. Isabelle Adrianssens is my first and last UROP. It was great experience for me to work with such a talented and nice woman. I would also express thankfulness to William Uspal (my kind neighbor), Harry An (2nd bay warrior), Rathi Srinivas, Ben Renner (CNN news teacher), Ramin Haghgooie, and Matt Helgeson for their supports and helps. As collaborators, I further thank Sunggap Im, Jingjing Xu, and Jongho Kim. By virtue of their efforts, our collaborations have successfully come to fruition.

On a personal front, I would thank Korean Community at MIT. Taeho Shin, Jongnam Park, Seungwoo Cho, Daeyeon Lee, Jonghoon Choi, Changhoon Lim, Jumin Kim, Wonjae Choi, Yoonsung Nam, Jujin Ahn, Sunyoung Lee, Changyoung Lee, Yongku Cho, Jungah Lee, Daekun Hwang, Younjin Min, Kyungsuk Yum, Jaehee Han, Changsik Song, Woojae Kim, Byungsoo Kim, Sanghwal Yoon, Taeseok Moon, Gwanggyu Kim, Youngseok Kim, and Hyunmin Lee have provided grateful cares to me as senior students. Also, Seungwoo Lee, Tekhyung Lee, Seokjoon Kwon, Hyekyung Noh, Eunjee Lee, Jeongwoo Han, Youjin Lee, Bobae Lee, Jinyoung Baek, Wookeun Chung, Hyomin Lee, Jiyeon Yang, Dongsook Chang, Juhyun Song, Jouha Min, Youngwoo Son, Naeri Ohn, Siwon Choi, Jiyoung Ahn, Jongmi Lee, Yongjin Sung, Yanghyo Kim, Jinkee Hong, Jeonggon Son, Younkyung Baek, Jeonghwan Jeon, Kyungsun Son, Jongmin Lim, Seungkon Lee, Heechul Park, Kyoochul Park, and Jaejin Kim have shared their valuable times with me. I would further thank international friends at MIT. Joshua Middaugh, Wuisiew Tan, Jessie Wong, Christina Lewis, Ying Diao, Adebola Ogunniyi, Qing Han, Shreerang Chhatre, Byron Masi, Pedro Valencia, and Adel Ghaderi have thankfully given constant friendship.

I also acknowledge the following financial supports for the research projects described in this thesis: KwanJeong Educational Foundation, the Singpore-MIT Alliances, NSF, the MIT Deshpande Center, NIBIB, and NIH.

Finally, I should say that it would not be possible to finish this PhD journey without endless love and dedications of my parents (Won Sik, Bong and Young Ok, Park). Also, I should mention that my younger brother (Ki Tae, Bong) have greatly supported me during past 5 years. I will miss that we performed experiments together at MIT for a few months. I truly thank my family and hope them to be always healthy and happy.

Table of Contents

List of Figures

List of Tables

Chapter 1

Introduction

Recently, flow lithography (FL) has emerged as a promising way to prepare complex anisotropic particles, combining photolithography with microfluidic-based methods. This thesis is focused on the developments of advanced flow lithography to achieve much higher degree of geometrical and chemical complexity of particles than the primitive versions of FL. Also, advanced barcoded particles are proposed as a demonstrative application of the new techniques.

1.1 Anisotropic Multifunctional Particles

Anisotropic multifunctional particles hold great potentials in drug delivery [1-3], tissue engineering [4-6], sorting media [7-9], smart materials [10-15], optics [16], microelectromechanical systems [17-19], and building blocks [20-22] for self-assembled, dynamic structures with complex functionality. One of the simplest multifunctional particles is spherical Janus particles. As inferred from Janus, the name which means two-faced Roman god, the particles have two compartments of distinct chemical or physical properties. Although the form is simple, the spherical Janus particles have yielded entirely different applications that homogeneous microspheres cannot reach to. A simple example is Janus microspheres that have hydrophobic and hydrophilic surfaces. Once these particles can be spread out on the water, the hydrophilic regions are dipped into water leading to face-up of hydrophobic areas. Then, the hydrophobic coated area can provide so-called 'lotus effect' of antifogging and self-cleaning, and be used for the preparation of superhydrophobic

films on car or building windows [23]. Another example is dichromatic Janus microspheres. These particles can be electrically or magnetically controlled for face-up direction, and used as pixels of flexible bead displays or papers [24, 25]. Janus microspheres were also of interest in assembly as anisotropic building blocks [26-30]. Furthermore, the particles can be used for optical probes [31] and self-propulsion [32, 33].

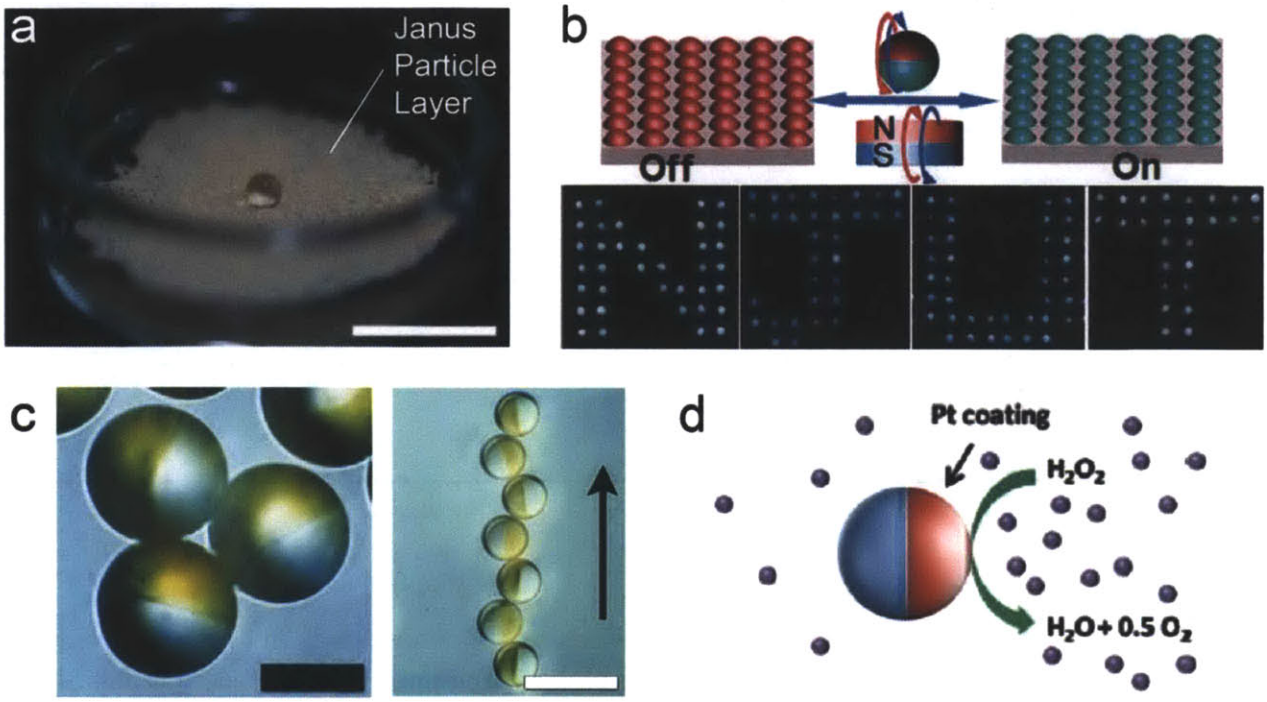

Figure 1.1: *Applications of spherical Janus particles (a) Water-repellent Janus microspheres. The particles were used to form a super-hydrophobic monolayer on water. Then, a water droplet was sitting on the layer. The Image was adapted from ref. 23. (b) Bicolored Janus microspheres. By varying the direction of an external magnetic field, the orientations of Janus particles were changed switching fluorescent signals. The particles can be used for magnetoresponsive bead display. Images adapted from ref. 25. (c) Magnetic Janus microspheres. The particles were self-assembled in Zig-Zag structures in response to in-plain magnetic fields. Images adapted from ref. 30. (d) Self-propelling Janus microspheres. The particles get propulsion force from uneven degradation rates of hydrogen peroxide. The image was adapted from ref. 31. Scale bars are 1 cm (a), 25 μm (c, left) and 100 μm (c, right).*

When physical or chemical structures of particles are getting complex, other interesting applications can emerge. Gracius and co-workers have used geometrically and chemically patterned particles to create 3D electronic circuits that had not been achieved with any other methods [34]. Using particle self-folding, his group also developed micro-grippers to capture targets [11, 35, 36] or micro-containers to load cells [37, 38]. The entities-loaded particles were further traveled to the final destination by the remotely controlled electromagnetic field [11, 36, 37]. When such complex particles hold even biocompatibility,

they can be used for new applications for the biomedical areas such as diagnostics, therapeutics and imaging. One example can be anisotropic building blocks which are patterned with different cell lines for tissue engineering [39-41].

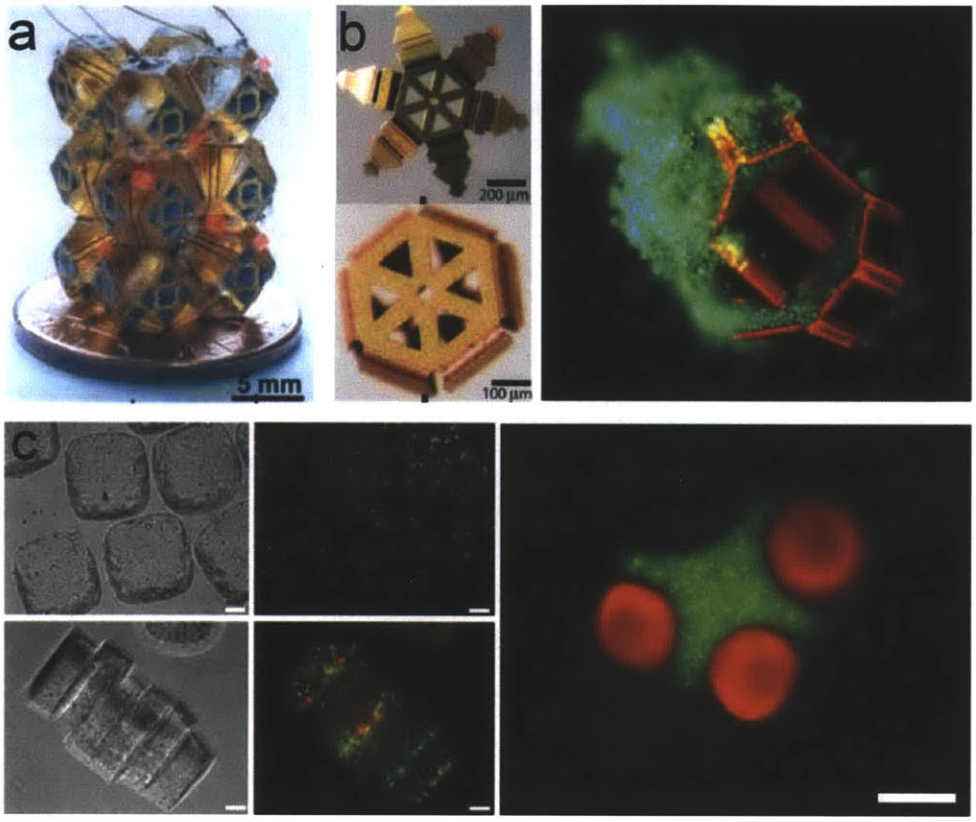

Figure 1.2: *Applications of anisotropic multifunctional particles (a) 3D electronic circuits. The structure was created from the assembly of truncated octahedron particles. The Image was adapted from ref. 34. (b) Micro-grippers. The particles can catch and release target entities by chemically or thermally triggered actuation. The right fluorescent image shows that a micro-gripper locomote gripping samples. Images adapted from ref. 11 and 35. (c) Bottom-up assembly of cell-laden anisotropic particles. The building blocks were assembled into the multi-component constructs by hydrophobic interaction. Images adapted from ref. 39. Scale bars are 100 µm (c, left 4 images) and 200 µm (c, right).*

1.2 Current Methodologies

The enormous potentials of anisotropic multifunctional particles have inspired scientists to develop various fabrication methods. Complex 3D particles can be synthesized using multi-photon fabrication [42-46]. With 100 nm feature resolution, the technique has provided precise control over particle geometry in all dimensions. Unfortunately, the synthetic way has not been widely used for mass-production of 3D particles as the technique is prohibitively time consuming. To partially overcome this, it has been used to generate masters for soft-molding [45].

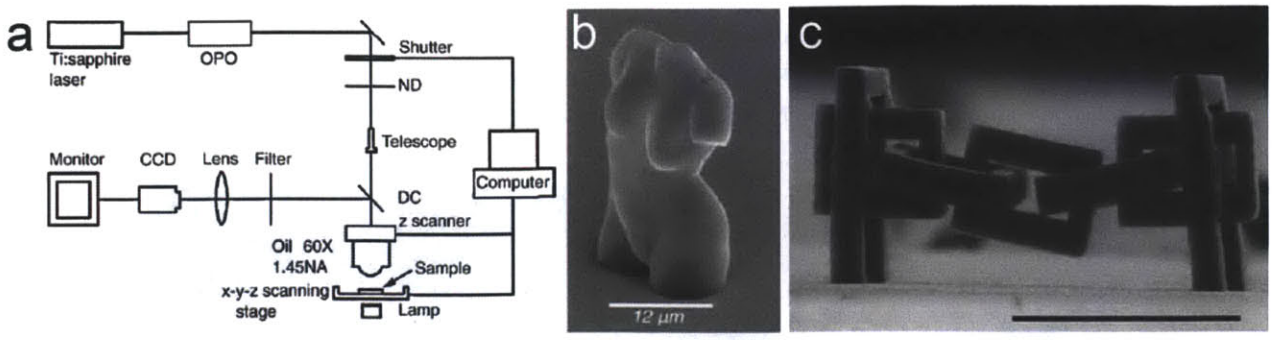

Figure 1.3: *3D particle synthesis (a) A schematic depicting experimental setups for two-photon lithography. Figure adapted from ref. 44. (b) Venus Statue. The micro-statue was fabricated using the setup in (a). Image adapted from ref. 44. (c) Inter-locking chain. The micro-chain was fabricated from multi-photon absorption fabrication. Images adapted from ref. 43. Scale bar is 100 μm (c).*

Anisotropic particles could be also introduced by off-wafer fabrication [47-49]. The advantage of this process is the high-throughput synthesis of particles at a rate of 10^8 particles/min. However, the use of photoresist materials renders this approach suboptimal for many biological applications. In addition, the layer by layer process makes the chemical patterning limited to layered motifs. Alternatively, template-assisted particle fabrication [50-52] could be used to create geometrically complex particles with sub-micrometer dimensions. Unfortunately, this method is largely ineffective at producing particles with chemical anisotropy or patterning, as the precursor liquid is simply isolated in a non-wetting template and then crosslinked in situ. Although one-dimensional striped particles have been generated [53], the synthesis requires complex steps including multiple evaporation-refilling-crosslinking procedures, and the process cannot be applied to non-volatile precursors.

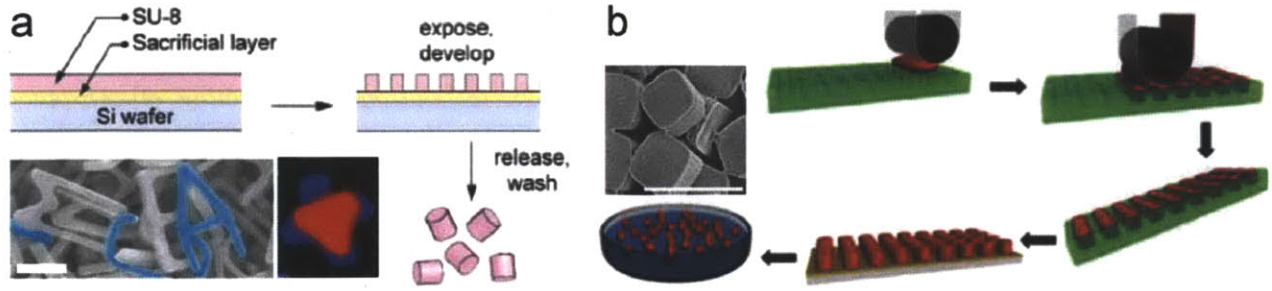

Figure 1.4: *Mass-production of anisotropic particles (a) Off-wafer synthesis. The schematic describes the fabrication process. Inserted images show micro-alphabets and layered composite particles. Figures adapted from ref. 48 and 49. (b) PRINT fabrication. The schematic describes the PRINT process. Inserted image shows micro-cubes. Figures adapted from ref. 51 and 52. Scale bars are 3 μm.*

Other liquid-phase particle synthesis methods have had limited success in creating geometrically and chemically anisotropic particles due to the tendency of liquid systems to

adopt arrangements that minimize surface energy. In current liquid-based methods such as batch nucleation [54], emulsification [55], microreactor production [56, 57], droplet-based microfluidics [24, 58-61], droplet template fabrication [62, 63], co-jetting [64], and microcutting [65], the particle geometries have been restricted to spheres, deformed spheres, or cylinders.

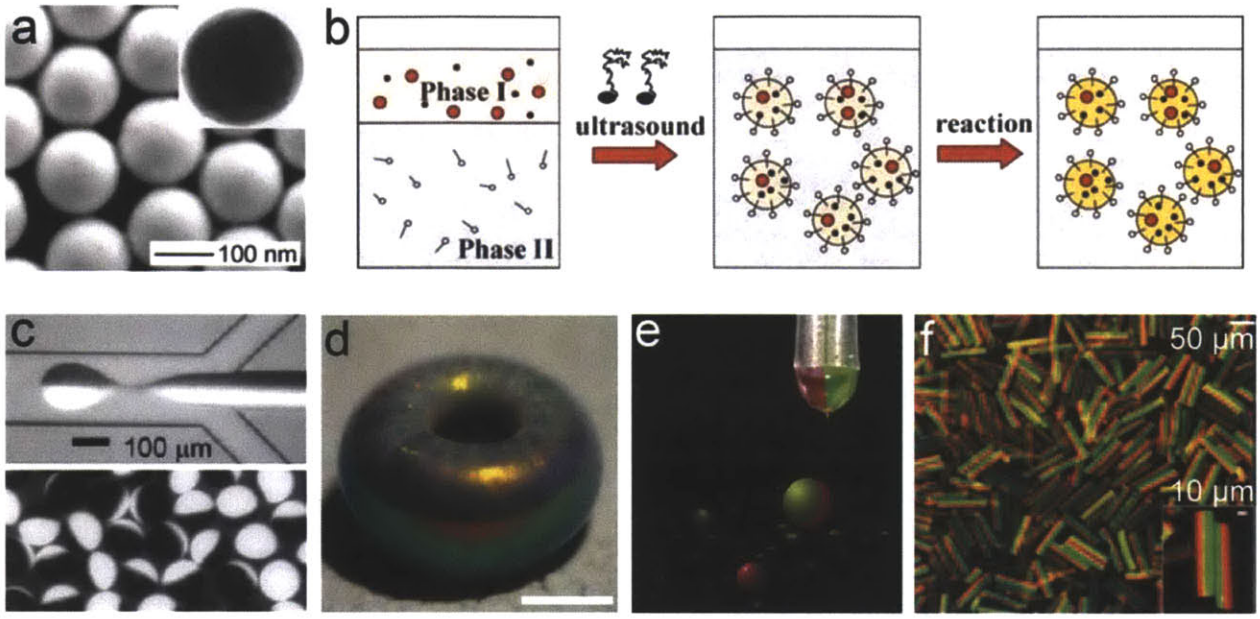

Figure 1.5: *Other liquid-phase synthesis methods (a) SEM and TEM images of nanoparticles synthesized from batch nucleation. Images adapted from ref. 54. (b) A schematic depicting the emulsification process. Figure adapted from ref. 55. (c) Droplet-based microfluidics. Images adapted from ref. 24. (d) An optical image for a micro-doughnut particle prepared by the droplet-template fabrication method. Image adapted from ref. 63. (e) Electro-jettting fabrication for the synthesis of Janus nanoparticles. Figure adapted from ref. 64. (f) Micro-cylinders prepared by micro-cutting fabrication route. Images adapted from ref. 65. Scale bar is 500 μm (d).*

1.3 Flow Lithography

Microfluidic methods provide a flexible toolset for patterning precursor liquids in the synthesis process. The low Reynolds number regime of microfluidic devices offers several advantages that can be exploited for the generation of nano- and microparticles [66, 67]. Complex laminar flow patterns can easily be established in microfluidic channels without the need for physical separators, enabling a range of applications that cannot be achieved with more traditional liquid handling technologies [68-71]. Flow lithography (FL) is a versatile technique that combines photolithography with the capabilities of microfluidic methods for the high-fidelity synthesis of anisotropic gel microparticles [72, 73]. In this technique, photomask-defined shapes can be rapidly printed onto monomer flows, providing precise control over particle size, geometry, and chemical patchiness.

1.3.1 Continuous Flow Lithography (CFL)

In CFL, the first form of flow lithography, mask defined shapes are patterned into a continuously flowing photo-polymerizable monomer stream [72]. The technique can fabricate virtually any two-dimensional particle by simple mask exchanges. The nexus of this technique is the lubrication layer (~1um thick) which is induced by atmospheric oxygen diffusing in through the porous PDMS and locally inhibiting polymerization. By virtue of this layer, particles formed via photo-polymerization are advected through unpolymerized prepolymer liquids without sticking to the PDMS walls.

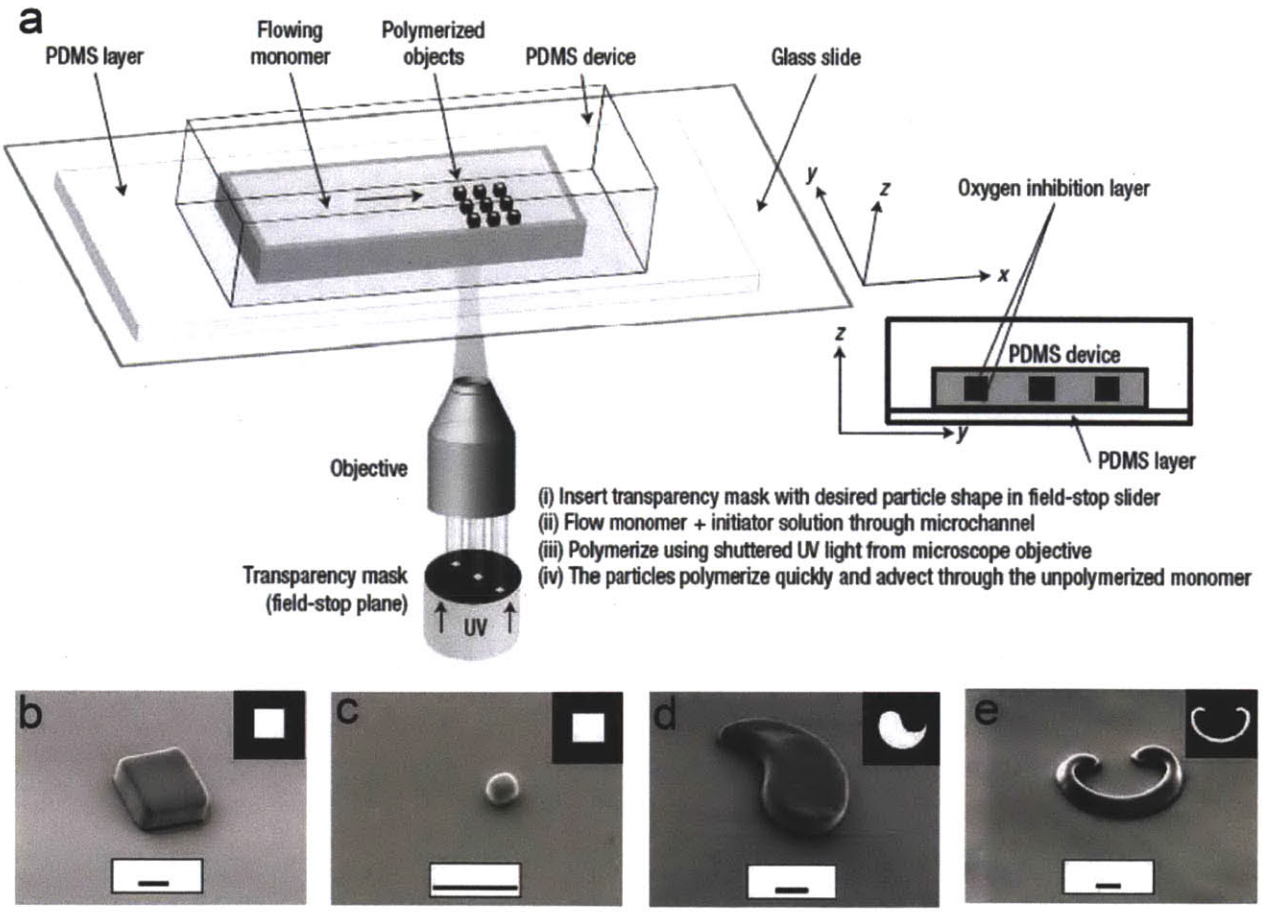

Figure 1.6: *Continuous Flow Lithography (CFL) (a) A schematic diagram of CFL process. (b) – (e) Differential Interference Contrast (DIC) images of various microparticles prepared by CFL. Scale bars are 10 um. Figures adapted from ref. 72.*

In co-flowing laminar streams, CFL can be also used to generate multifunctional particles. Figure 1.7a shows the schematic diagram for synthesis of Janus particles. The widths of the streams in Figure1.7a can be altered by changing the flow rates of the streams, controlling

over both functional areas. However, particles with arbitrary chemical patterns cannot be achieved by CFL because the chemical patterning relies on stream lines (Fig. 1.7c).

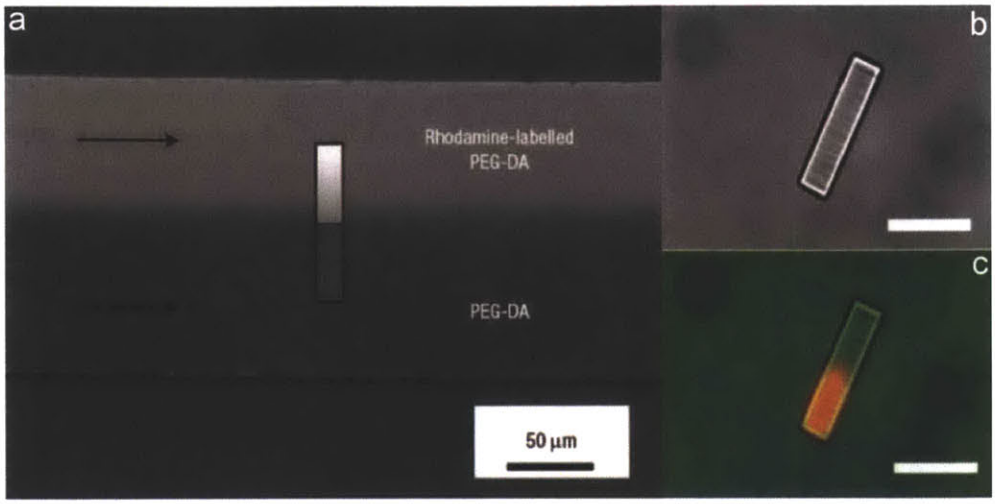

Figure 1.7: *Synthesis of Janus particles (a) A schematic diagram showing the CFL process for the synthesis of Janus particles. (b) - (c) DIC and fluorescent images of a Janus particle synthesized in the process (a). Scale bars are 100µm. Figures adapted from ref. 72.*

1.3.2 Stop Flow Lithography (SFL)

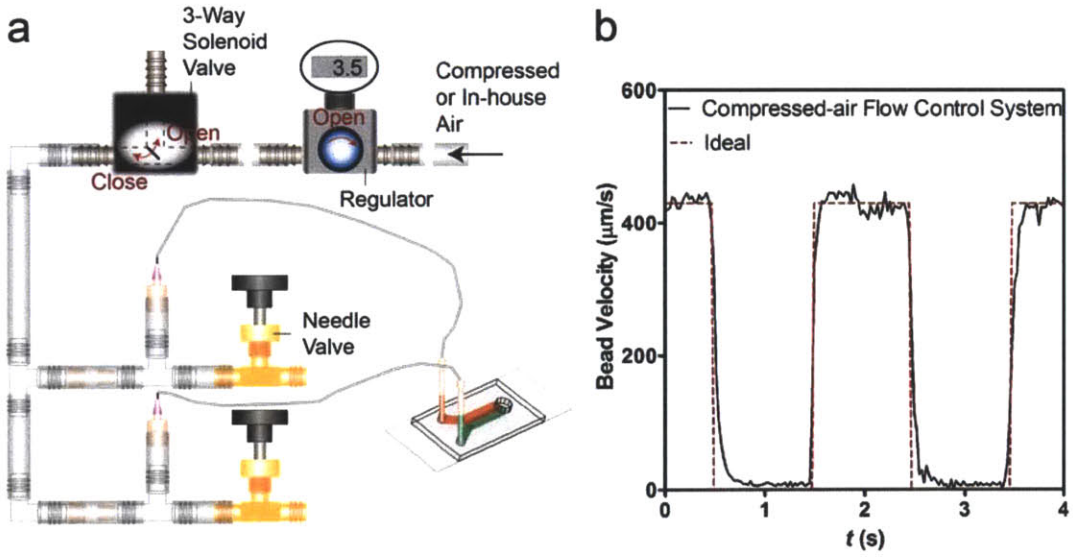

Figure 1.8: *Compressed-air flow control system (a) Schematic of the pressure manifold and its attachment to a two-inlet microfluidic device. Compressed air is down regulated and then passed through a three-way solenoid valve that serves to either pressurize the manifold (open) or vent to the atmosphere (closed). Two control channels, each with its own sample arm and relief needle valve, are pictured branching off the main supply line. (b) Pulsed-flow operation. Pulsing frequency was fixed at 0.5 Hz. The compressed-air system exhibited a rapid reaction to the driving force.*

In CFL, high velocity flows could not be used for particle synthesis because the particle features would be smeared and distorted during the UV polymerization step. To address this, stop flow lithography (SFL), which synthesizes particles while flow has been stopped and then flushes the particles out by high velocity flow pulses, was developed [73]. In this process, the rapid pulsing of microflows was achieved by a compressed-air flow control system (Fig. 1.8a). The simple and inexpensive flow control apparatus was developed by Doyle group, and has provided an economical and scalable solution to generating structured microflows with tunable properties for a range of applications [74]. This pulsed flow control was then synchronized with brief, shutter-mediated UV exposures to complete the SFL process.

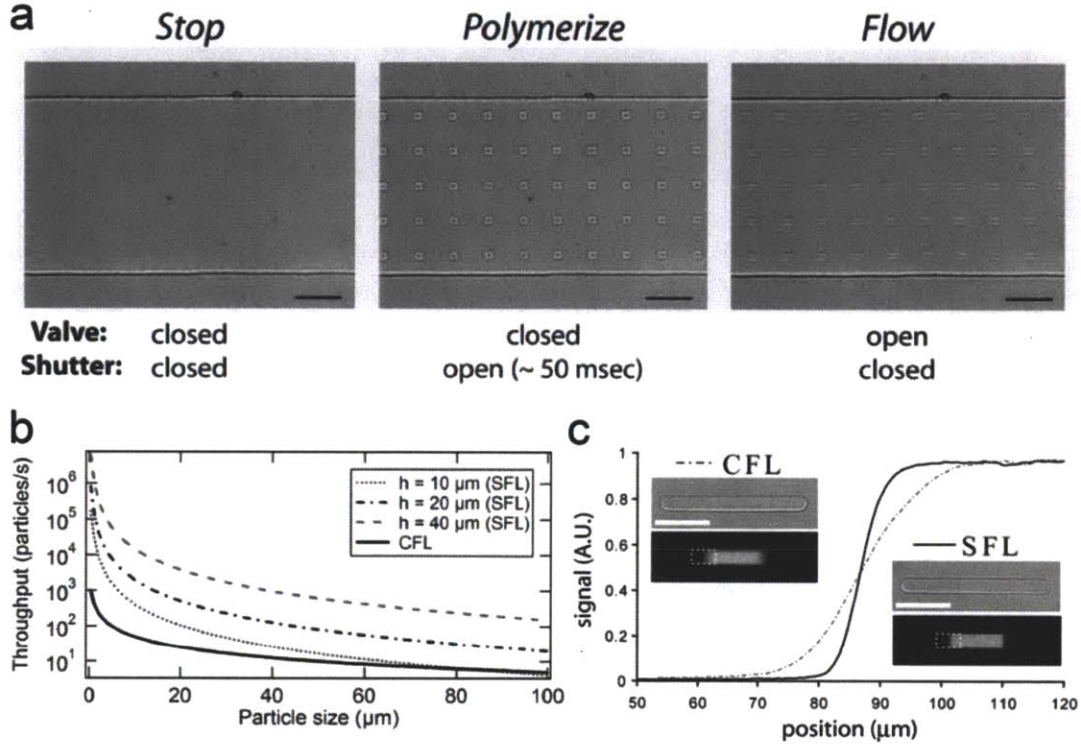

Figure 1.9: *Stop Flow Lithography (SFL) (a) Three steps in the SFL process. The first step is stopping the flow of polymer solution. The second step is photopolymerization via flash of UV light through a mask. The final step is flowing out of microparticles using a pressure pulse. (b) Comparisons for particle throughputs of CFL and SFL. The throughput is a function of particle size. When particle size is getting smaller, the difference of throughputs is getting larger. (c) Comparisons for fluorescent signals of striped particles synthesized from CFL and SFL. Scale bars are 50 μm (a) and 100 μm (c). Figures adapted from ref. 73.*

SFL essentially consists of three states (Fig. 1.9a). First, a flowing stream of oligomer is stopped via pressure release before photo-polymerization. Then, on the stopped flow, an array of particles is formed by UV exposure through a transparency mask using a standard fluorescence microscope. Finally, the formed particles are flushed out at high flow rates

before the cycle of stop-polymerize-flow is repeated. Compared to CFL, SFL has given much improved resolution for particles as the particle synthesis is performed in a stationary fluid. Also, the method can provide a higher throughput up to $10^7 \sim 10^8$ particles per hour using a single microscope. Because SFL does not impose a maximum flow velocity to maintain synthesis fidelity, the technique can offer much faster averaged flow velocity and orders of magnitudes higher throughput than CFL (Fig. 1.9b). Moreover, SFL can improve sharpness of interfaces of striped particles utilizing the high velocity flows (Fig. 1.9c).

1.3.3 Theory

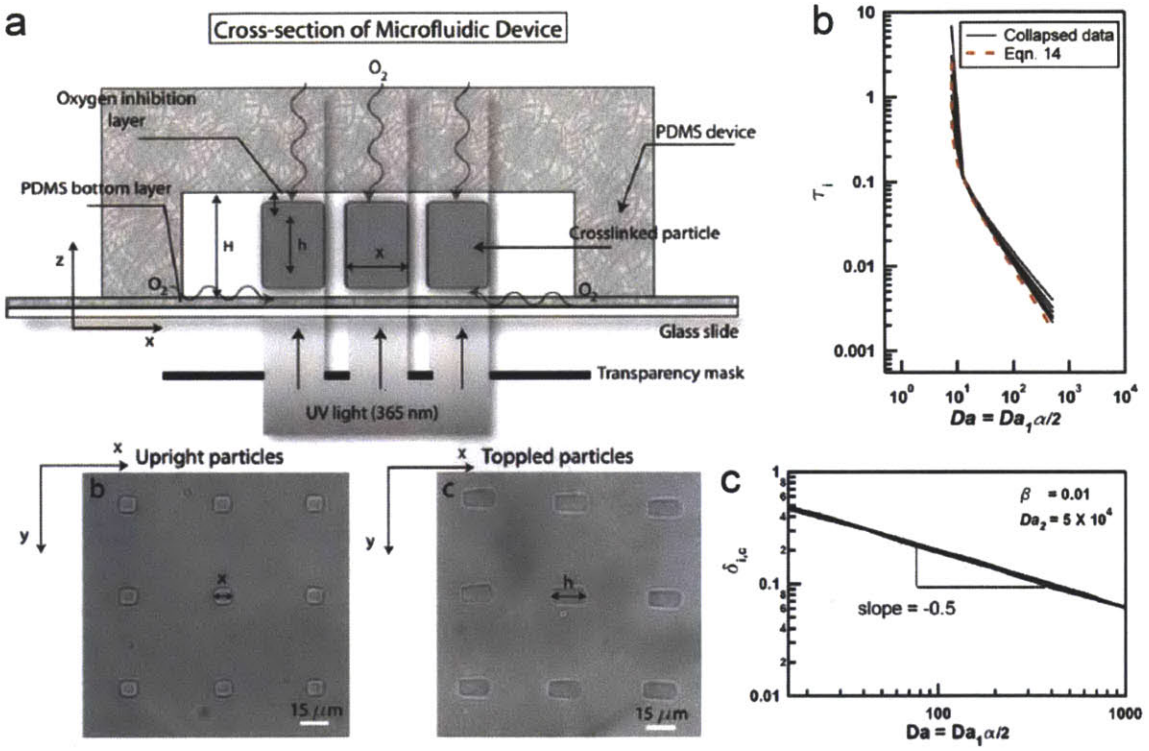

Figure 1.10: *A model for oxygen inhibited photo-polymerization (a) Schematic diagram of the reaction-diffusion model. DIC images show measurements of particle width, x, and height, h. (b) A plot for induction time τ_i as a function of Da. (c) A plot for the critical thickness of the inhibition layer $\delta_{i,c}$ as a function of Da. Figures adapted from ref. 75.*

The theoretical work about the oxygen lubrication layer has been done under 1D (z-direction), unsteady state simplification of the reaction-diffusion model [75] (Fig. 1.10). The oxygen inhibition effect is considered only at the top and bottom walls of the device as particles are usually formed far away from the side walls. The work reveals that 'induction time τ_i (the time when a gel structure is first seen)' and '$\delta_{i,c}$ (the critical thickness of the inhibition layer)' are just related with a dimensionless number, Da which contains key FL

process variables such as light intensity, photoinitiator concentration, and channel height (Fig. 1.10b and c). The lumped parameter Da is given by the following equation.

$$Da = \frac{\varphi \varepsilon [PI] I_0 H^2}{D_0 [O_{2,eqb}]}$$

where φ is the quantum yield of formation of initial radicals, ε is the molar extinction coefficient of the photoinitiator at 365nm, [PI] is the concentration of the photoinitiator species, I_0 is the light intensity, H is the height of the channel, D_0 is the diffusivity of oxygen in the oligomer, and $[O_{2,eqb}]$ is the equilibrium concentration of oxygen in the oligomer, which in turn is always in contact with air-saturated PDMS.

1.3.4 Applications of Flow Lithography

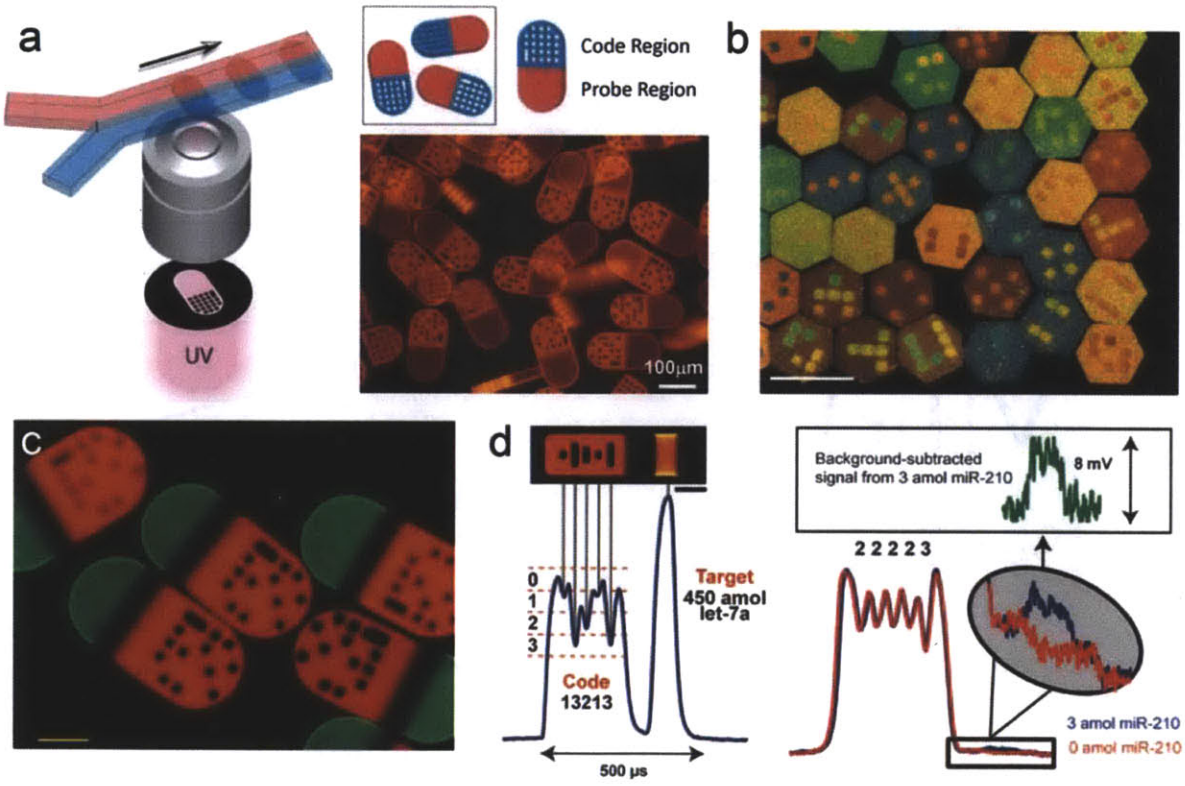

Figure 1.11: *Barcoded hydrogel particles (a) A schematic depicting the synthesis process of barcoded particles. The inserted fluorescent image show barcoded particles produced from the process. Figures adapted from ref. 7. (b) The fluorescent image of color-coded particles. The colors were generated from 1D photonic crystal structures of magnetic nanoparticles. Image adapted from ref. 76. (c) A fluorescent image of barcoded particles conjugated with fluorescently labeled viruses. Image adapted from ref. 83. (d) High sensitivity of barcoded particles. The particles detected micro-RNAs at atomolar concentrations. Figures adapted from ref. 78. Scale bars are 500 μm (b) and 50 μm (c).*

FL typically use monomers based off of poly(ethylene glycol) that is bio-friendly, highly tunable, and can be functionalized with a variety of biomolecules. As a result, numerous bio-related applications have been generated. One of the important applications is the synthesis of barcoded particles that have code regions and one or more probe regions [7]. The particles have been used for the high-throughput screening of biomolecules in multiplexed fashion. In this application, FL has allowed for easy modification of code shapes and probe-sets. When structured colors are utilized by modulating 1D chain structures of magnetic nanoparticles, the number of available codes can even reach to 8^{10} [76]. Also, the barcoded particles have loaded various probe sets to detect wide ranges of biomolecules including DNAs [7, 77], RNAs [78, 79], proteins [80-82], and even viruses [83]. The powerful advantages of the barcoded particles are high sensitivity and specificity for target molecules. Recently, micro-RNAs, which are one of the important cancer signatures and low abundance biomolecules, were detected in extremely low concentrations using the barcoded particles [78, 79].

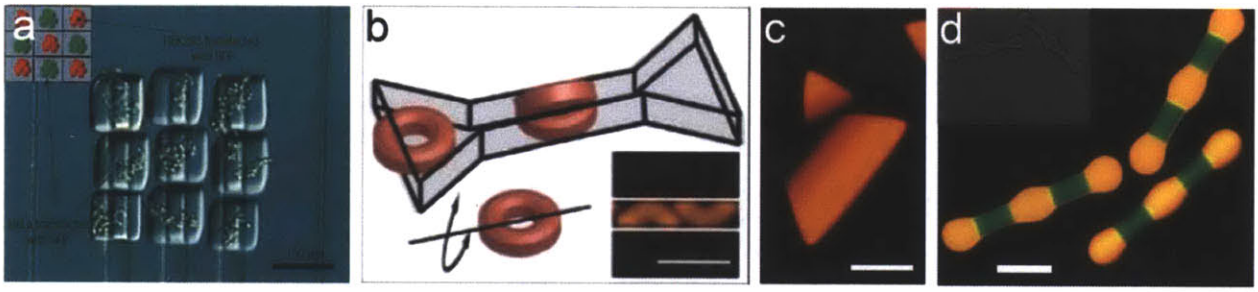

Figure 1.12: *Bio-related applications of FL (a) Assembly of cell-laden hydrogel particles using a railed microfluidic device. Image adapted from ref. 84. (b) Biomimetic hydrogel particles. The particles were enough squishy to penetrate into a channel that had smaller dimensions than their sizes. Figures adapted from ref. 86. (c) A fluorescent image of biodegradable particles. A triangle particle was divided into two parts as the middle biodegradable part disappeared by erosion. Image adapted from ref. 85. (d) Nanoemulsion composite microgels. The nanoemulsions allow for the release of drugs encapsulated in the gel particles, and reloading of drugs. Image adapted from ref. 88. Scale bars are 10 μm (b) and 50 μm (c and d).*

Another application is the preparation of building blocks for tissue engineering. Anisotropic cell-laden hydrogel particles were synthesized from FL [40], and assembled to target constructs in a railed micro-fluidic device [84]. Other applications are biodegradable particles to evolve shapes [85], squishy particles to exhibit similar behaviors to red blood cells [86], and nanoemulsion composite microgels to release and reload drugs [87, 88]. However, applications of FL have not been limited in bio-areas. For MEMs applications, FL was used to produce polymeric gear-shaped particles from monomer solutions containing 500 nm colloidal silica particles [89]. To convert the particles to hard micro-gears, they were further sintered at 850 °C. Also, micro-actuators that could provide complex motion for MEMs were achieved by patterning of magnetic anisotropy [90]. Moreover, the synthesis of

amphiphilic particles have been interesting in assembly areas [91]. The particles had a similar motif with block copolymers, and were assembled to multi-component constructs by the hydrophobic and hydrophilic interactions. Lastly, for photonic applications, FL was used for structural color printing [92].

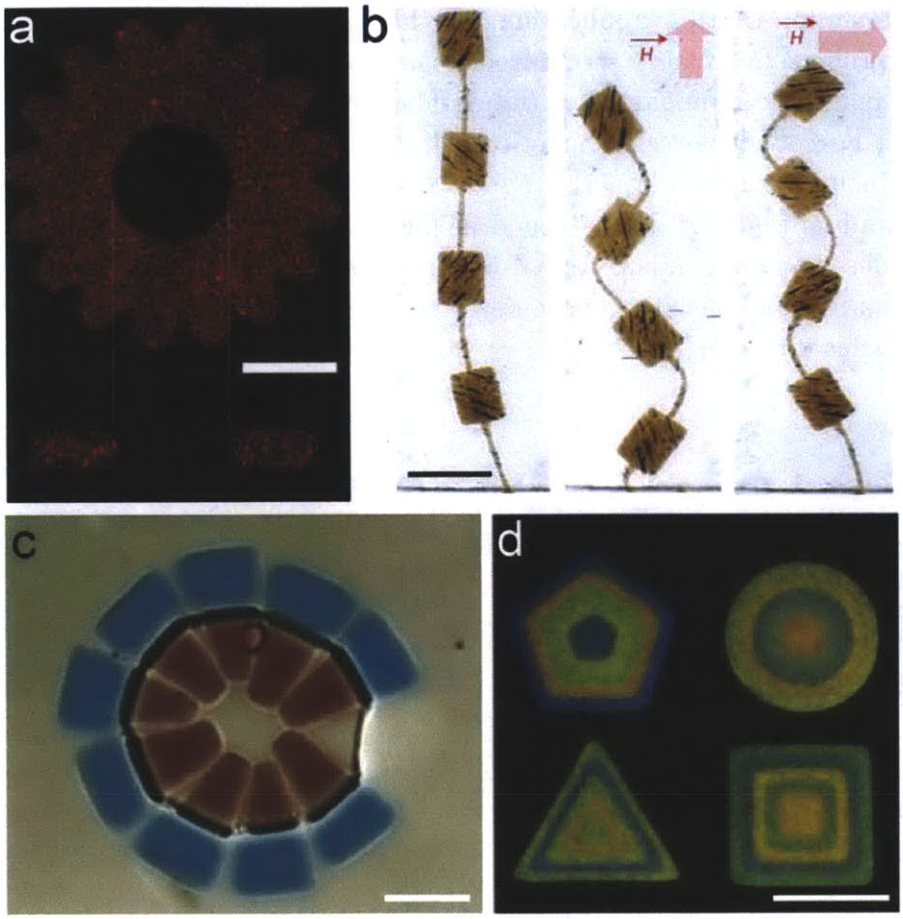

Figure 1.13: *Other applications of FL (a) A confocal image of a micro-gear for MEMs applications. The gear was fully compacted with glassy silica colloidal particles. Image adapted from ref. 89. (b) Micro-actuators for MEMs applications. In the presence of external magnetic field, the actuator exhibited anisotropic motions because the structure had programmed magnetic anisotropy. Image adapted from ref. 90. (c) Anisotropic amphiphilic particles. Particles with a large hydrophilic head (blue) and a small hydrophobic tail (red) were assembled at the interface of oil-in-water. Image adapted from ref. 91. (d) Structural color printing. Magnetic nanoparticles were used to generate different structural colors by modulation of external magnetic fields. Image adapted from ref. 92. Scale bars are 100 μm (a, b, and d), and 50 μm (c).*

1.3.5 Limitations

Although FL has been a versatile method for wide ranges of applications, the primitive versions of flow lithography and barcoded particles have shown following limitations.

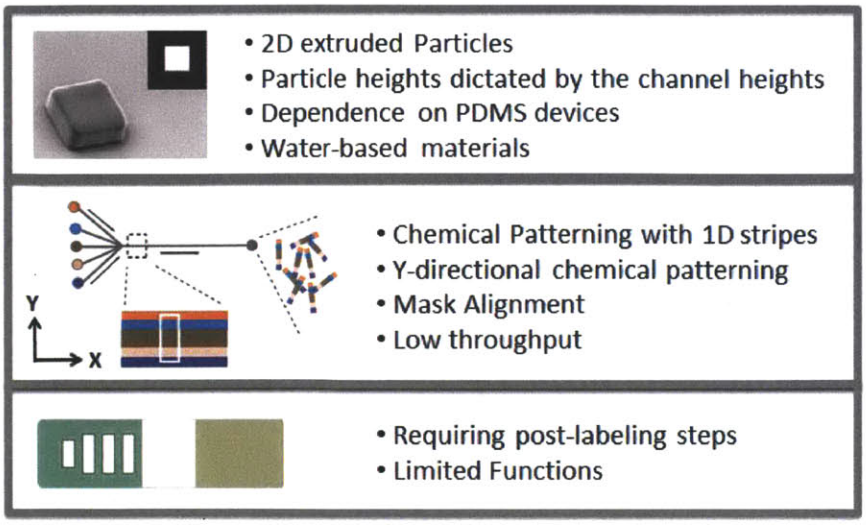

Figure 1.14: *Limitations in the primitive versions of flow lithography and barcoded particles.*

First of all, flow lithography has only produced quasi-2D extruded particles. Also, the need of oxygen inhibition layers has made the requirement of PDMS channels and fixed particle heights to the channel heights. The PDMS dependence even prevents the use of solvents and monomers that can swell PDMS. Furthermore, the chemical patterning of particles has been limited to y-directional 1D stripe motifs. During such striped particle synthesis, the method requires a precise mask alignment across the interface and each synthesis step polymerizes only 1-D rows giving a low throughput. Finally, for the barcoded particles, the particles have required complex post labeling steps and exhibited limited functions.

1.4 Outline of Thesis

The purpose of this work is to develop advanced flow lithography and barcoded particles to address the above limitations. The organization of this work is as follows:

Chapter 2 describes a new technique called lock release lithography that moves FL from 2D to 3D, and provides complex chemical patterns in x-y dimensions of particles.

Chapter 3 describes a new technique called hydrodynamic focusing lithography that can be used to provide chemical patterns in z-dimension or y-z dimensions of particles.

Chapter 4 describes a new technique called oxygen-free flow lithography that greatly expands the synthesis capabilities of FL in the following three categories: (1) device construction, (2) process control, and (3) operable material.

Chapter 5 describes advanced hydrogel barcoded particles that have magnetic functionality, tri-layered structures, and near-infrared sensing abilities.

Chapter 6 suggests future directions for works presented in this thesis.

Chapter 2

Lock Release Lithography for 3D and Composite Microparticles

In this section, we present a new method called "Lock Release Lithography (LRL)" that provides a means for the high-throughput production of particles with complex 3D morphologies and composite particles with configurable chemistries. We demonstrate a diverse set of functional particles that can be formed using this method. Particles made using LRL can originate from a broad range of precursor materials and may contain variety of functional entities including nucleic acids, proteins, quantum dots, beads, and living cells. This technology may provide a powerful means to mass-produce functional units for microfluidic operations, filtration systems, and tissue engineering constructs.

2.1 Introduction

Particles with three-dimensional (3D) morphologies and configurable chemistries hold great potential for a host of applications in drug delivery [1, 2], tissue engineering [4-6], optics [16] and electro mechanics [17]. In addition, they promise distinct advantages as sorting media [7] and stimuli-responsive materials [2, 93, 94]. Of particular interest, patterned particles with precisely positioned chemistries could provide the building blocks for self-assembled, dynamic structures with complex functionality [21, 22]. Despite their enormous potential, 3D and composite particles cannot be efficiently synthesized on a large scale using current methodologies [45-48, 95-98]. Multiphoton fabrication [46] is a well-known method for synthesizing micro/nano 3D structures as it

provides unparalleled control of morphology in all dimensions. In spite of the advantage, this direct drawing technique is prohibitively time-consuming. For higher throughput, 3D particles can be generated using a layer-by-layer process with photo resists [47, 48]. Unfortunately, these materials are not ideal for many applications, the chemistries are extremely restricted, and the chemical patterning is limited to layered motifs. Three-dimensional particles can alternatively be generated using the PRINT method [95], where particles are shaped using a 3D mold. However, the shapes of such molds are limited, and the process is not suitable for the synthesis of particles with multiple patterned chemistries. There exist several other synthesis techniques [96-98] that suffer from similar constraints of morphology and functionality. Here, we present a method called "Lock Release Lithography (LRL)" that utilizes a combination of channel topography, mask design, and pressure-induced channel deformation to form and release particles in a cycled fashion. This technique provides a means for the high-throughput production of particles with complex 3D morphologies and composite particles with configurable chemistries.

2.2 Experimental Methods

Materials

All of the particles shown in Figure 2.1 ~ 2.9 were made using solutions of 5% (v/v) Darocur 1173 (Sigma Aldrich) initiator, 35% (v/v) 1X TE buffer and 60% (v/v) poly(ethylene glycol)(700) diacrylate (PEG-DA, Polysciences). Twenty base pair oligonucleotide probes, #1 (5′-ATA GCA GAT CAG CAG CCA GA-3′) and #2 (5′-CAC TAT GCG CAG GTT CTC AT-3′) were purchased from IDT with Acrydite modifications and mixed into the monomers for a final concentration of 50 μM. To distinguish between chemistries for multifunctional particles, we added 5% (v/v) food color into desired chemistries. For swelling particle regions, we used solutions of 15% (v/v) acrylic acid (Polysciences), 15% (v/v) PEG-DA (700), 30% (v/v) poly(ethylene glycol)(200) (PEG, Sigma Aldrich), 5%(v/v) Darocur 1173 and 35% (v/v) 1X TE. Finally, particle regions with encapsulated entities were made from solutions comprised of 30% (v/v) PEG-DA (700), 3.5% (v/v) Darocur 1173, 59.5% (v/v) 1X TE buffer, 5% (v/v) Tween 20 (Sigma Aldrich) with 2% (v/v) fluorescent protein (streptavidin-phycorytherin, Invitrogen) or 5% (v/v) 2 μm fluorescent beads (FITC, Polysciences) in 5% (v/v) Darocur 1173, 30% (v/v) 1X TE buffer and 60% (v/v) PEG-DA. Solutions, 0.01% wt, of the fluorescent methacryloxyethyl thiocarbamoyl rhodamine B (Polysciences) in PEG-DA were used to fluorescently label the hydrogel.

Microfluidic Device

Devices were fabricated by pouring polydimethylsiloxane (PDMS, Sylgard 184,Dow Corning) on a silicon wafer containing positive-relief channels patterned in SU-8 photoresist (Stanford Foundary). The devices were 1,000 μm wide channels with varying

heights (20, 30 or 60 μm) and various negative or positive topograhies (10 or 30 μm tall) on their ceiling. These devices were placed on PDMS-coated glass slides or plasma sealed to patterned PDMS surfaces after placing thin sacrificial layers of PDMS on the channel alone and on the region of the PDMS surfaces which sits right under the channel. This is to ensure that the oligomer was only exposed to the PDMS surfaces. The devices were mounted on an inverted microscope (Axiovert 200, Zeiss), and the formation of the microparticles was visualized using a charge-coupled-device camera (KPM1A, Hitachi). Images were captured and processed using NIH Image software or a digital camera (D200, Nikon) and Nikon Capture software.

SFL Setup

The setup for SFL requires the use of pressure provided by a compressed-air source to drive flow inside the microfluidic channels. To generate controlled pressure in the range of 0–15 psi, a compressed air source (~ 40 psi) in the laboratory was first connected to either a T3510 I/P transducer (Marshbellofram) or a Type 100 LR manual pressure regulator (Control Air). Downstream of the transducer/regulator, a 3-way solenoid valve (Burkert) was used to switch rapidly between atmospheric pressure (stop) and the input pressure (flow). The output from the 3-way valve was connected to the microfluidic device using Tygon tubing connected to a 10 ml pipette tip (Biosciences). The pipette tip was filled with the desired fluid and inserted into the inlet hole punched in the microfluidic device. The transducer, 3-way valve and shutter were all controlled using VIs written in Labview 8.1 (National Instruments). The 3-way valve was controlled using a 1024-HLS digital I/O board (Measurement Computing) and a relay. The transducer and the shutter were controlled using serial connections.

Photopolymerization Setup

Photomasks were designed in AUTOCAD 2005 and printed using a high-resolution printer at CAD Art Services (Bandon, OR). The mask was then inserted into the field-stop of the microscope. A 100W HBO mercury lamp served as the source of UV light. A filter set that allowed wide UV excitation (11000v2: UV, Chroma) was used to select light of the desired wavelength and a VS25 shutter system (Uniblitz) driven by a computer-controlled VMM-D1 shutter driver provided specified pulses of UV light. Typical exposure times used were 30–100 ms and pressures ranged from 0.05 to 15 psi. A reservoir was cut in the PDMS to collect the particles.

2.3 LRL for 3D Particle Synthesis

We introduce lock release lithography, built off of continuous-flow [72] and stop-flow lithography [73], which can overcome the above limitations on throughput, 3D morphology, and composite chemistries using the combination of channel topography, mask features, and pressure-induced channel deformation. The process consists of (1)

stopping the flow of a UV-sensitive monomer stream through a microfliudic channel, (2) lithographically printing structures that are "locked" into regions with multi-level channel topography, and (3) inducing channel deformation via high pressure to release structures for harvesting. In the example shown in Figure 2.1, we formed particles by 75ms of UV exposure through a transparency mask using a standard fluorescence microscope. Particle morphology is defined by a combination mask feature shape and channel topography. Locked into the three-dimensional relief, particles remain immobilized until a relatively high pressure (~ 5 psi) is applied to the poly(dimethylsiloxane) (PDMS) channel to initiate flow and deflect the channel beyond the point of particle release. Using an automated valving system, the flow is then stopped via pressure release, and the process is repeated, thus allowing the formation of 3D particles in an automated, semi-continuous manner.

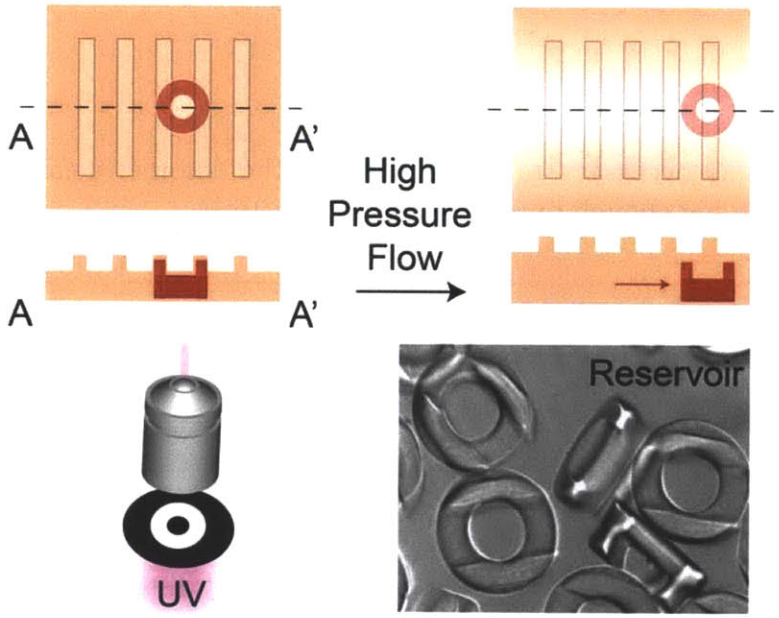

Figure 2.1: *Process of lock release lithography. First, structures are polymerized by shining bursts of UV light through a transparency mask and a microscope objective. The structures, having a shape determined by the mask and channel topography, are "locked" by relief structures in the channel topographies. Particles are "released" with channel deflection after a relatively high pressure (~ 5psi) is applied to initiate flow. Differential interference contrast (DIC) image of collection of 3D particles in the channel reservoir.*

With the need for periodic channel deformation, this process is well-suited by stop-flow lithography, but incompatible with continuous-flow techniques [72, 84]. Recently, continuous-flow lithography was used to fabricate finned structures in "railed" channels for guided self-assembly [84]. However, without release, this process cannot be used to

generate diverse topographies. Several other advantages are afforded by stop-flow, including improved resolution and a higher throughput up to 10^6 ~ 10^7 particles per hour using a single microscope [73]. Like the other flow lithography techniques [72, 73, 84], LRL utilizes simple microfluidic control and can be applied to a broad range of precursor materials. Functional particles generated with flow lithography have contained nucleic acids for bioassays [7], whole cells for tissue engineering [40], hydrophilic and hydrophobic materials for self-assembly [55], and even glassy materials [56]. Because LRL is a variant of flow lithography [72, 73, 84], the oxygen lubrication layer near channel surfaces is expected to be a ~ 1 μm thick [72]. Thus, the achieved particle size in LRL is limited to micrometer ranges. Due to the size limitation, the particles produced by LRL could not be suitable for sub-micormeter applications such as cell uptake. Topographical channel features used in LRL are at least a few microns in size, larger than the UV wavelength (~360 nm), such that optical interference can be disregarded.

2.3.1 Theory

To develop LRL, it is necessary to check whether the channel deformation in a PDMS microfluidic device is big enough to release locked structures.

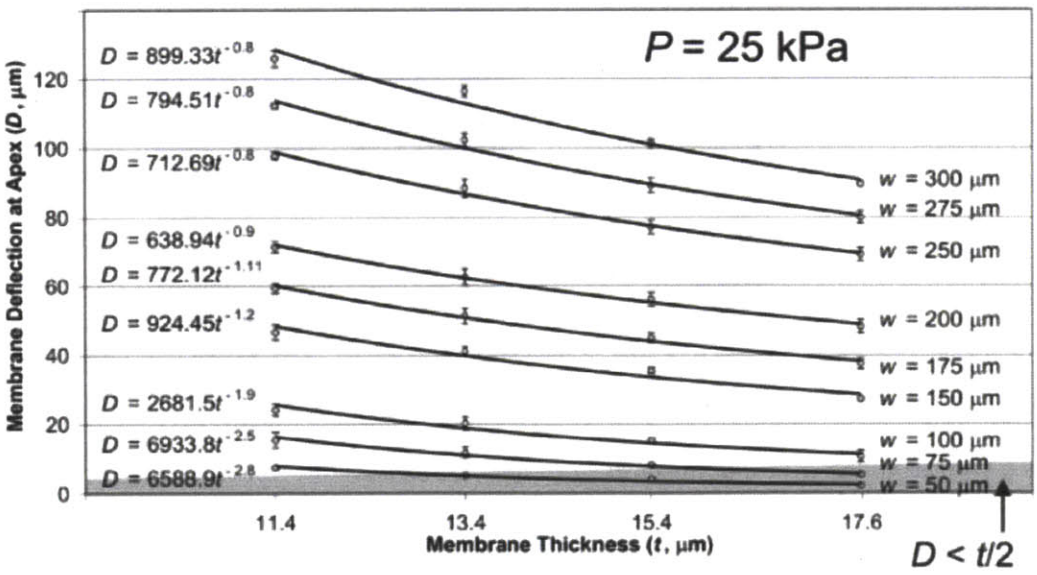

Figure 2.2: *Measurements of membrane deflection at apex for membrane thickness [Ref. 100]*

Fortunately, there are previous researches about the elastic deformation. Jensen and coworkers have demonstrated that scaling analysis for a thick, "semi-infinite" PDMS channel gives the flow-induced maximum deformation of

$$\Delta h_{\max} = C_1 \frac{P(z)W}{E} \tag{2.1}$$

Where C_1 is a proportionality constant of magnitude order one, W is the width of the channel, E is the young's modulus of PDMS, and P(z) is the pressure at any position z along the direction of flow [99]. Using a typical operating pressure of 5 psi with a channel 1,000 μm wide, the maximum deformation is expected to be ~ 100 μm [99]. From their results, the following considerations should be taken for the development of LRL. To exploit maximum channel deformation and ensure safe particle release, particles will be polymerized near the channel inlet, channels will be kept fairly wide, and the channel region near the outlet designed to be taller than the particles. When much larger relief features are desired, it is possible to use a thin PDMS channel, which allows for significantly more deflection. In this case, the deformation is determined by classical elasticity theory as

$$\Delta h_{\max} \approx 0.142 \frac{PW^4}{Et^3} \tag{2.2}$$

Where t is channel thickness [100]. For thin channels, which have a ceiling PDMS thickness around 200 μm, 5 psi pressure will provide enough deflection to release 3D particles with relief features of ~ 250 μm. For extremely thin channels (~ a few microns thickness), Folch and coworkers found that the channel deformation largely surpassed the value predicted by the classical elasticity theory. They proposed that the theory would be broken on the condition ($t < d/2$ where d is the maximum deformation) [100]. In this case, the deflection must be determined empirically as shown in Figure 2.2. If LRL use these thin channels, there will be requirements of PDMS adapters at the inlet and outlet to provide robust connections for sample introduction and particle collection. Based on these researches, LRL is feasible enough to produce 3D and composite particles via control of pressure.

2.3.2 Various 3D Particles

In lock release lithography, particle morphology is defined by a combination of channel topographies and mask feature shape. Numerous combinations can be used to produce diverse 3D morphologies in particles. Using the first combination in Figure 2.3, we generated squares with 1 micrometer line patterns. This validated that fine features of only a few microns could be patterned although the oxygen lubrication layer near channel surfaces is expected to be a ~ 1 μm thick [72]. As channel topographies, we used very fine negative 3.5 μm line-space patterns (with 7 μm pitch). These troughs could be oriented with the particle edges (Fig. 2.3c and d) or made to be oblique by simply rotating the mask with respect to the channel. The particles might exhibit interesting optical properties via interference with visible rays. The second combination in Figure 2.3 was used to generate squares with 10 micrometer high pillars that mimic gecko

adhesive patterns. Adding bottom channel topographies can lead to more complex 3D morphologies in particles. To demonstrate that both channel floor and ceiling topographies could be used to dictate morphology, we synthesized table-like structures with large relief features on one side and a highly resolved 5 μm line-space pattern on the other (Fig. 2.3i). These particles demonstrate the ability to combine coarse and fine features into particle topology.

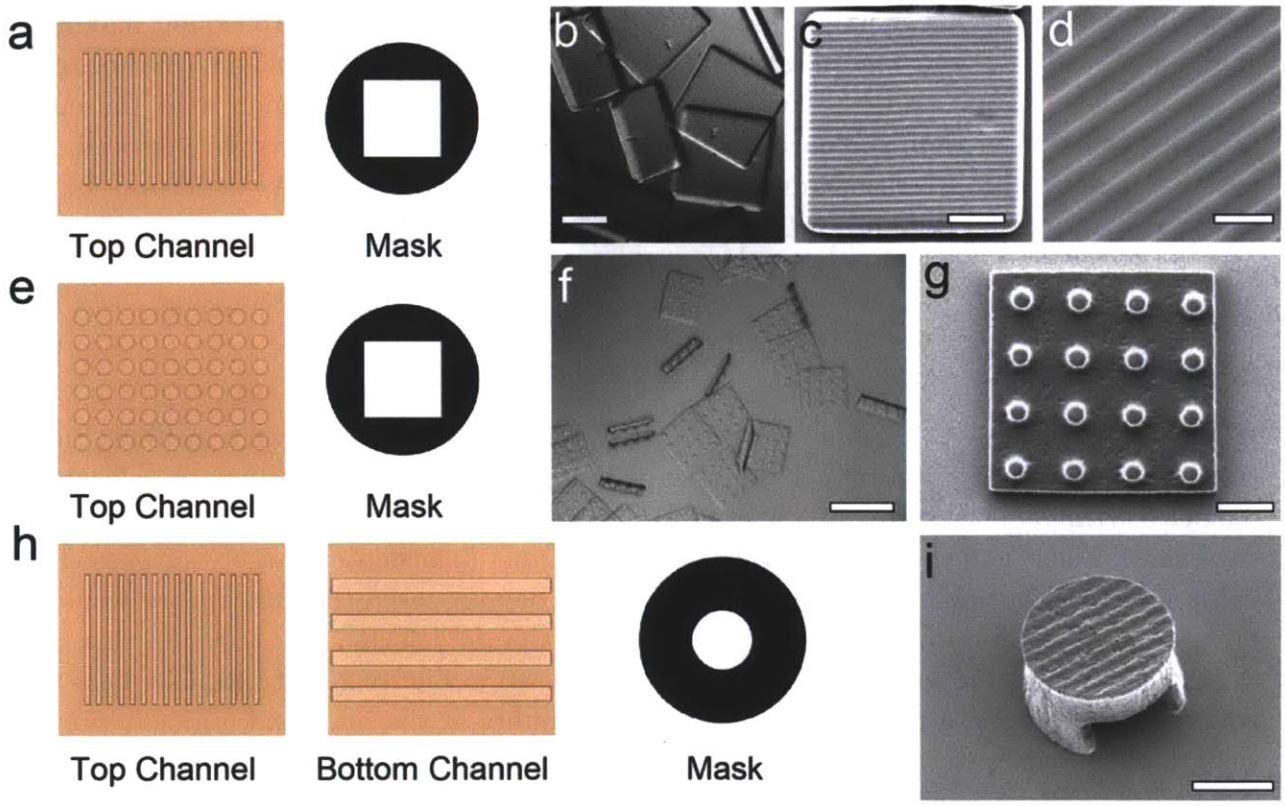

Figure 2.3: *3D particle synthesis from channels with negative topographies (a)-(d) Squares with 1-μm-high line-space patterns using 30-μm-high channel with negative line-space patterns on its floor and a square mask. (e)-(g) Squares with 10-μm-high gecko-type patterns using 20-μm-high channel with negative dot patterns on its ceiling and a square mask. (h)-(i) Table-like 3D particles with 1-μm-high line space patterns on the top and 30-μm-high supports on the bottom using 30-μm-high channel with negative line-space patterns on both sides and a circle mask. Scale bars are (b) 100 μm (c, g, i) 50 μm, (d) 10 μm, and (f) 200 μm.*

Importantly, LRL can be performed with the same channel and varying masks to give a variety of particle morphologies. To demonstrate this, we altered the square mask to a cross-shaped mask in the 30 μm channels with negative dot patterns, and produced the particles shown in Figure 2.4a. We also showed that the channel topographies could be beyond dot and line patterns. Using a channel with negative MIT patterns, we generated T-shirts particles with three dimensional MIT logo.

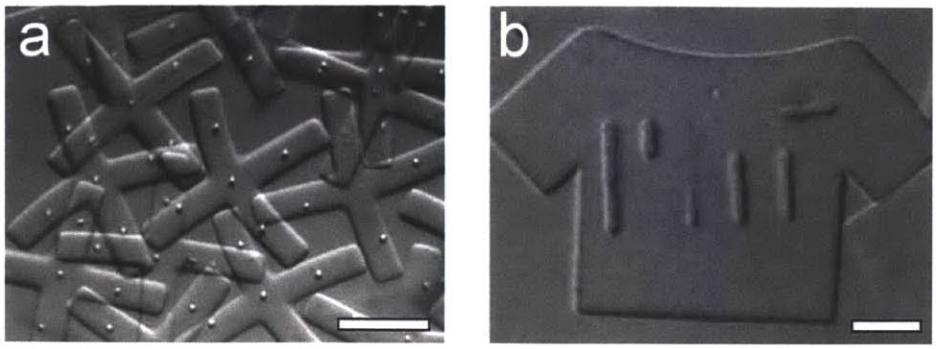

Figure 2.4: *Synthesis of variants by changing masks and/or channel topographies (a) Variants using 30-μm-high channels with same kinds of topographies of negative dots on their ceiling, but different cross mask. (b) Micro T-shirt with 3D MIT logo. Scale bars are (a) 200 μm and (b) 50 μm.*

Furthermore, positive channel topographies can be used to generate dishes and cups. These particles have voids that could potentially be filled with active components or cells. Morphologies generated with LRL can be more complicated depending on the mold used to generate the channel topographies, and the mask used to polymerize the particles. Molds generated using standard lithography can be multi-tiered, rounded, or slanted [101], while virtually any topography can be achieved using multiphoton fabrication [45, 46]. The transparency masks used to generate particles can have virtually any two-dimensional shape, can be greyscale [17] to provide variability in height along particles, and can be used in conjugation with interference masks to give finely tuned microporous structures [102]. Combinations of channel topography and mask shape can provide intricate structures such as coils, but in its current inception, LRL is not suitable for the preparation of interlocking (like chain links) features or particles with internal hollow structures.

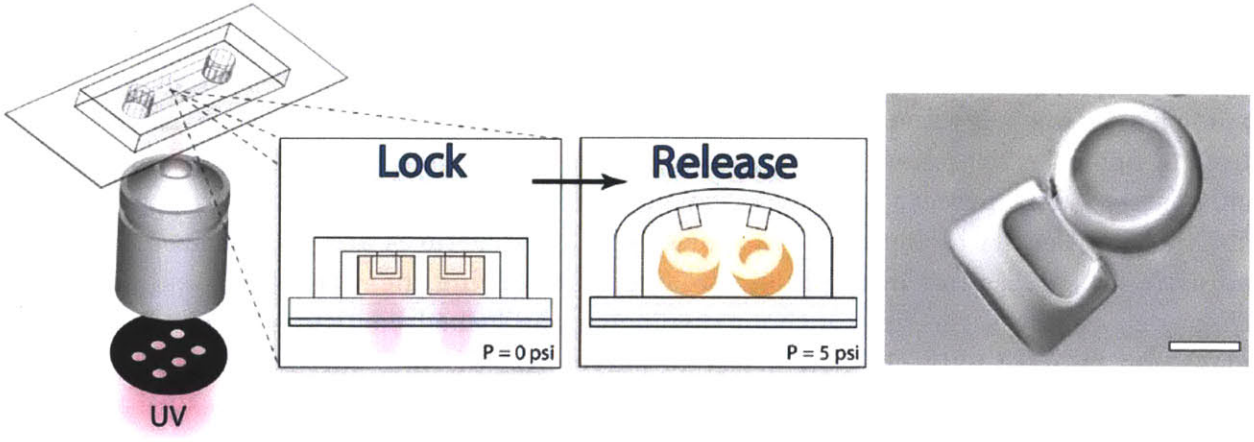

Figure 2.5: *3D particle synthesis from channels with positive topographies. Microcups with 30-μm-deep voids were generated using 60-μm-high channel with positive dot patterns on its ceiling and a circle mask. Scale bar is 50 μm.*

2.4 LRL for Composite Particle Synthesis

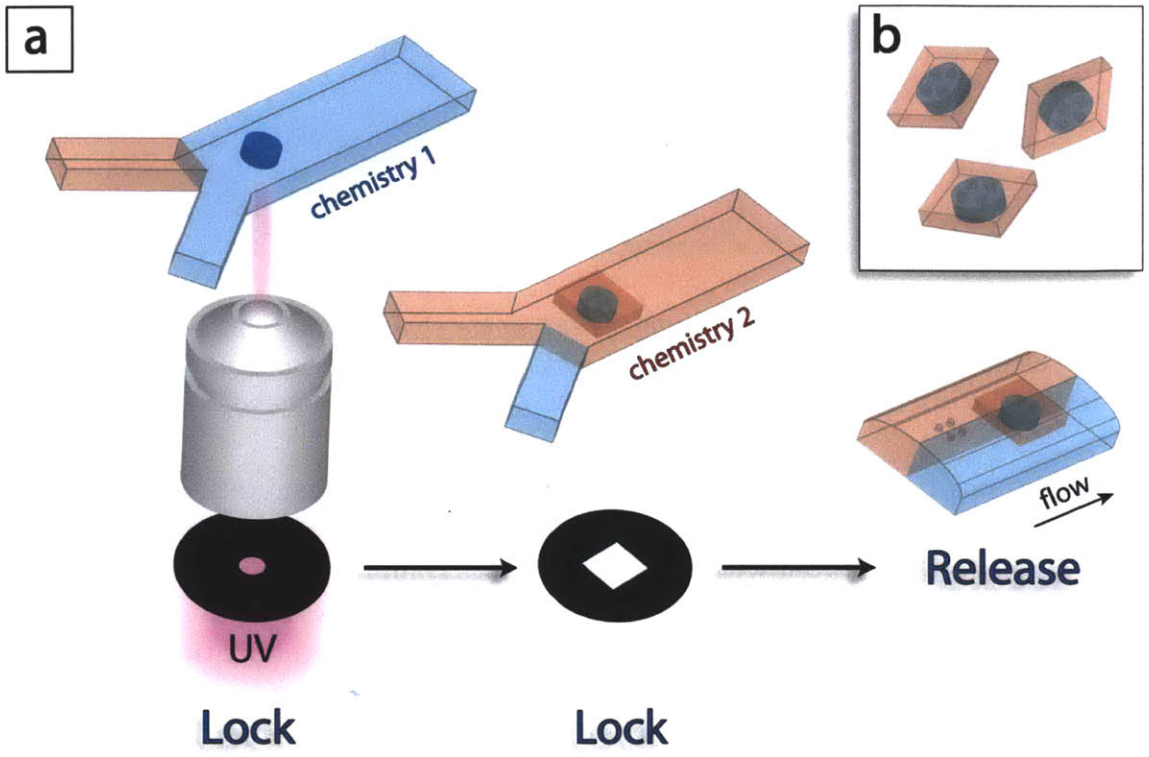

Figure 2.6: *Synthesis of composite particles. (a) A schematic diagram showing the synthesis of composite particles. Locking structures with chemistry 1 are covalently linked to chemistry 2 through mask overlap and UV exposure after fluidic exchange with low pressure. Then, the composite structures are released by high pressure in both flows. (b) A schematic description of particles produced by the process (a).*

Perhaps the most attractive feature of lock release lithography is that the release time is controllable. Because particle release occurs at a critical pressure (related to deformation), lower pressures can be used to exchange monomer without unlocking particles – this allows subsequent addition of new chemistries. As such, LRL can be used efficiently to generate composite particles with multiple precisely engineered chemistries. The process is shown schematically in Figure 2.6. First, the multi-inlet channel is filled with chemistry #1 and locked 3D structures are polymerized. Then, by adjusting the pressures of the inlet streams (but keeping them below ~ 1 psi), a second chemistry replaces the first without displacing the locked particle structure. A unique mask can be used with this chemistry to polymerize distinct particle features that are covalently linked to the locked particles via overlap. Finally, a high pressure flow (~ 5 psi) is used to release the composite particles (Fig. 2.6b).

2.4.1 Composite Particles with Two Chemistries

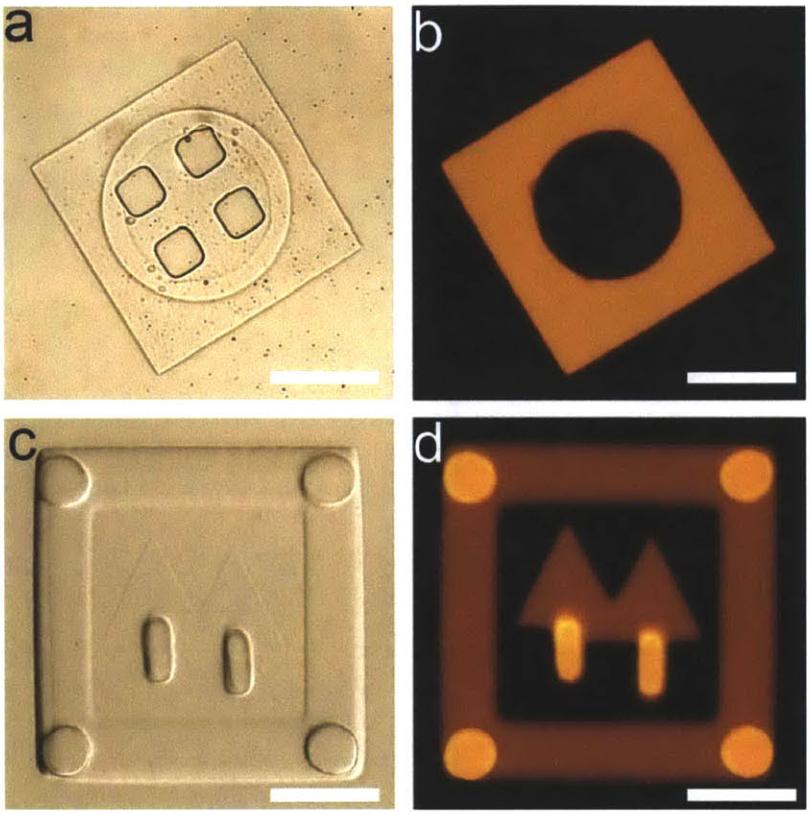

Figure 2.7: *Composite particles with two distinct chemistries. (a) DIC image of a composite particle with a circular center and square exterior. (b) Fluorescence microscopy image of the particle shown in (a). (c) DIC image of a composite particle with interior features and border. (d) Fluorescence microscopy image of the particle shown in (d). Two streams containing PEG-DA and PEG-DA with rhodamine-labeled monomer were used to respectively present chemistry 1 and chemistry 2. Scale bars are 100 μm (a and b) and 50 μm (c and d).*

To demonstrate the synthesis of composite particles, we used two chemistries, both with PEG-DA monomer and one with a fluorescent monomer (rhodamine-acrylate, orange) to easily distinguish the chemistries via fluorescence after polymerization. We used positive-relief locks to synthesize patterned particles with a circular center and square exterior (Fig. 2.7a and b), and negative-relief locks to make more intricate particles with interior features and border (Fig. 2.7c and d). Both particle types were generated using two polymerization steps, and in the second case, it was important to lock in each fluorescent region separately to maintain proper orientation before the filler chemistry was added. The locks correspond to the brighter regions of fluorescence in the particle corners and interior (Fig. 2.7c and d). In both cases, the channel topography locks were only 10 μm tall, and thus we were able to use standard "thick" PDMS devices without need for thin membrane-like deflection.

2.4.2 *Scalability*

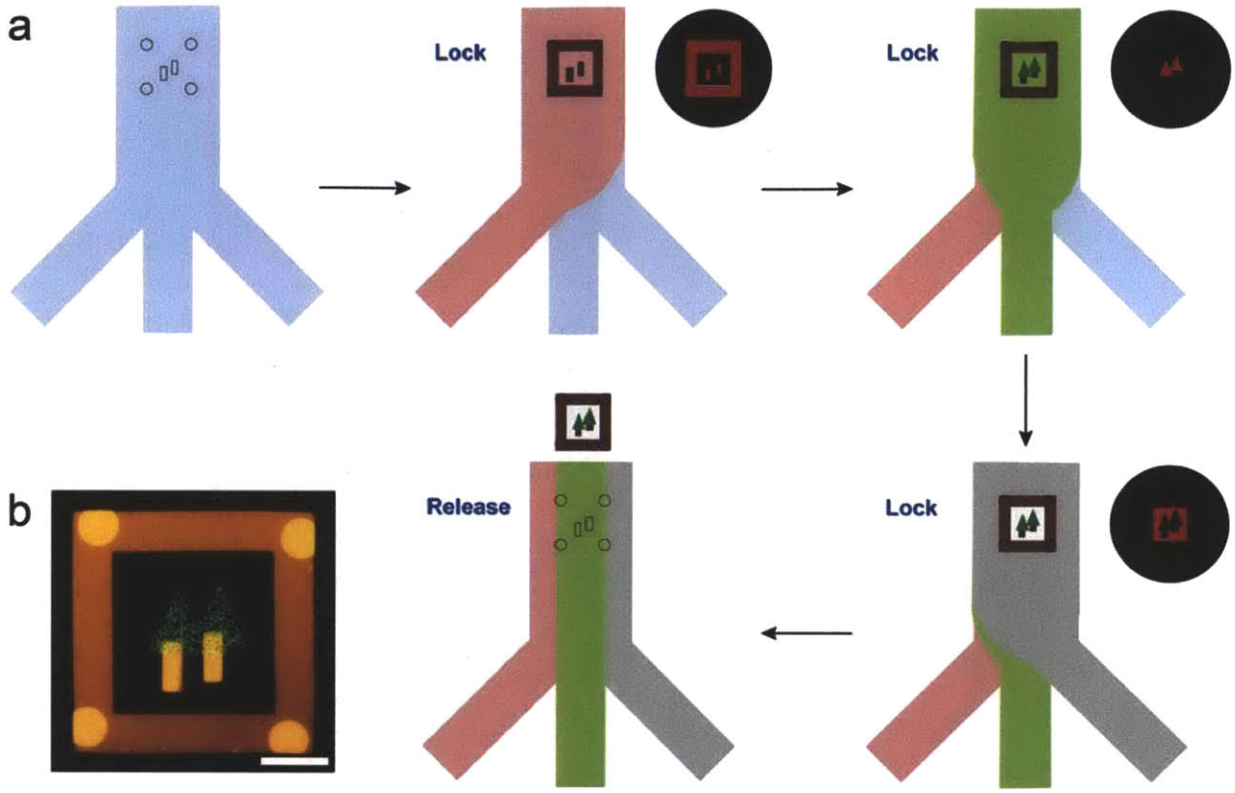

Figure 2.8: *Composite particles with three distinct chemistries. (a) A schematic diagram showing the synthesis of composite particles with three chemistries. First, we flow a prepolymer solution with red fluorophores, rhodamine-acrylate. Using a first mask, we generated a frame and two trunks of trees locked in the channel topographies. Then, in a low pressure, we replace the first prepolymer solution as a second one with 200 nanometer green fluorescent beads. Using a second mask, we created leaves of trees. After that, we flow third prepolymer solution with no fluorophores in a low pressure. With a final mask, we connect trees with the frame. Finally, a high pressure flow is used to release the composite particle. (b) Fluorescence microscopy image of a composite particle synthesized in the process (a). Scale bar is 50 μm.*

The LRL process for the synthesis of composite particles can be applied to any number of unique chemistries. Shown in Figure 2.8 is one example that applies three chemistries. The particles were synthesized by the same process using one more PEG-DA monomer stream with 500 nm fluorescent beads (chemistry 3). In this case, the sequence of polymerization is chemistry 2 (PEG-DA with rhodamin-acrylate), chemistry 3, and then chemistry 1 (PEG-DA). However, due to lag times associated with fluidic exchange and mask alignment, the throughput for composite particles depends on how many chemistries are applied. When two chemistries are used, we can generate ~ 10^3 particles per hour on our current system. When the number of chemistries increases, the throughput decreases. This can be expedited in the future using dynamic mask systems [103].

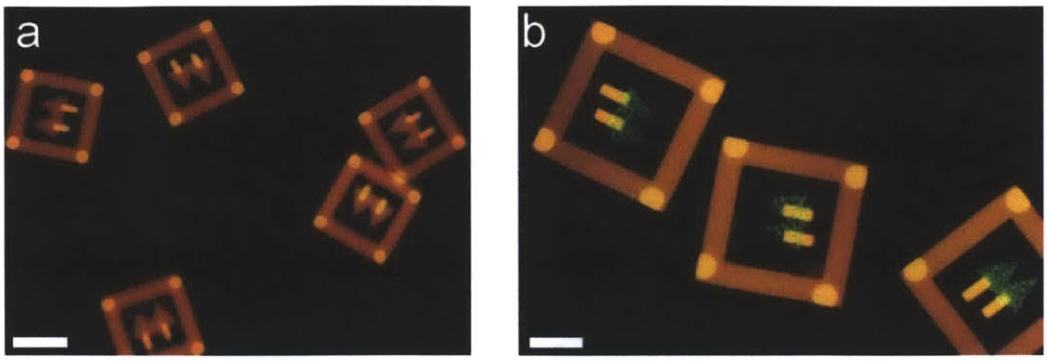

Figure 2.9: *Fluorescence microscopy images of multiple composite particles with different orientation. (a) Composite particles with "fall trees" in a frame. (b) Composite particles with "spring trees" in a frame. Scale bar is 100 μm.*

2.5 LRL for Functional Particle Synthesis

We exploited the ability to spatially arrange multiple chemistries in Lock Release Lithography to prepare particles diverse functionalities. The overlap regions of multi-functional particles can be designed to provide interwoven chemistries or excluded chemistries, depending on the pore size of the initial material and the size of entities included in subsequent monomers. When the pore size is large enough for molecules to leech in, the result is an interwoven blend of the two chemistries. However, when entities included in the monomer blend are larger than the pore size of the existing structure, those entities are excluded from the overlap region, resulting in a segregation of chemistries. Examples of interwoven and excluded chemistries are shown in Figure 4a. We prepared "Venn diagram-like" particles to investigate the incorporation of chemistries in the overlap regions. The first chemistry was a pure PEG hydrogel with a pore size expected to be ~ 1 nm [104]. The second chemistry was PEG with the addition of rhodamine-acrylate and 50 nm green fluorescent beads. As can be seen, the fluorescent monomer penetrated the initial gel structure and was incorporated in the overlap region while the colloidal entities were excluded. Figure 2.10b shows a DNA detector particle18 with distinct probe regions. The interior region and four wings contained DNA probe #1, while the other four wings contained probe #2. The particles were incubated with target #1 (which was labeled with green fluorescence, FITC) or both targets (target #2 was labeled with red fluorescence, Cy3) at 10nM at 37C for 30min. Fluorescence images confirm that the target oligomers hybridize only with their complementary probe regions. We also generated particle with opposing chemistries – specifically swelling and non-swelling. Swelling chemistries were achieved using PEG/acrylic acid monomer blends, which are well-known to be responsive to changes in pH. We made particles with a cross-shaped support and pH-responsive, fluorescent fins between each arm (Fig. 2.10c-e). In acidic conditions (pH ~ 3), these particles keep their original 2D body (Fig. 2.10c), while in neutral to alkaline conditions (pH ~ 8), the responsive fins bloom to form a 3D flower-like structure (Fig. 2.10d and e).

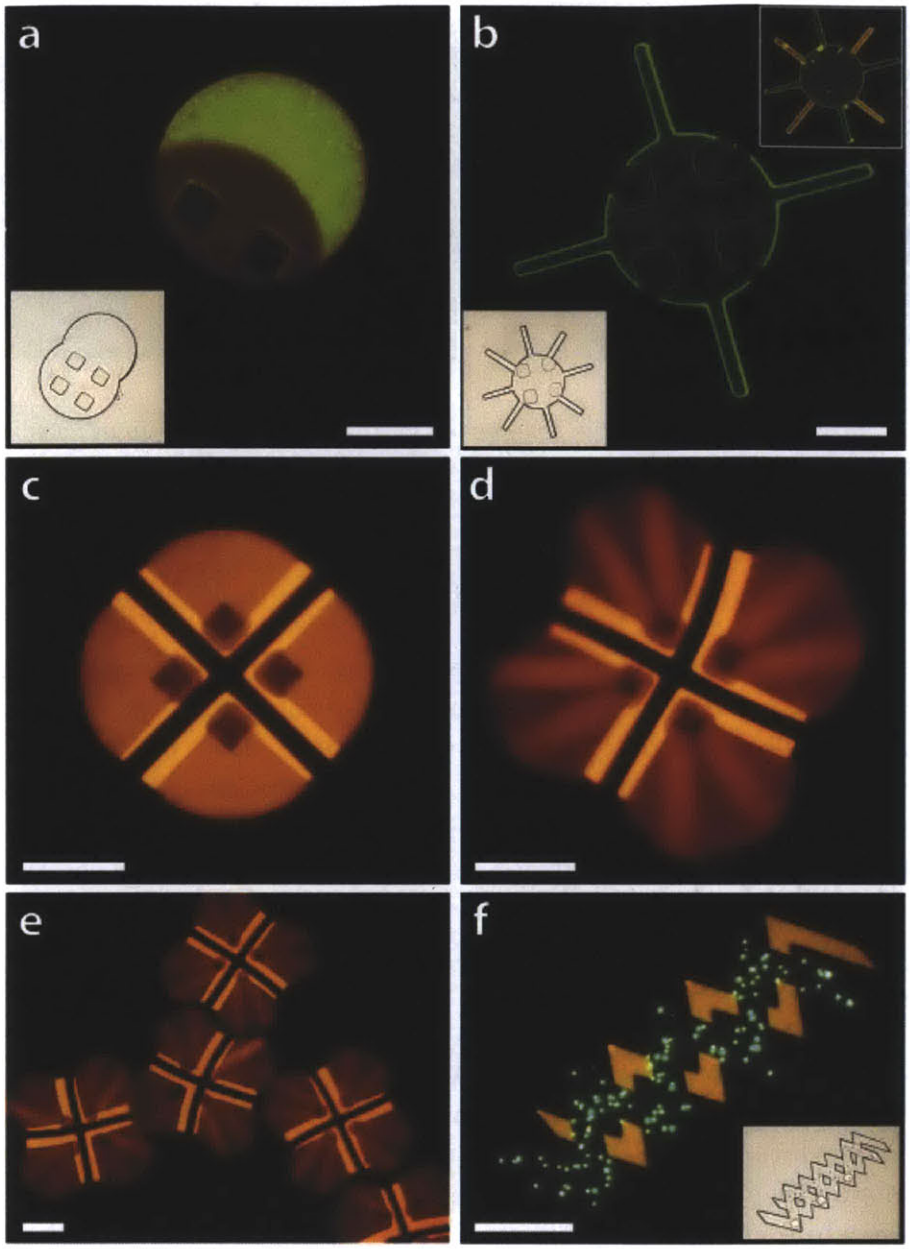

Figure 2.10: *Functional particles. (a) Fluorescence and DIC images of "Venn diagram" particle demonstrating interwoven (fluorescent monomer, orange) and excluded chemistries (beads, green) in polymerization overlap region. (b) Fluorescence and DIC images of a DNA detector particle with distinct probe regions. Shown are fluorescent images of a particle after incubation with target #1 (green) or both targets #1 (green, insert in the top right corner). and #2 (red, insert in the top right corner). (c) – (e) Fluorescence images of particles with pH-responsive fins and a cross-shaped rigid support. The particle keeps its original 2D circle shape in low pH (c) while in an alkaline pH, the fins bloom to form a 3D flower-like structure (d). (f) Fluorescence and DIC images of overlapping zig-zag-shaped particles with encapsulated entities. One strand contains 2 μm green fluorescent beads while the other has 5 nm red fluorescent streptavidin protein. In all DIC images, particles have been outlined for clarity. Scale bars are 50 μm (a,b), and 100 μm (c-f).*

Lastly, we demonstrate the generation of particles with various encapsulated entities that are organized in complex hierarchies. We made particles with overlapping zig-zag-shaped chemistries, one of which was laden with 2 μm fluorescent beads (FITC, green), and the other with 5 nm fluorescent protein (streptavidin-phycorytherin, red) (Fig. 2.10f). This process can be used to encapsulate living cells, stimuli, or nutrients with precise control over position, which has implications for applications in tissue engineering. Compared to other hydrogel particle-based approaches to engineering tissue constructs [4], we can prepare more precise and intricate building blocks in a scalable and highly homogeneous manner.

2.6 Summary

We have demonstrated that lock release lithography can be used to easily generate a diverse range of 3D and multifunctional composite particles through the association of channel topography, mask features, and pressure-induced channel deformation. The computer-automated method provides high resolution and high-throughput, similar to that seen in standard stop-flow lithography [73]. Also, locked structures can be built upon to generate complex, composite particles with a broad range of potential chemistries, interwoven or excluded, with incorporated entities including nucleic acids, proteins, or cells. For example, the length scales in LRL are ideally suited to generating tissue engineering mesoconstructs each containing multiple cell lines which are precisely positioned within the particle [4, 40]. In addition, the juxtaposition of swelling and stiff materials can be exploited to create particles that can undergo dramatic shape changes. Degradable polymers can be used to create microparticles which controllably evolve or fragment over time. We envision that this technology will provide a simple but powerful means to mass-produce functional units for microfluidic operations, filtration systems, and tissue engineering constructs.

Chapter 3

Hydrodynamic Focusing Lithography

Diverse patterns of flows in microfluidic channels have been utilized with great interests in the field of mixing, separation, and flow cytometry for high throughput analysis of chemical reagent or biomolecules. In this section, we describe a new approach, hydrodynamic focusing lithography (HFL), in which the structuring of fluids in microflows combined with lithography is exploited to create large arrays of functional microparticles. Contrary to our prior flow lithography method, here the flows are stacked in multiple dimensions. We also demonstrate the utility of this process in patterning of proteins.

3.1 Introduction

Biocompatible multifunctional particles hold great promise for drug delivery [1], imaging [31], and construction of building blocks [22, 105] for dynamic meso-structures such as self-assembled tissues [4] and 3D electrical circuits [34]. Of particular interest, multifunctional particles with unique barcodes have been suggested as diagnosis tools for rapid screening of biomolecules [7]. For these applications, particle design is at least as important as size [106-108] and requires a fabrication technique with precise control over shape and chemical patchiness. Methods currently used to generate multifunctional particles include microcutting [65], cojetting [64], core/shell system [62], photo resist-based lithography [48] and the PRINT method [53]. The morphology of particles prepared by cojetting, microcutting and core/shell systems has been limited to spheres and cylinders [62, 64, 65].

Although multilayer lithography overcomes this limitation [48], the use of photoresist materials renders this approach non ideal for many applications. While the PRINT method [53] has its strength in producing small submicron particles, to date multiphasic particles beyond a 1-D stripe have not been synthesized. Furthermore, during multifunctional particle synthesis, the technique needs multiple steps and does not provide flexibility as particle shapes are restricted to the pre-defined stamping molds. Previously, we have shown that flow lithography (FL) can be used to generate multifunctional particles – we exploited several microfluidic characteristics such as co-flow of liquid monomers, rapid fluidic exchange, and simple controllability [72, 73, 109]. In FL, we can use a combination of adjacent flowing photocurable monomers with lithographic masks to simultaneously define the shape and chemical pattern of particles [72, 73]. Recently, we also developed lock release lithography (LRL) to extend chemical patterning to multiple dimensions [109]. However, these FL-based approaches for generating particles with patterned chemistries require precise alignment of masks at flow interfaces and concomitant modest particle throughput. Currently, FL cannot be used to synthesize multifunctional particles with chemical anisotropy in the channel height direction. Here, we introduce a new method called hydrodynamic focusing lithography (HFL) that harnesses flow focusing to create stacked flows in two-layered channels for particle synthesis. Contrary to our prior methods to create multilayered particles, here the fluid interface can be perpendicular to the UV light propagation direction and precise mask alignment at the interface is no longer needed. This change in geometry also allows us to polymerize 2-D arrays, compared to 1-D in the prior method, which can increase throughput dramatically. In HFL, multiple monomer streams can be simultaneously stacked in both the z- and y-direction leading to more complex particles than before. Finally, we demonstrate that particles prepared by HFL can be combined with capture proteins on selected layers.

3.2 Experimental Methods

Materials

All of the particles shown in Figure 2, and 3 were made using solutions of 60% (v/v) poly(ethylene glycol)(700) diacrylate (PEG-DA, Polysciences), 5% (v/v) Darocur 1173 (Sigma Aldrich) initiator, 30% (v/v) 1X TE buffer and 5% (v/v) fluorphores. Fluorphores were 100 nm blue fluorescent beads (Polysciences), 200 nm green fluorescent beads (Polysciences) and the fluorescent methacryloxyethyl thiocarbamoyl rhodamine-A (Polysciences), respectively. Particle regions for protein coupling were made from solutions comprised of 60% (v/v) poly(ethylene glycol)(700) diacrylate (PEG-DA, Polysciences), 5% (v/v) Darocur 1173 (Sigma Aldrich) initiator and 35% (v/v) biotin-PEGA in PBS. Biotin-PEGA solution was prepared by mixing NHS-PEG(2000)-acrylate (Laysan Bio inc.) and biotin-hydrazide (Polysciences) as 1:1 molar ratio in PBS buffer.

Microfluidic Device and SFL Setup

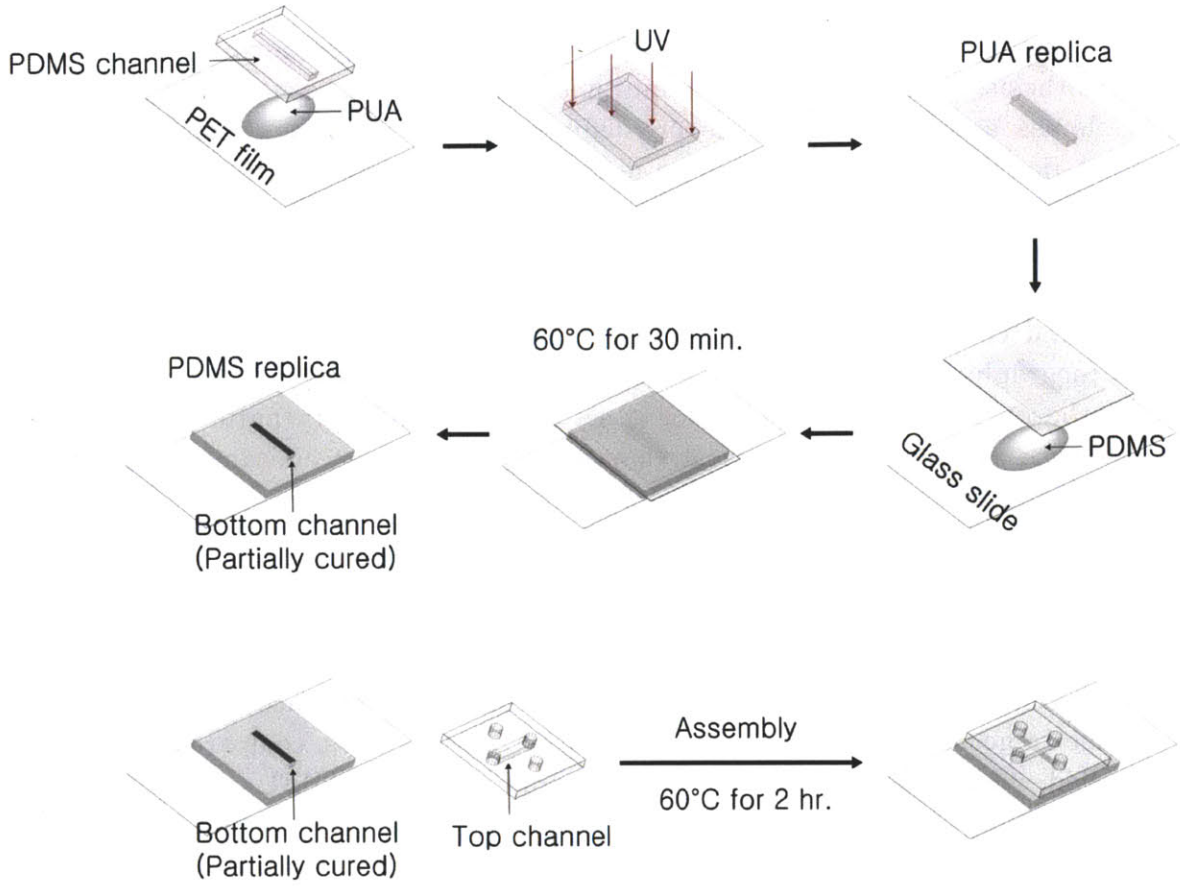

Figure 3.1: *A schematic diagram for fabrication process of oxygen permeable two-layered PDMS channels. A partially cured PDMS bottom channel is prepared on a glass slide via PDMS-PUA-PDMS replica molding technique. Then, a top PDMS channel is assembled on the bottom channel generating a two-layered gas permeable PDMS channel.*

Flow lithography is made possible by the presence of a lubrication layer at the channel walls, which results from the quenching of free-radical reaction at the channel walls via oxygen that has diffused through the polydimethoxysilane (PDMS) [75]. Typically, two-layered PDMS devices are irreversibly sealed using oxygen plasma activation [110, 111]. However, the activated surfaces covered with silanol groups are less permeable to oxygen, diminishing the presence of a suitable lubrication layer. Although PDMS sacrificial layers could be used during plasma treatment to avoid oxidizing specific regions of the devices, the method leads to imperfect sealing with the potential of leaking. We observed that layered flows in these devices were frequently mixed as a result of leaking. Alternatively, channels can be sealed using the technique of partial curing, device fabrication, and complete curing. This method is preferred when fabricating two-layered homogeneous PDMS channels for flow lithography. Figure 4.1 shows the fabrication process of gas permeable two-layered

PDMS channels. PDMS channels are generated by pouring PDMS (mixed at 10:1 base:curing agent) over an SU-8 master (Stanford Foundry) and then curing 2 hr at 60 °C in an oven. To prepare a partially cured bottom PDMS channels on a glass slide, we used a PDMS – polyurethane acrylate (PUA) – PDMS replica molding technique [112]. Briefly, a droplet of PUA was put on a flat polyester (PET) film and sandwiched between the film and a PDMS mold. The PUA was exposed to UV (365 nm) for 1 min and the PDMS mold was removed to give a PUA mold on PET. In a similar manner, this PUA mold was used with a droplet of PDMS to form a partially cured PDMS channel bottom after curing for 25 min at 60 °C. To finish the construction of a two-layered PDMS device, a PDMS mold with the top channel was assembled on the bottom channel and the device was fully cured at 60 °C for 2 hr. Finally, SFL setup was same with Chapter 2.

3.3 Particle Synthesis in Stacked Monomer Flows

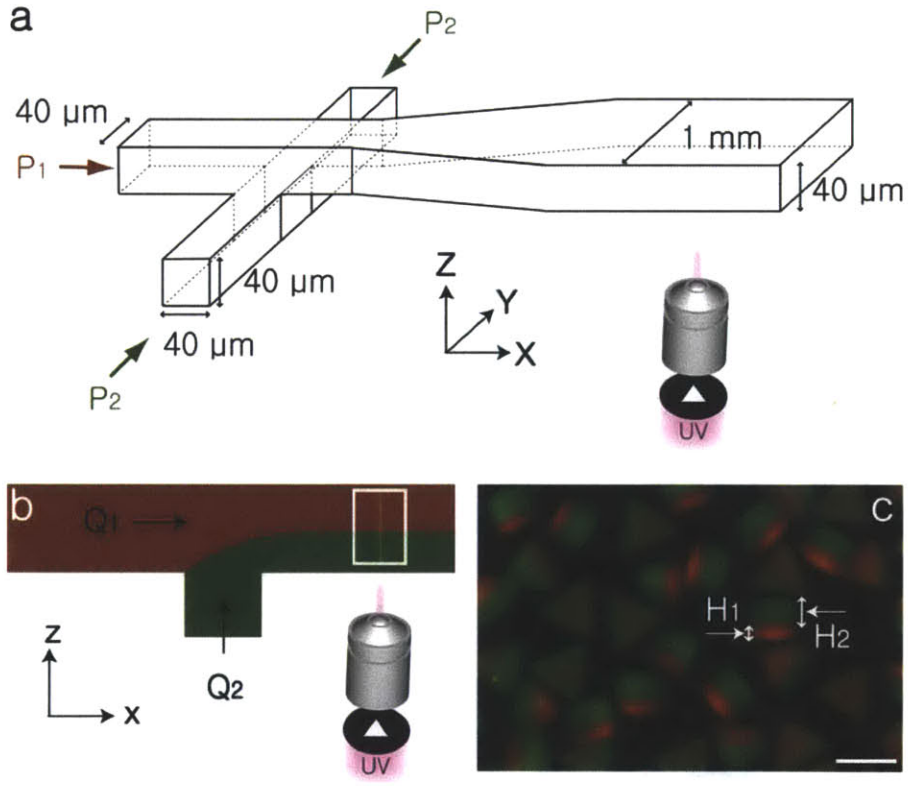

Figure 3.2: *Hydrodynamic focusing lithography (HFL) for high-throughput synthesis of Janus microparticles. (a) Schematic description for the creation of layered monomer flows. P_1 and P_2 represent the inlet pressures of top and bottom channel respectively. All inlet dimensions are 40 μm X 40 μm. Particles are synthesized after layered flows are widened up to 1 mm in a 40 μm tall region of the channel. (b) A side view of flow focusing and particle polymerization. (c) A fluorescent image of 50 μm triangular particles with green (200 nm, green fluorescent beads) and red (Rhodamine-A) layers. H_1 and H_2 are the heights of top (red) and bottom (green) layer in a particle. Scale bar is 50 μm.*

Figure 3.2a shows a typical channel used for particle synthesis. Narrow channels (40 μm) were used to minimize mixing as stacked streams were introduced, providing stable layered flows in the z-direction [110, 112]. Further along the channel, the flows are widened up to 1 mm for particle synthesis. Like other flow lithography techniques [72, 73, 109], HFL can be applied to a broad range of precursor materials. As before, we use monomers based on poly(ethylene glycol) that are bio-friendly, and can be functionalized with a variety of biomolecules. As the prepolymer solutions we employ here are miscible, we can neglect the effect of surface tension between layered flows. Figure 3.2b shows the particle synthesis process in a 2D side view. We first flow a prepolymer solution with red fluorophores, rhodamine acrylate. We then flow a second prepolymer solution with 200 nm green fluorescent beads. After that, we synthesized bifunctional, triangular PEG hydrogel particles in the stacked monomers. In this method, the fluid interface could be perpendicular to the UV light propagation direction and precise mask alignment at the interface is no longer needed. As shown in Figure 3.2c, the layered flows could be used to introduce chemical anisotropy in the z-direction of particles. The relative thickness of each chemical region, H_1 and H_2, could be readily controlled by adjusting the ratio of inlet pressures.

3.3.1 Throughput and Uniformity for Synthesis of Striped Particles

To mass-produce layered particles in the two-layered PDMS channels, we used stop flow lithography (SFL). As mentioned earlier, during multifunctional particle synthesis, traditional SFL requires precise mask alignment across the interface and each synthesis step polymerizes only 1-D rows of particles. The change in orientation of the fluid interface in HFL allows for production of 2D arrays in each step. With a circular polymerization region of radius D and a particle dimension L, synthesis throughput per cycle is approximately $\pi D^2/4L^2$ for a 2D array of particles in comparison to D/L for a single row. In our current setup, D is approximately 1 mm and taking a particle dimension of 5 μm, the throughput is increased by more than 200×. Furthermore, resolution of layer heights is now controlled by automated flow rather than manual mask alignment.

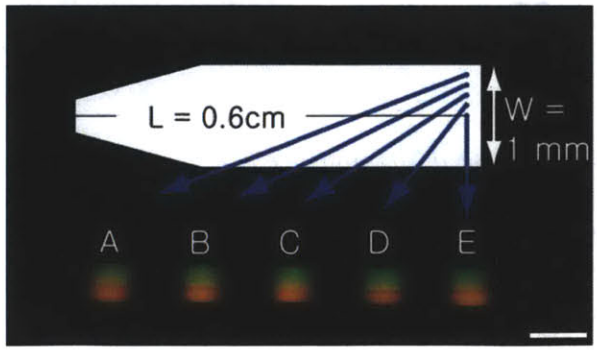

Figure 3.3: *Uniformity of Janus particles synthesized at A, B, C, D and E spots across a 1 mm width channel. The intervals between spots are 100 μm. Scale bar is 50 μm.*

We also demonstrated that during synthesis with HFL, particles with uniform dimensions are generated across the channel width. It is known that PDMS channels deflect under pressure-driven flows, giving a local channel height that is dependent on the position [99]. In this view, continuous flow lithography (CFL) [72] is not compatible with HFL as layer thicknesses will be different at each location. However, SFL can be used to yield uniform layered particles without position dependency since polymerization occurs at zero applied pressure, after the PDMS channel has recovered from a deflected state - as long as the stop time (t_s) is longer than the time required for channel relaxation (t_r). The relaxation time is dependent on channel width, channel height, viscosity of the solution, and distances from inlets [73]. At 0.6 cm downstream in a 1 mm wide channel with 40 μm heights, tr is estimated to be 0.07s [73]. Also, the polymerization time (t_p) should be kept to a minimum in order to prevent species diffusion between layers. Using t_r of 300 ms and t_p of 50 ms, we showed that layered particles with uniform features were generated across the channel width (Fig. 3.3).

3.3.2 Top-down Particle Design

As shown in Figure 3.2, we synthesized bifunctional, triangular polyethylene glycol particles comprised of an upper layer with rhodamine-acrylate and a bottom layer containing 200 nm green fluorescent beads. In the synthesis of the particles, we control the thickness of each chemical region in a predictive way. To demonstrate this, we produced triangular particles with high aspect ratio on several conditions of volumetric flow rates. As most particles were toppled, we easily measured the thickness of each chemical region. Then, we compared the results with the estimated values by a simple model that predicted a curve for the relation between measured H_2/H_1 and Q_2/Q_1 (Fig. 3.4). When the thickness of each chemistry is much larger than the oxygen inhibition layer thickness, the ratio of H_2/H_1 is approximately same as the ratio of Q_2/Q_1. As shown in the below graph, the estimation compared well with the experiments. We were able to precisely tune the layer height from 32 to ~4.5 μm.

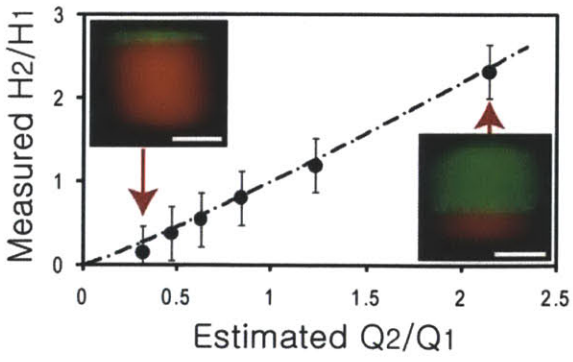

Figure 3.4: *Comparison of measured H_2/H_1 versus estimated flow ratio Q_2/Q_1. A simple hydrodynamic resistance model predicts a curve for the relation. Scale bar is 20 μm.*

We recall that HFL (and SFL) can quickly stop and start the flows (polymerizing features in the stop regime) because they control pressure at the inputs, whereas sources that directly control flow rates (e.g. syringe pumps) typically have a slow response time. As a result, we developed a hydrodynamic resistance model to estimate volumetric flow rates from inlet pressures. This model was analogous to Ohm's laws. We calculated hydrodynamic resistances from channel geometries, and converted pressure differences to volumetric flow rates using the resistances. We make the following assumptions in our model: (1) Newtonian, incompressible, fully developed and laminar flows, (2) negligible surface tension between solutions, and (3) viscosity μ is the same in all inlet flow streams.

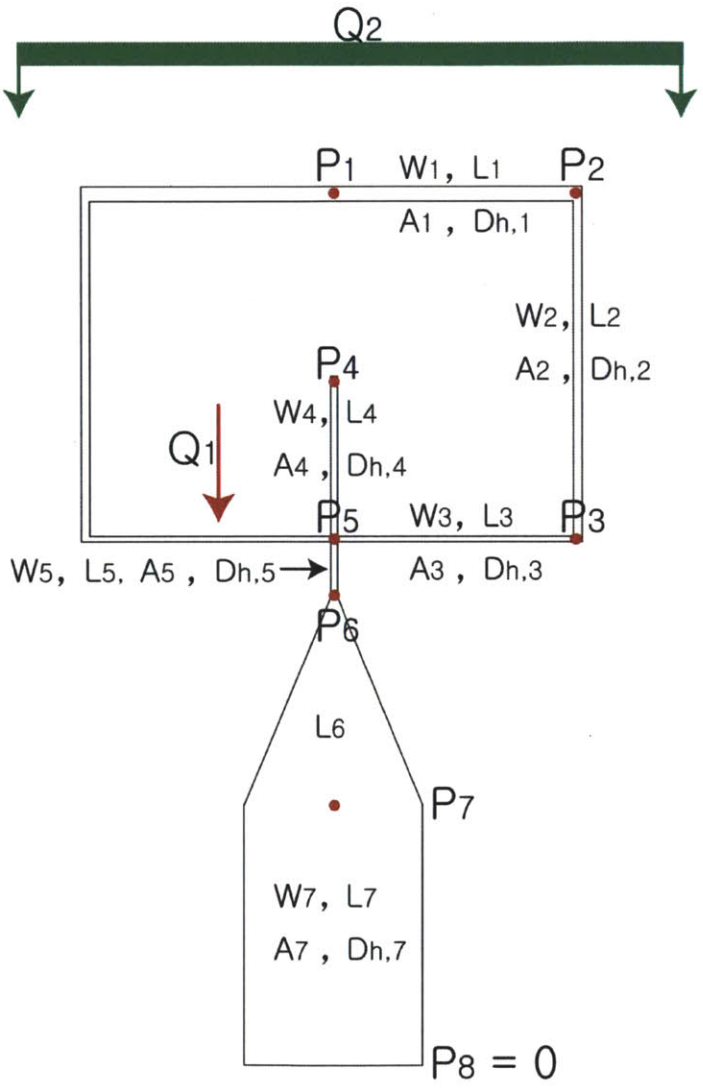

Figure 3.5: *A schematic description of a PDMS channel used for creation of two layered flows.*

Width	μm	Area	μm²	Hydraulic diameter	μm	Length	μm
W_1	200	A_1	8000	$D_{h,1}$	67	L_1	3773
W_2	100	A_2	4000	$D_{h,2}$	57	L_2	5430
W_3	40	A_3	1600	$D_{h,3}$	40	L_3	3773
W_4	40	A_4	1600	$D_{h,4}$	40	L_4	3217
W_5	40	A_5	1600	$D_{h,5}$	40	L_5	520
						L_6	2000
W_7	500	A_7	20000	$D_{h,7}$	74	L_7	3875

Table 3.1. *Geometries of a PDMS channel used for creation of two layered flows*

Then, for laminar flow in a pipe, we can express the volumetric flow rate Q as the following equation (3.1),

$$Q = \frac{AD_h^2}{32\mu L}(P_{loss}) \tag{3.1}$$

Here, the hydraulic diameter (D_h) of rectangular tubes is given by the following equation (3.2).

$$D_h = \frac{2ab}{a+b} \tag{3.2}$$

Where a is the width of a pipe and b is the height of a pipe. From Figure 3.5 and the equation (3.1), we can write the following equations.

$$\frac{A_1 D_{h,1}^2}{32\mu L_1}(P_1 - P_2) = \frac{A_2 D_{h,2}^2}{32\mu L_2}(P_2 - P_3) = \frac{A_3 D_{h,3}^2}{32\mu L_3}(P_3 - P_5) \tag{3.3}$$

$$\frac{A_4 D_{h,4}^2}{32\mu L_4}(P_4 - P_5) + \frac{A_1 D_{h,1}^2}{32\mu L_1}(P_1 - P_2) = \frac{A_5 D_{h,5}^2}{32\mu L_5}(P_5 - P_6) \tag{3.4}$$

$$\frac{A_5 D_{h,5}^2}{32\mu L_5}(P_5 - P_6) = \frac{A_7 D_{h,7}^2}{32\mu L_7}(P_7) = \frac{2H}{3\mu L_6}(P_6 - P_7)\frac{2W_5^2 W_7^2}{(W_5 + W_7)} \tag{3.5}$$

Solving the above equations, we can get the following pressure relations.

$$\begin{pmatrix} P_2 \\ P_3 \\ P_5 \\ P_6 \\ P_7 \end{pmatrix} = \begin{pmatrix} 0.95 & 0.0077 \\ 0.76 & 0.038 \\ 0.092 & 0.15 \\ 0.014 & 0.022 \\ 0.013 & 0.021 \end{pmatrix} \begin{pmatrix} P_1 \\ P_4 \end{pmatrix} \tag{3.6}$$

Using the relations, we can express the ratio of the volumetric flow rates as inlet pressures.

$$\frac{Q_2}{Q_1} = \frac{0.57P_1 - 0.092P_4}{0.85P_4 - 0.092P_1} \tag{3.7}$$

In table 3.2, we summarize the estimations of all intersection pressures (P_2, P_3, P_5, P_6, and P_7) and Q_2/Q_1 at given inlet pressures (P_1 and P_4),

$P_{1,inlet}$ (Psia)	$P_{4,inlet}$ (Psia)	P_2 (Psia)	P_3 (Psia)	P_5 (Psia)	P_6 (Psia)	P_7 (Psia)	Q_2/Q_1
3.0	5.0	2.9	2.5	1.0	0.15	0.15	0.31
4.0	5.0	3.8	3.2	1.1	0.17	0.16	0.47
5.0	5.0	4.8	4.0	1.2	0.18	0.17	0.63
5.0	4.0	4.8	4.0	1.0	0.16	0.15	0.84
5.0	3.0	4.8	3.9	0.9	0.14	0.13	1.23
5.0	2.0	4.8	3.9	0.8	0.12	0.11	2.14

Table 3.2. *Estimated pressures and Q_2/Q_1.*

Finally, we can derive a relation between H_2/H_1 and estimated Q_2/Q_1.

$$\frac{H_2}{H_1} \sim \frac{\frac{Q_2}{Q_1+Q_2} \times H_C - H_I}{\frac{Q_1}{Q_1+Q_2} \times H_C - H_I} = \frac{(H_C - H_I) \times \frac{Q_2}{Q_1} - H_I}{(H_C - H_I) - H_I \times \frac{Q_2}{Q_1}} \tag{3.8}$$

Where H_C is the channel height and H_I is the inhibition layer thickness. For our experiments, H_C is 40 μm and H_I is approximately 2 μm.

3.3.3 Multilayered Particles

We showed that multiple flows can be stacked by increasing the number of inlets entering sequentially from the bottom layer of the device (Fig. 3.6a). Using such multi-flow stacking, we synthesized triangular particles containing three layers (Fig. 3.6b and c). In the tri-layered flows, flow 1 was PEG-DA with 200 nm green fluorescent beads while flow 2 and flow 3 were PEG-DA with 100 nm blue fluorescent beads and PEG-DA with rhodamine acrylate, respectively. Considering the minimum chemical layer thickness of ~ 4 μm, we could generate particles containing 10 different chemical layers from a 40 μm channel. The aspect ratio of the layered particles is defined to be the ratio of the over-all particle height divided by the size of the feature produced by the transparency mask. Using variations of mask feature sizes in similar channels, we also generated particles with aspect ratios greater than (Fig. 3.7a) or less than 1 (Fig. 3.7b).

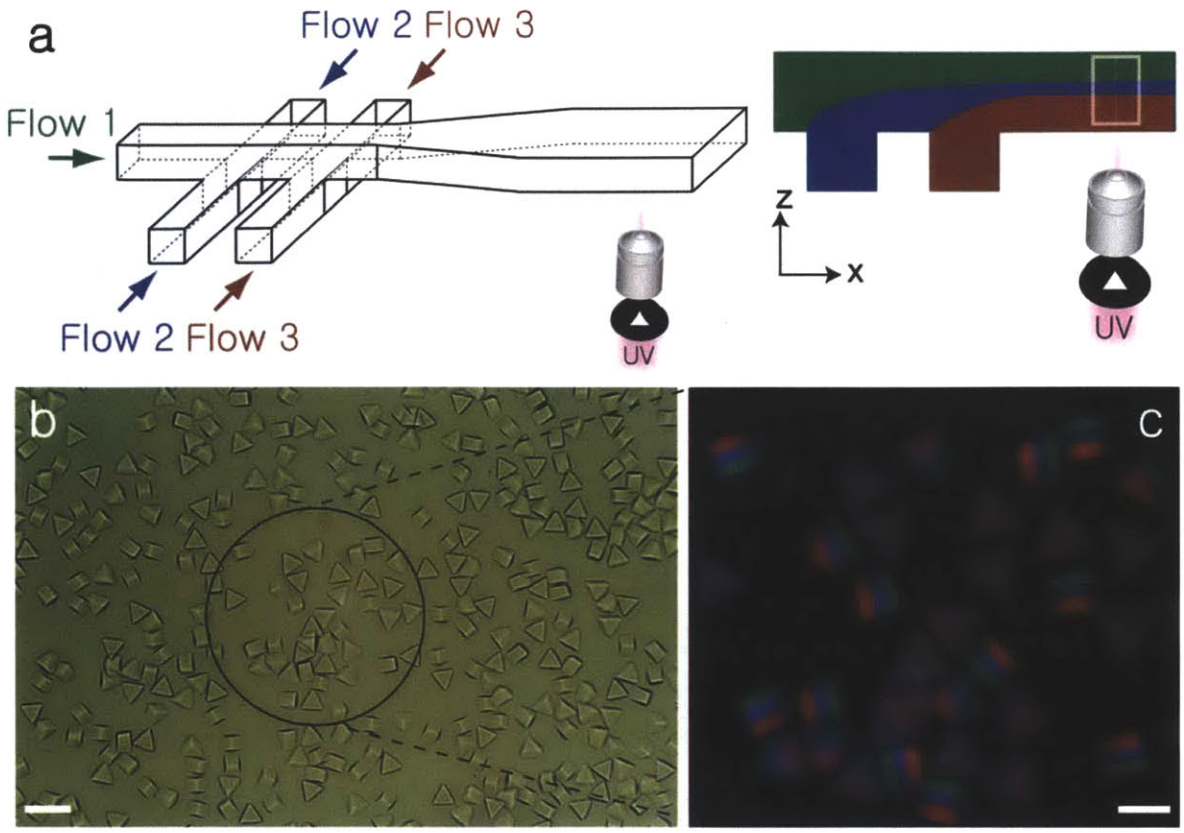

Figure 3.6: *Synthesis of multi-layered microparticles. (a) A schematic drawing for synthesis process of tri-layered microparticles. In the stable layered flow, tri-phasic triangular particles can be synthesized using a mask with triangles. (b) Differential interference contrast (DIC) image of 50 μm tri-layered triangular particles (c) Magnified fluorescent image for the circled region of (b). Scale bars are 100 μm (b) and 50 μm (c).*

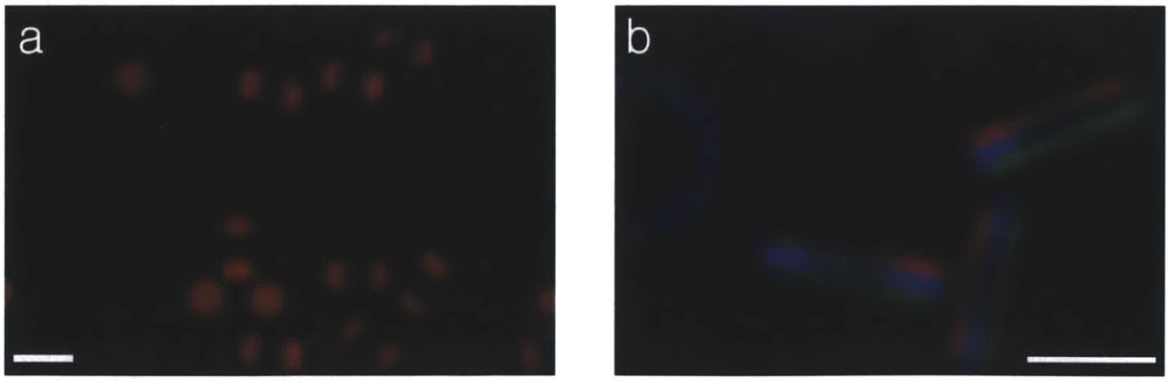

Figure 3.7: *Tri-layered microparticles with different aspect ratios (a) 20 μm pentagonal particles with aspect ratio 2. These particles contain rhodamine-acrylate in both top and bottom layers but no fluorophores in the middle layer. (b) 150 μm tri-layered ring particles with aspect ratio 0.4. Scale bars are 30 μm (a) and 100 μm (b).*

3.4 Particle Synthesis in Multidimensional Monomer Flows

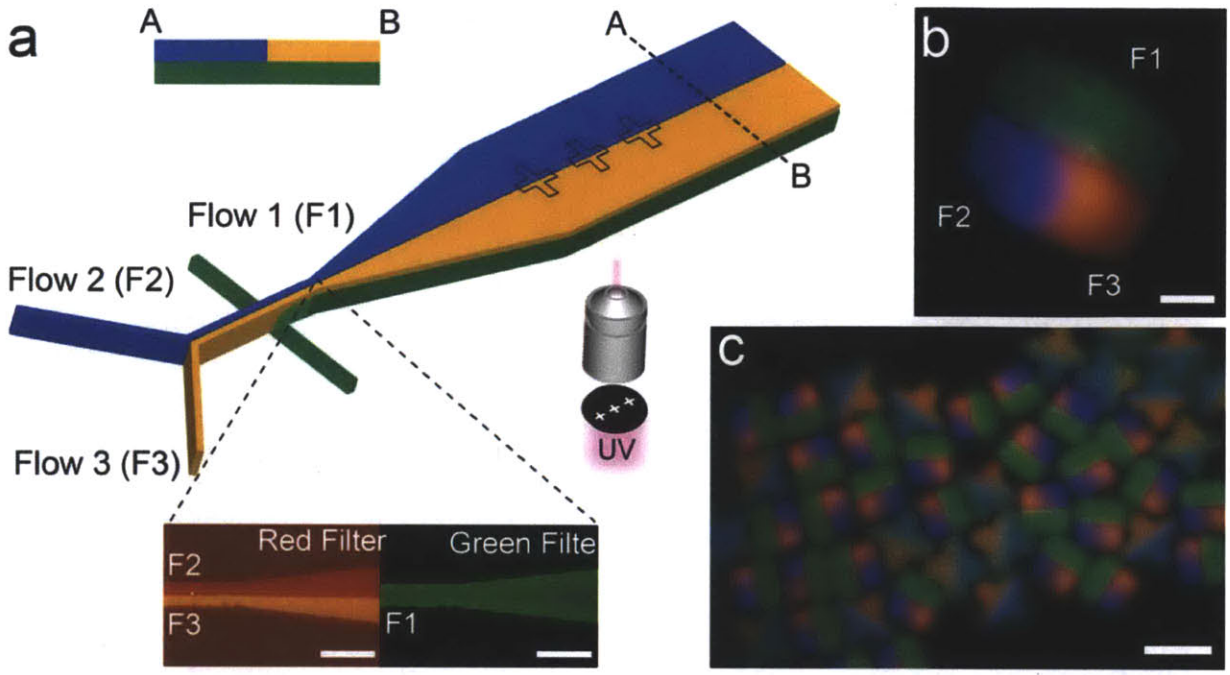

Figure 3.8: *Synthesis of dual-axis layered microparticles. (a) A schematic diagram for synthesis process of dual-axis layered microparticles. Flow 1 (F1), flow 2 (F2) and flow 3 (F3) contain 200 nm green fluorescent beads, 100 nm blue fluorescent beads and rhodamine-acrylates as fluorophores. Inserted fluorescent images show dual-axis flows in a two-layered PDMS channel. (b) A fluorescent image to show a side view of a 40 μm cross shaped particle with red, blue (in top) and green layers (in bottom) (c) A fluorescent image of mass-produced particles. Scale bars are 80 μm (b) and 10 μm (c).*

As perhaps the most valuable feature of HFL, the method can also be used for high-throughput synthesis of dual-axis multifunctional particles with mask-defined morphologies. Such particles have not previously been made in microfluidic devices. We generate a 2-D flow focusing [113] geometry by first co-flowing monomers F1 (PEG-DA with Rhodamin-A) and F2 (PEG-DA with 100 nm blue fluorescent beads) using two inlets of top channel. This flow is then stacked on monomer F3 (PEG-DA with 200 nm green fluorescent beads), which enters from the bottom channel. Shown in Fig. 3.8a are the layered flows that comprise the top (flow 1 and flow 2) and bottom layers (flow 3). Using a transparency mask with a single row of features, we synthesized cross-shaped particles with dual-axis functionality at the interface of flows (Fig. 3.8b and c). Although the production rate for this process is similar to that of traditional SFL due to the necessity of 1-D row synthesis, the process extends the degree of freedom for chemical anisotropy in a particle to two dimensions. Furthermore, the multidimensional flows can be layered in a scalable way. We generated 4 layered flows which contained in their center side-by-side stacked monomers which were bounded on the top and bottom by a third monomer stream (Fig. 3.9).

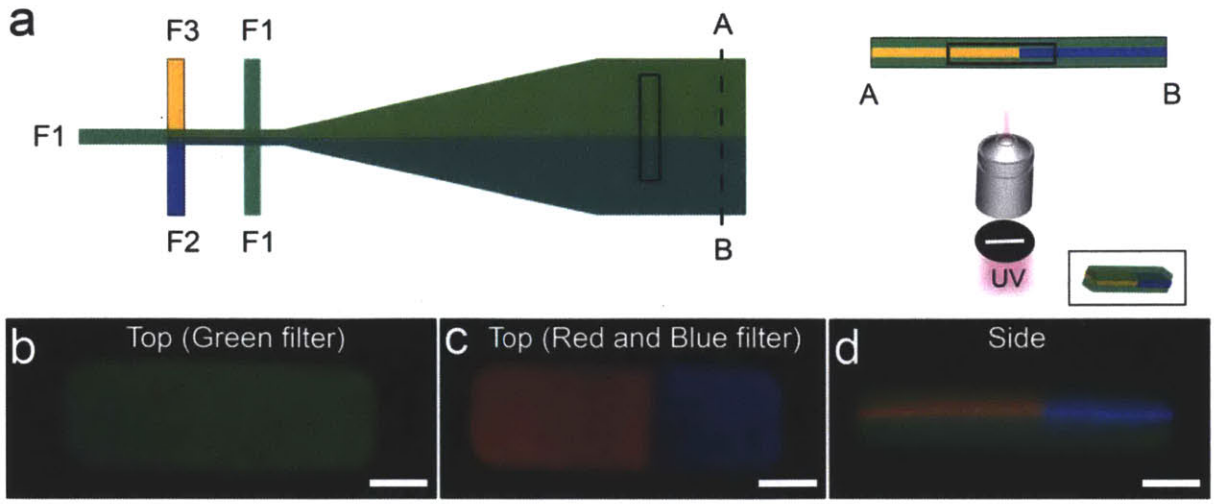

Figure 3.9: *Synthesis of four-layered sandwich microparticles. (a) A schematic diagram for synthesis process of four layered sandwich particles with dual layers in the middle. A-B is the intersection of the channel with dual-axis four layered flows. (b)-(d) Fluorescent images of a sandwich particle generated by the process in (a). Scale bars are 50 μm.*

To achieve this, flow 3 was introduced in at both the top and second bottom channel, while the monomers contained in the middle layer were combined at the first bottom inlet. Using a mask of rectangular shapes with rounded corners, we synthesized sandwich-like multifunctional particles at the interface of the two flows in the middle layer (Fig. 3.9a). As shown in Figure 3.9b-d, the sandwich particles had green fluorescent top and bottom layers (Fig. 3.9b) with red and blue fluorescent layers comprising the middle (Fig. 3.9c). For such dual-axis particles, chemical anisotropy in the y-direction can be controlled by mask alignments at the flow interface.

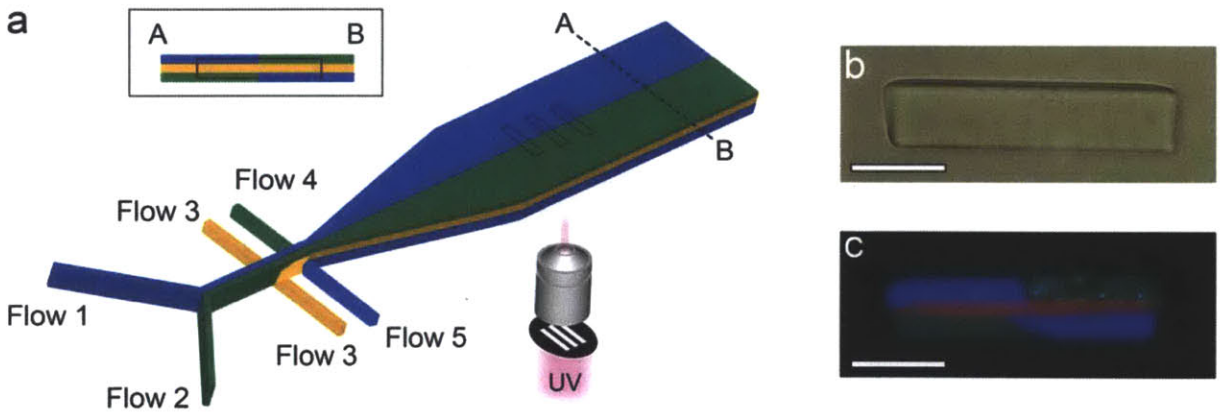

Figure 3.10: *Synthesis of five-layered sandwich microparticles. (a) A schematic diagram for synthesis process of five layered sandwich particles with dual layers in the top and bottom. A-B is the intersection of the channel with dual-axis five layered flows. (b-c) DIC and fluorescent images of a sandwich particle generated by the process in (a). Scale bars are 50 μm.*

5 layered flows were also generated as shown in Figure 3.10. The center consisted of a monomer while the top and bottom comprised of side-by-side stacked monomers. A particle synthesized in the structured flows is shown in Figure 3.10b and c. As shown in these examples, the number of layers in a particle is less than or equal to the number of inlet flows because a layer can be generated from multiple inlet flows. Using this process, virtually any number of flows can be stacked.

3.5 Protein Coating on Particle Surfaces

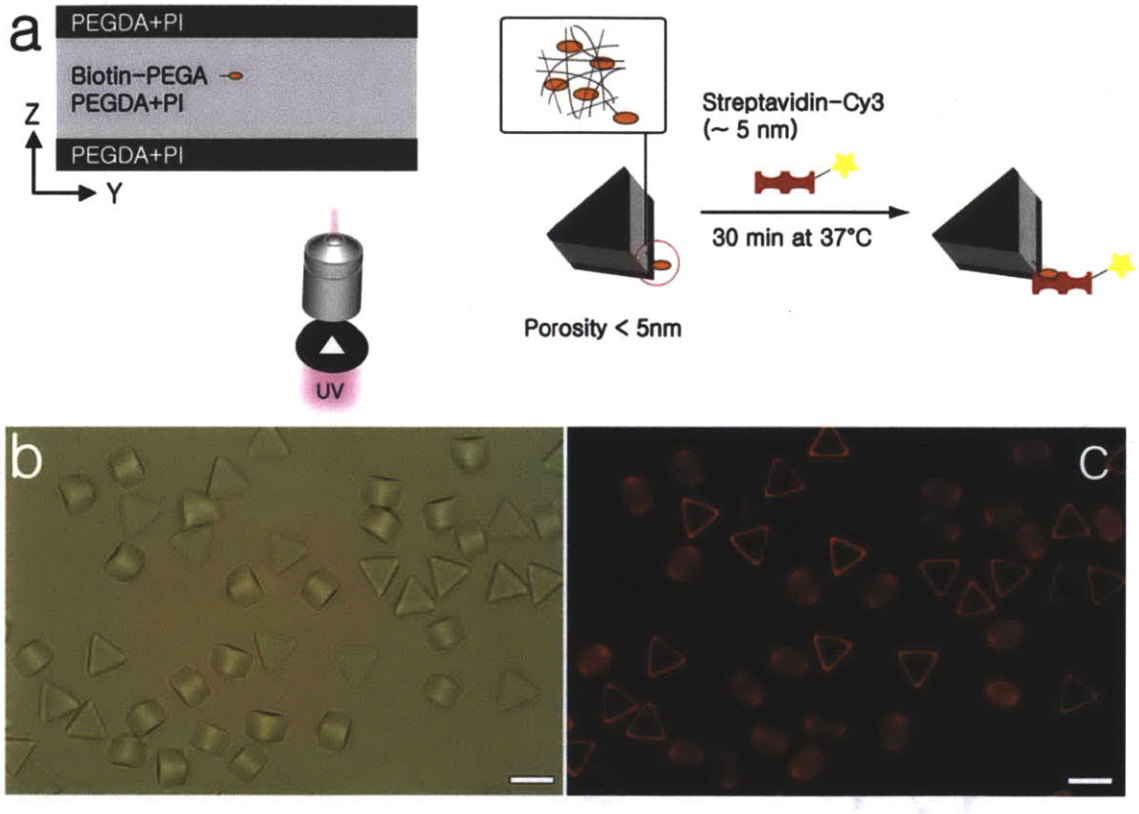

Figure 3.11: *Protein conjugation on particle sides. (a) A schematic diagram for preparation of triangular particles with patterned protein coatings. The middle flow contains biotin-PEGA that is copolymerized in the particle. After incubation, the triangular particles are coated with streptavidin-cy3 on the sides. (b) A DIC image of the protein coated triangular particles. (c) A fluorescent image of (b). Scale bars are 50 μm.*

Finally, we demonstrate that particles prepared by HFL can be patterned with proteins on a specific layer. These "caps" can be used to restrict target capture to specific particle faces (Fig. 3.11) To achieve protein capturing, we first synthesized biotin-PEG-Acrylate by mixing 1:1 molar mixture of biotin-hydrizide and acrylate-PEG-succinimidyl ester in 1X PBS buffer and used this as an anchor to attach streptavidin. This allows us to directly co-

polymerize biotin in a selected region of the particle. The trilayer flow is shown schematically in Figure 3.11a, and the acrylated biotin is in the center flow. The resulting synthesized triangular particles are shown in Figure 3.11b. Next, streptavidin-Cy3 was incubated with the particles at 37 °C for 30 min. The streptavidin-Cy3 will strongly associate with the biotin. As the size of streptavidin (~ 5 nm) was bigger than the porosity size of the hydrogel networks [104, 109], proteins were coated on sides of particles. In Fig. 4C, the fluorescence pattern indicates that proteins were not bound to top and bottom layers. Furthermore, the resulting specific association shows that the biotin is still active after UV-polymerization, akin to our prior work with nucleic acids [7]. The short UV exposure dose required for synthesis is the most likely reason that bio-activity is retained

3.6 Summary

In this section, we have presented a new technique called hydrodynamic focusing lithography (HFL) that combines flow-stacking and microfluidic particle synthesis. In HFL, the layered flows can be used to introduce chemical anisotropy in z-direction of particles. The top-down particle design was achieved by a simple hydrodynamic model. For certain applications, the approach can increase the throughput of multifunctional particle synthesis over 200 times when compared to traditional stop-flow-lithography. We have also demonstrated that HFL can be used to produce dual-axis layered particles. To achieve this, multidimensional stacked flows were used to synthesize the complicated particles, and layered in a scalable way. The flows were further engineered in a predictive fashion. Lastly, as a demonstrative application, we showed surface functionalization of particles patterning proteins on a specific layer. HFL is a compelling method as the technique is compatible with other flow lithographic methods such as LRL [109] and stop flow interference lithography (SFIL) [102]. For example, the combination of HFL and LRL can lead to chemical patterning in all dimensions as LRL can offer chemical isotropy of particles in x-y dimension [109]. We have believed that HFL can provide a powerful way to reach new complex particles.

Chapter 4

Oxygen-Free Flow Lithography

FL currently relies on the use of polydimethylsiloxane (PDMS) microchannels because the process requires local inhibition of polymerization near channel interfaces via oxygen permeation. The dependence on PDMS devices greatly limits the range of precursor materials which can be processed in FL. Utilizing an initiated chemical vapor deposition (iCVD) nano-adhesive bonding technique to create non-PDMS based devices, here we present oxygen-free flow lithography via inert fluid lubrication layers for the synthesis of new classes of complex microparticles. We successfully synthesize microparticles with a sub-second residence time and demonstrate on-the-fly alteration of particle height. This technique greatly expands the synthesis capabilities of FL, enabling particle synthesis using water-insoluble monomers, organic solvents, and hydrophobic functional entities such as quantum dots (QDs) and single-walled carbon nanotubes. As one demonstrative application, we created near-infrared barcoded particles for real-time, label-free detection of target analytes.

4.1 Introduction

Current FL protocols require polydimethylsiloxane (PDMS) channels to allow for the permeation of oxygen into the synthesis chamber for inhibition of polymerization near channel interfaces. This localized inhibition layer enables the production of mobile particulates (as opposed to fixed structures) that can be transported out of the synthesis area via flow [72]. The current dependence on PDMS places restrictions on both device

construction (e.g. glass or plastic cannot be used) and prevents the use of solvents and/or monomers that swell PDMS. Employing an iCVD nano-adhesive bonding procedure to construct a new class of non-PDMS devices, we now present oxygen-free FL, a versatile particle synthesis method that uses inert fluid lubrication layers to achieve new levels of chemical complexity. By vertically layering multiple laminar flows within this new generation of devices, we produce anisotropic particles using sub-second residence times without oxygen lubrication layers and tune particle heights on demand by adjusting flow parameters. We further estimate maximum residence time for particle synthesis, evaluating physical and kinetic properties such as flow layer thickness, critical gel point, and diffusivity. Finally, we demonstrate solvent-based synthesis of complex anisotropic particles from structured microflows of water-insoluble monomers and particles encapsulating hydrophobic functional entities such as ruthenium, quantum dots (QDs) and single-walled carbon nanotubes (SWNTs). Using this approach, we synthesize graphically encoded particles that bear near-infrared-active QDs in the "code" region and SWNTs in a separate "probe" region designed for label-free, real-time detection of target molecules. The novel techniques described here greatly enhance the synthesis capabilities of FL and further expand the library of chemically and geometrically complex microparticles that can be produced.

4.2 Experimental Methods

Materials

For swelling experiments, we used an organic solvent comprised of 98% (v/v) toluene (EMD Chemical Inc.) containing 2% (v/v) magnetic nanoparticles solution (EMG 905, Ferrotec, for visualization). PEG structures inside NOA devices were generated from a monomer solution containing 60% (v/v) PEG-DA 700 (Sigma Aldrich), 10% (v/v) 2-hydroxy-2-methylpropiophenon (PI, Sigma Aldrich), and 30% (v/v) PEG 200 containing 20 mg/ml of red acrylate 13 (Sigma Aldrich). PEG particles encapsulating ruthenium were synthesized using solution of 84% (v/v) PEG-DA 200 (Sigma Aldrich), 10% (v/v) PI, 1% (v/v) NVP (Sigma Aldrich), and 5% (v/v) ruthenium complex (II) dye solution. The dye solution was prepared by dissolving dichlorotris(1,10-phenanthroline) ruthenium (II) hydrate (Sigma Aldrich) powder into a mixture of methanol and toluene (4:1, v/v) at a concentration of 5 mg/ml. Other PEG particles were made of the composition as in Figure 4.15. Unless noted, PEG inert flows were PEG 200 (Sigma Aldrich) containing the same PI concentration as the accompanying monomer solution. In experiments to find the critical gel point of PEG-DA 575, the monomer solutions were comprised of 5% (v/v) PI, 1% (v/v) methacryloxyethyl thiocarbamoyl rhodamine B (Polysciences) in PEG 200 (1mg/ml), 4% (v/v) Food coloring (Tone Brothers Inc.), X% (v/v) PEG-DA 575, and 90-X% (v/v) PEG 200. PUA and TMPTA (Polysciences) particles were prepared from a prepolymer composition of 55% (v/v) monomer, 35% (v/v) toluene and 10% (v/v) PI. The liquid PUA precursor (MINS 311RM) was kindly provided by Minuta Tech. For QDs stock solution, we purchased 915 nm CdTeSe/ZnS QDs

dispersed in toluene at a concentration of 25 mg/ml (Nano Optical Materials Inc.). QDs monomer mixture consisted of 10 % (v/v) PI, 40% (v/v) NOA81 (Norland Products), and 50% QDs solution. The QDs concentration was adjusted by toluene dilution of stock solution.

iCVD Process

All iCVD films were deposited in a custom built vacuum reactor (Sharon Vacuum) with a radius of 12 cm, as previously described [114]. The ChromAlloy filaments (Goodfellow) were mounted in a parallel array to provide the thermal excitation, heated by a DC power supply (Sorensen). The filament temperature was measured by a K type thermocouple (Omega Engineering) attached to one of the filaments. The vertical distance between the filament and the deposition stage was 1.5 cm. The stage was back-cooled by a recirculating chiller/heater (NESLAB), which served as the purpose of maintaining the substrate temperature constant to prevent the heating of the sample due to the heated filaments. All the chemicals species were used as purchased without further purification. tert-Butyl peroxide (Aldrich, 97%) initiator at room temperature, was fed into the reactor through a mass flow controller (model 1479, MKS Instruments) at 1 sccm. iCVD deposition conditions utilizing the monomer 4-aminostyrene (4-AS) (Aldrich, 97%) and glycidyl methacrylate (Aldrich, 97%) (GMA) were adopted from previous work reported by Xu and Mao [115, 116]. Total pressure in the vacuum chamber was maintained at 0.3 torr and 0.2 torr for 4-AS and GMA depositions respectively.

SFL Setup

The setup for SFL uses pressure provided by a compressed-air source to drive flow inside the microfluidic channels. The compressed-air flow control system is described in our previous work [74]. Devices were mounted on an inverted microscope (Axiovert 200, Zeiss) equipped with a VS25 shutter system (UniBlitz) to precisely control the UV exposure dose. A photomask was then inserted into the field-stop of the microscope. The masks were designed in AUTOCAD 2005 and printed using a high-resolution printer at CAD Art Services (Bandon, OR). A Lumen 200 (Prior) served as the source of UV light. A filter set that allowed wide UV excitation (11000v2: UV, Chroma) was used to select light of the desired wavelength. The VS25 shutter system driven by a computer-controlled VMM-D1 shutter driver provided specified pulses of UV light. The shutter-mediated UV exposures were synchronized with the stop flow system using Python to allow the user to cycle SFL process automatically through the specification of a flow duration, a stoppage duration, and an exposure time. Typical exposure times used were 30–300 ms and pressures ranged from 0.05 to 15 psi.

Near Infrared Fluorescence Imaging Analysis

Near infrared fluorescence images of particles were taken using a fluorescence microscope (Carl Zeiss, Axiovert 200), with a CCD camera (Carl Zeiss, ZxioCam MRm) and 2D InGaAs array (Princeton Instruments OMA 2D). Samples were excited by a 658 nm laser (LDM-

OPT-A6-13, Newport Corp) at 35 mW and the emission from 900 to 1400 nm was detected for 1 s using a 20x objective.

4.3 Non-PDMS Based Device Fabrication

Oxygen-free FL is a technique designed to extend current PDMS-based FL to non-PDMS based devices. These non-PDMS based devices include homogeneous and heterogeneous devices created from numerous combinations of alternative substrate materials as well as integrated devices to mount electric and magnetic circuits. In past work, the absence of a suitably general bonding method to combine diverse types of substrates has led to limitations in device construction. In developing oxygen-free FL, we required a bonding method that (1) does not depend on substrate type for the creation of a wide array of devices with different properties, (2) does not demand immediate bonding for further device integration, and (3) offers strong mechanical resistance for high-throughput synthesis. With these considerations in mind, we use the nano-adhesive iCVD bonding technique for the creation of non-PDMS based devices. The versatile iCVD method is able to deposit conformal and pinhole-free adhesive films on virtually any kind of substrate with nanometer-level thickness control [115, 117, 118]. Also, the iCVD bonding process is independent of the channel fabrication process, and deposited samples can be stored for more than 2 months prior to bonding [115, 118]. Finally, bonded devices were able to withstand pressures higher than 150 psia, and the all-iCVD nano-adhesive bonding process displayed superior resistance against hydrolytic degradation [115].

4.3.1 Homogeneous NOA81 Channel Fabrication

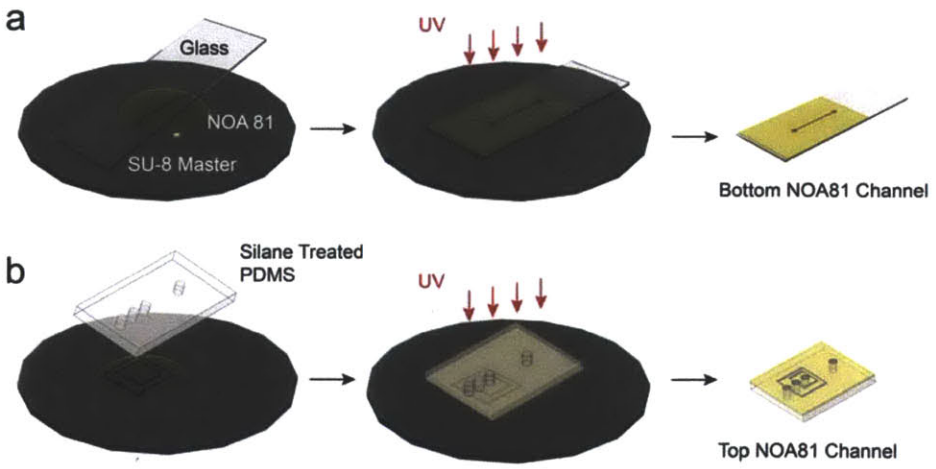

Figure 4.1: *NOA81 channel fabrication (A) Bottom layer of channel is created by sandwiching NOA between glass substrate and SU-8 master mold bearing positive-relief features and then curing with 10-min UV exposure. (B) Top layer is created in a similar fashion, using a different master mold and a silane-treated PDMS layer with inlet and outlet holes that align with the corresponding SU-8 relief elements. Silane treatment of PDMS substrate facilitates bonding between PDMS and NOA.*

We demonstrate that the iCVD nano-adhesive bonding technique can be used to fabricate non-PDMS based channels. UV-curable Norland Optical Adhesive 81 (NOA81), a thiolene-based resin, was chosen as the substrate material because it is commercially available and allows for rapid prototyping and reliable replication of sub-micron features [119]. In addition, this material can provide a number of attractive optical and physical properties including transparency, high elastic modulus (~ 3 Gpa), and excellent solvent resistance [119]. The channel substrates are prepared using the process described in Figure 4.1. Briefly, a droplet of NOA81 was put on a silicon wafer and sandwiched between the wafer and a glass slide. After curing under the UV (365nm) lamp for 10 min and unmolding, a bottom NOA81 channel was mounted on the glass slide. A blank PDMS slab with inlets and an outlet was treated with oxygen plasma for 30 s and then with tricholorvinylsilane (Aldrich, 98%) under vacuum for 5 min. Again, the NOA81 was exposed to UV for 10 min giving a top NOA channel on the PDMS substrate.

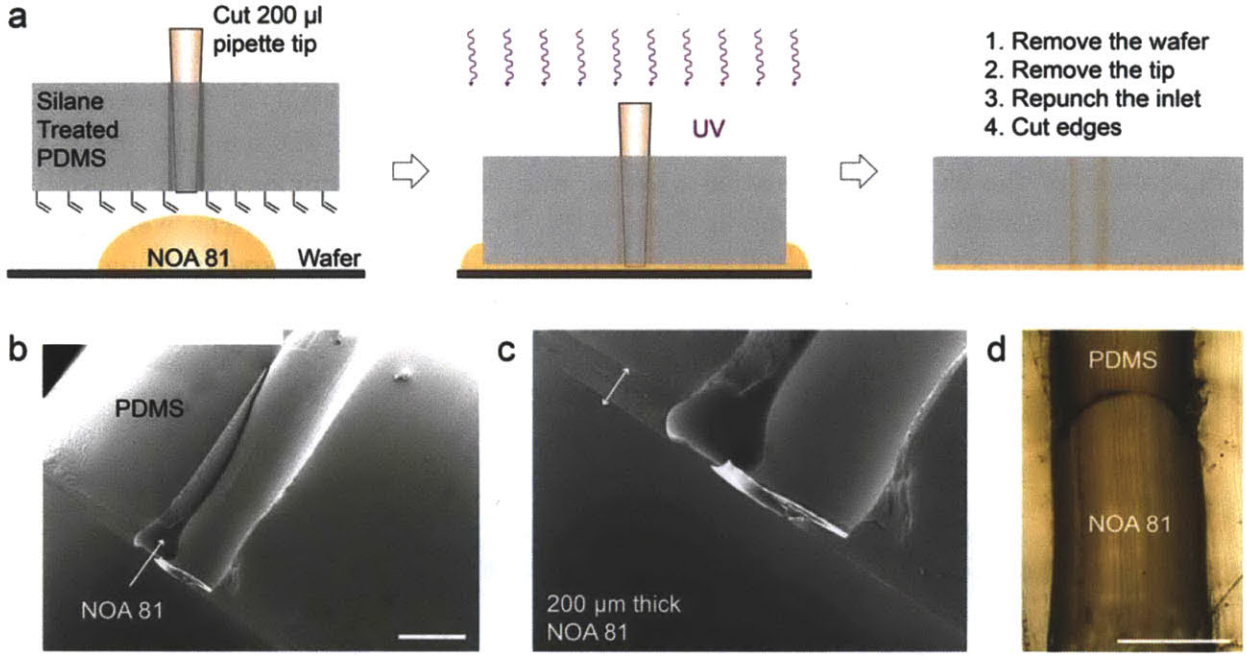

Figure 4.2: *Inlet fabrication utilizing NOA81 capillary coating. (a) A schematic description of the inlet fabrication process. (b) A SEM (Scanning Electron Microscope) image for intersection of an NOA81-coated PDMS inlet. During the sample cutting process, the hard NOA81 coating that originally covered the entire circumference of the inlet was broken, and the image provided shows only a portion of the original cylindrical coating. The white arrow indicates the remaining portion of the broken NOA81 coating. (c) A magnified SEM image of (b). (d) An optical image to show the intersection of an evenly coated inlet. The NOA81 was coated with around 200 µm thick on the PDMS substrate. All scale bars are 1 mm.*

In PDMS device fabrication, inlet fabrication has not drawn attention as the material can allow for easy inlet fabrication. PDMS can provide quick punching of inlets and tight

supporting of tubing. However, this situation completely turns about in plastic or glass channel fabrication. These channels sometimes require special equipment for inlet punching and supporters to hold tubing [119]. Usually, such supporters are glued on the inlets, occupying considerable areas that can be a problem in fabricating dense inlets. For our case, we developed an inlet fabrication method accommodating the PDMS advantages. The inlets had NOA81 coating on PDMS inlets (Fig. 4.2).

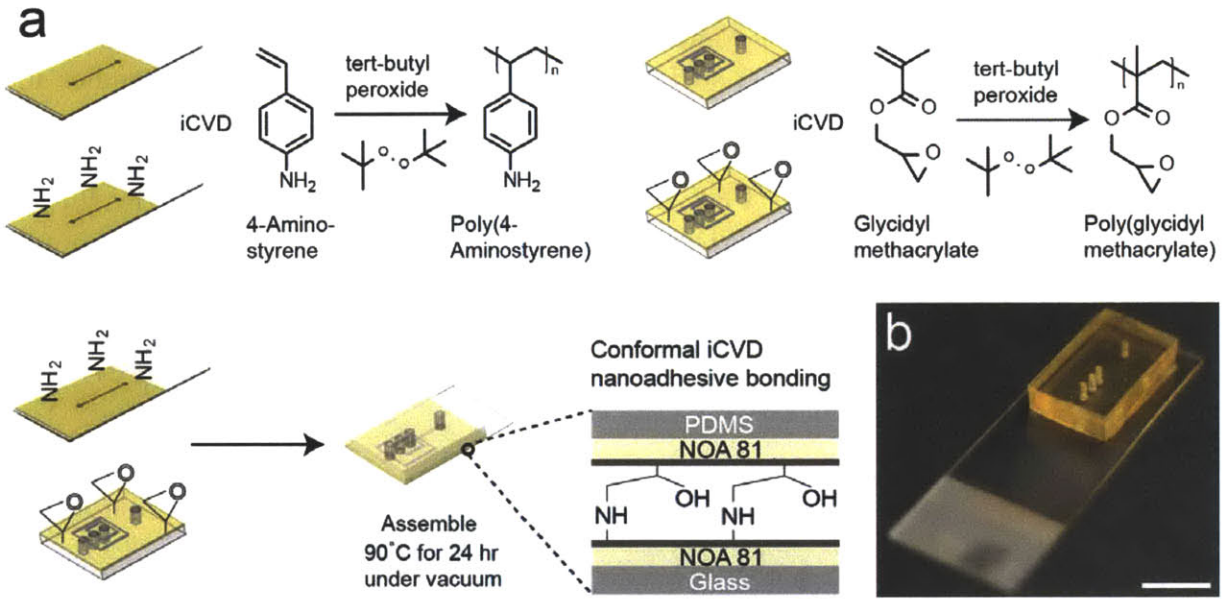

Figure 4.3: *iCVD nano-adhesive bonding (a) Schematic description for the iCVD nano-adhesive bonding process. The nano-adhesive films of poly(4-aminostyrene) (PAS) and poly(glycidyl methacrylate) (PGMA) were deposited on top and bottom channel substrates, respectively, via iCVD. The two channel substrates are aligned and sealed together under vacuum via the ring-opening reaction of the newly generated amine and epoxy groups. (b) Color image of fully assembled channel mounted on a glass slide. The devices are optically transparent and can be used with photolithographic techniques. Scale bar is 1 mm.*

A nano-adhesive bonding process utilizing iCVD has been developed previously [115, 118]. However, in the past construction of such devices, one substrate was required to be a soft elastic PDMS substrate in order to ensure conformal contact to the other substrate [115, 118]. When hard channel substrates were combined together, air bubbles were entrapped between channel interfaces, causing insufficient channel sealing and even distortion of channel geometries. To overcome this, we developed a vacuum curing process to remove the trapped air bubbles and, for the first time, generated homogeneous NOA81 channels using the bonding technique (Fig. 4.3). It should be noted that the NOA81 channels can also be prepared by existing thiolene-based bonding techniques [119-121]. However, these existing methods do not satisfy all of the previously mentioned requirements for oxygen-free FL, thereby limiting operational flexibility.

4.3.2 Heterogeneous NOA81 Channel Fabrication

We also demonstrate that the iCVD bonding process can be used to fabricate heterogeneous NOA81 channels. To do this, we prepared top NOA 81 channels by the process described in (b) of Figure 4.1. In this process, we used an additional layer of PDMS to add thickness for easier inlet fabrication. This elastic PDMS layer was easily modified for inlet creation because holes could easily be punched into it using luer stubs, and the resulting elastomer holes enabled tight fitting of pipettes containing monomer. As a result of this construction process, the top substrate was a composite slab of PDMS and NOA81. However, it is important to note that the channel surfaces in contact with the synthesis chamber itself were comprised only of NOA81, and did not contain PDMS. Using the iCVD bonding process, we successfully combined the hard NOA81 channel surfaces with a number of substrates including Si wafers, PET and polycarbonate (Fig. 4.4). This is the first demonstration that heterogeneous NOA81 channels can be created by the iCVD bonding process. The results can further validate that the nano-adhesive bonding method can be used to combine non-PDMS surfaces during the fabrication of various types of non-PDMS based devices.

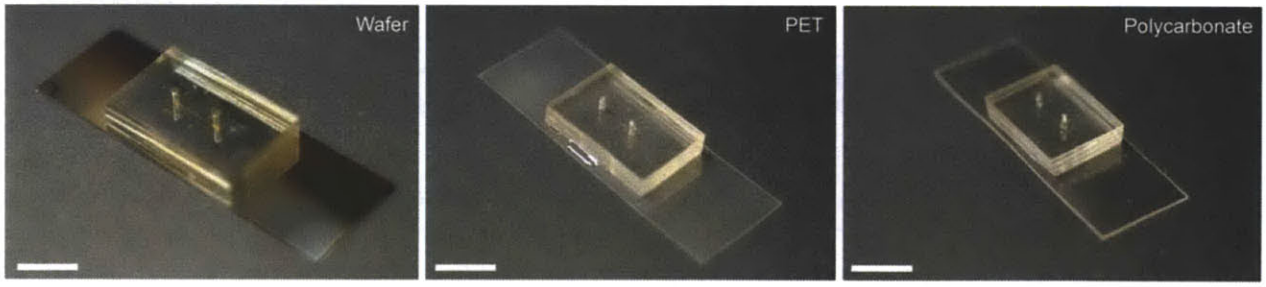

Figure 4.4: *Bonding NOA81 channels with various substrates. All scale bars are 1 cm.*

4.3.3 Evaluation of NOA-based Microchannel Performance

The nano-adhesive bonding process was able to combine channel substrates, as well as retain a range of substrate properties. The NOA devices bonded with the nano-adhesive were optically transparent (Fig. 4.3b), compatible with standard photolithography techniques, and displayed response time characteristics far superior to those of PDMS channels [115, 119]. The high Young's modulus of the NOA81 channels [119] produces a response time scale that is 1000 times smaller than that which can be achieved with PDMS devices, thereby greatly decreasing the lag times associated with pulsed flow.

$$\frac{\tau_{r,NOA81}}{\tau_{r,PDMS}} \sim \frac{E_{PDMS}}{E_{NOA81}} = \frac{1\ MPa}{10^3\ MPa}$$

Also, the devices exhibited excellent compatibility with organic solvent flows, with little evidence of swelling or deformation in numerous trials (Fig. 4.5a). To demonstrate the improvement over previous iCVD nano-adhesive work [115, 118], we first fabricated a two-layer hybrid channel (PDMS top, NOA81 bottom) and injected toluene at the inlet of the bottom channel. When the toluene reached the PDMS substrate, the PDMS channels began to shrink dramatically, and within 1 min, the width of the top PDMS channel was reduced by ~ 60%. The reduction of channel size can significantly alter flow rates and velocity profiles, and thus prevent the creation of stable layered flows. We then performed the same experiments with homogeneous NOA81 channels and examined their performance with organic solvent flows. Unlike the hybrid channels, we observed no significant swelling, even after 5 hr of solvent exposure. This is the first demonstration that the devices bonded by the nano-adhesive technique have solvent resistance.

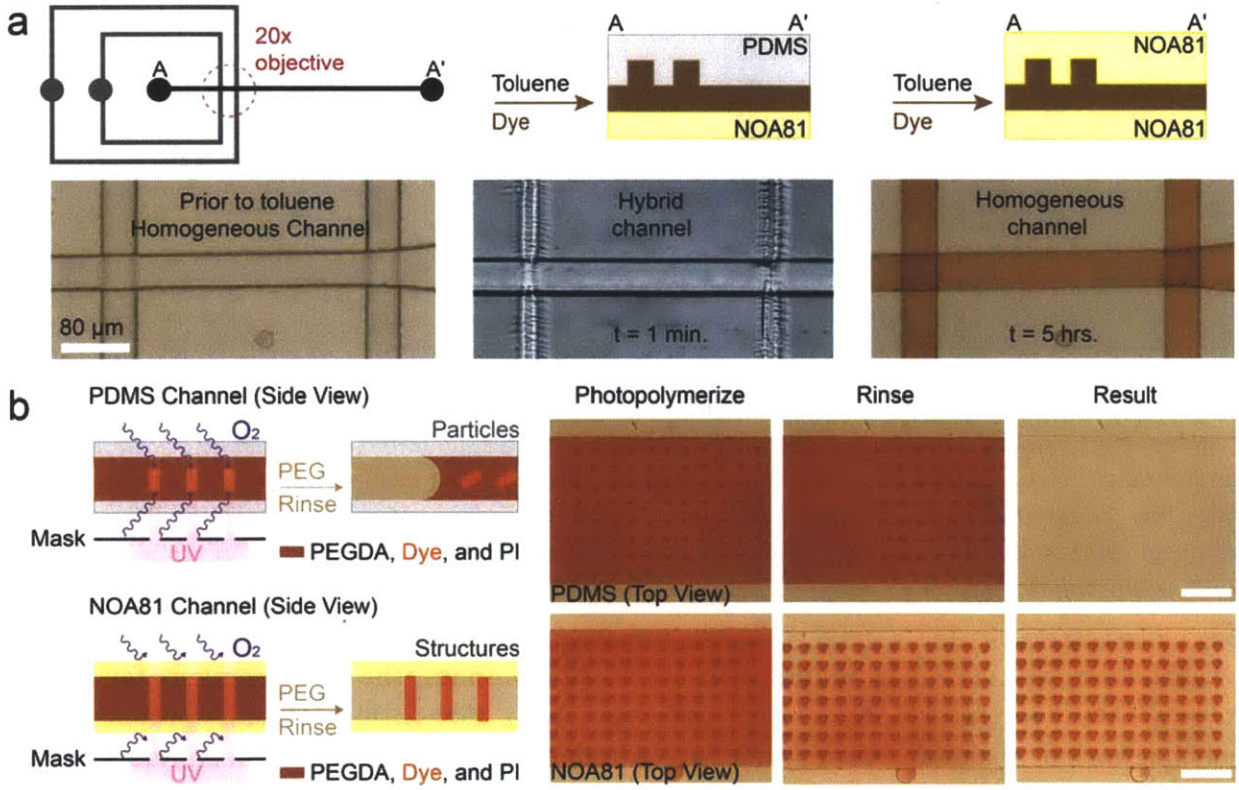

Figure 4.5: *iCVD nano-adhesive bonding (a) Schematic description for the iCVD nano-adhesive bonding process. The nano-adhesive films of poly(4-aminostyrene) (PAS) and poly(glycidyl methacrylate) (PGMA) were deposited on top and bottom channel substrates, respectively, via iCVD. The two channel substrates are aligned and sealed together under vacuum via the ring-opening reaction of the newly generated amine and epoxy groups. (b) Color image of fully assembled channel mounted on a glass slide. The devices are optically transparent and can be used with photolithographic techniques. Scale bar is 1 mm.*

Lastly, as NOA81 substrates are gas-impermeable, the devices cannot provide oxygen lubrication layers for the creation of free-floating particles. As mentioned earlier, oxygen lubrication in gas-permeable PDMS channels allows for the creation of free-floating particles that can be flushed out by rinsing solution and collected in a reservoir. However, in gas-impermeable NOA81 channels, the radical polymerization was able to propagate to the channel walls in the absence of oxygen and thereby generated photo-patterned structures that were affixed to the channel and could not be removed by flow (Fig. 4.5b).

4.4 On-the-fly Particle Synthesis

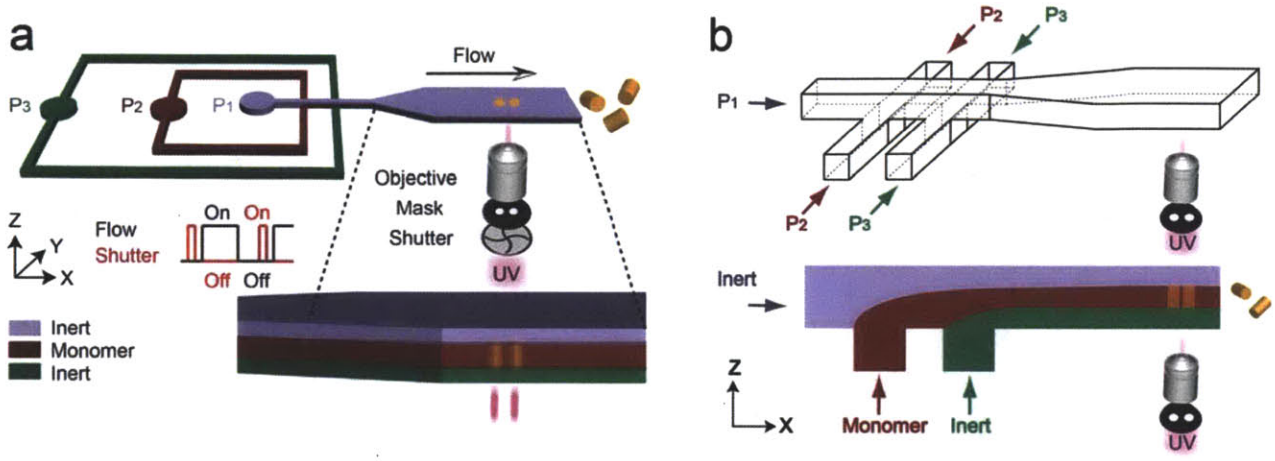

Figure 4.6: *On-the-fly alteration of particle height with inert flows (a) Schematic of microparticle synthesis in gas-impermeable NOA channel. Particles were synthesized and then carried out of the synthesis area using rapid, synchronized cycles of shutter-mediated UV exposure and pressure-driven flow. (b) A schematic to describe the vertical flow focusing process. Instead of volumetric flow rates, we controlled pressures at the inputs to provide rapid alternation between the flow and stoppage states. The middle monomer flow is sandwiched between top and bottom inert flows without mixing due to low Reynolds number flow conditions.*

Oxygen-free FL is a technique developed to eliminate the requirement for oxygen lubrication in the FL process by utilizing inert flows that cannot propagate the polymerization reaction. Combining a hydrodynamic flow focusing technique with a compressed-air flow control system [73, 74], we generated pulsed tri-layered flows containing two bounding inert flows and a central monomer flow (Fig. 4.6). Although vertical flow focusing techniques have been used in flow cytometry [110, 111], this is the first demonstration of particle synthesis with stacked lubrication layers. Moreover, it is important to note that our synthesis with the stacked lubrication layers was achieved with a pulsed flow regime that periodically stopped the flow just prior to the photopolymerization step to provide higher feature resolution and improved throughput [73]. As pressure-driven sources typically provide quick dynamic response [74, 122], we generated rapid pulsing of the layered microflows using our pressure-control system that can allow for fast and simple modulation [74]. We rapidly polymerized cylindrical particles

in the middle monomer layer by terminating the driving pressure, waiting 300 ms to ensure complete flow stoppage, and then exposing the flow to a 75 ms UV burst. We then re-initiated pressure-driven flow for 1 s to flush particles out to the reservoir (Fig. 4.6a). This process was cycled and automated using a computer-controlled system. There were three main criteria for the inert flows: (1) miscibility with the middle monomer to avoid interfacial tension, (2) similar density with the middle monomer to prevent gravity-induced reorientation of interfaces [123], and (3) a concentration of photoinitiator (PI) that matched the concentration contained in the middle monomer to ensure homogenous polymerization. To satisfy these conditions, we used polyethylene glycol (PEG) with PI for the inert flows for synthesis trials with a central monomer of polyethylene glycol diacrylate (PEG-DA).

4.4.1 Maximum Particle Synthesis Throughput of Oxygen-free FL

Oxygen-free FL can provide a higher particle synthesis throughput than former FL techniques, improving the throughput of SFL. The SFL process requires a stop time for the channel relaxation of the elastic PDMS devices. This time ranges from tens of milliseconds to one minute depending on the channel height, width, and length [73]. The technique also need an induction time to deplete oxygen dissolved in the monomer flows [75, 124]. In our current setup, the minimum induction time for 40 μm channel approximately occupies 20% of the polymerization time. In addition, the PDMS devices have shown low pressure resistance. Oxygen-free FL in NOA81 channels can use 1000 times smaller stop times than SFL, and these oxygen impermeable devices can provide negligible induction time in the ideal case in which oxygen dissolved in the monomer is completely depleted before injection. The channels in oxygen-free FL can also utilize higher flow velocities, with operating pressures over 150 psi. When we synthesized particles with 3 μm feature size in a 1 mm wide, 40 μm high, and 1 cm long channel, the maximum particle synthesis throughput for CFL and SFL were respectively estimated in Reference 73. Estimating the maximum particle synthesis throughput of oxygen-free FL for the synthesis condition, we prepared Table 4.1 to summarize the maximum particle synthesis throughput for each type of FL.

Process	Stop	Polymerization	Flow	Cycle Time	Throughput (Particles/min)
CFL [Ref. 73]	0	~ 50 ms	~ 20 s	~ 20 s	$10^4 \sim 10^5$
SFL [Ref. 73]	~ 20 ms	~ 50 ms	~ 110 ms	~ 180 ms	$\sim 10^7$
Oxygen-Free FL	< 1 ms	~ 40 ms	~ 35 ms	< 76 ms	$\sim 2.3\times10^7$

Table 4.1 *Summary for the maximum particle synthesis throughput for each type of FL*

4.4.2 Modified Hydrodynamic Resistance Model

We developed a predictive model for the creation of particles with inert flows that allowed us to adjust particle height in a systematic fashion. In this approach, the volumetric flow rates for the top and bottom inert flows were designed to be equal to give symmetrical inert

thickness in the synthesis chamber. To estimate volumetric flow rates from the measured inlet driving pressures, we previously developed a model that calculated hydrodynamic resistances from channel geometries and fluid viscosities [125].

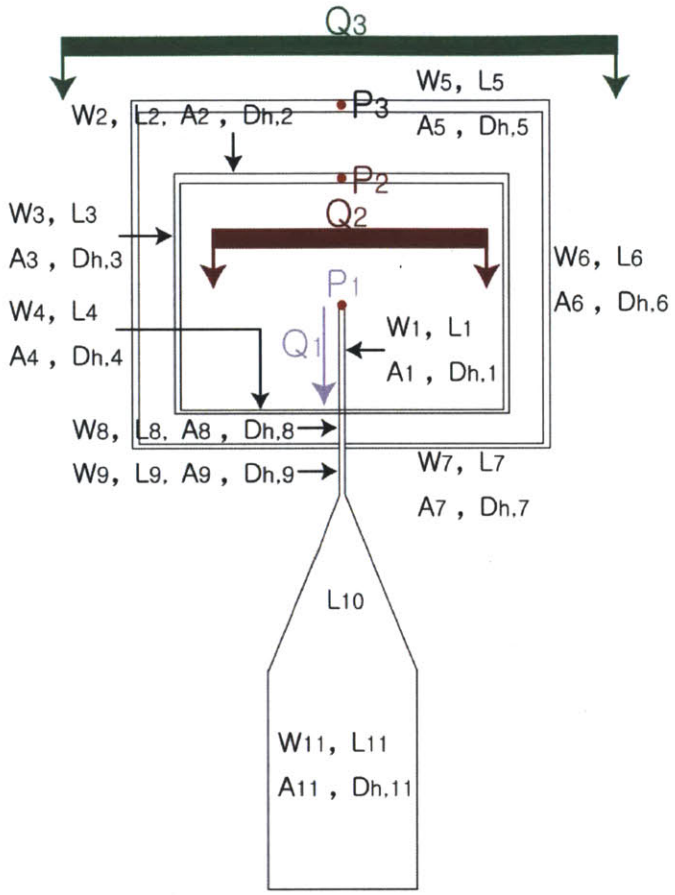

Figure 4.7: *A schematic description for two layered homogeneous NOA81 channels*

Width	μm	Area	μm²	Hydraulic diameter	μm	Length	μm
W_1	200	A_1	8000	$D_{h,1}$	67	L_1	4873
W_2	100	A_2	4000	$D_{h,2}$	57	L_2	7780
W_3	40	A_3	1600	$D_{h,3}$	40	L_3	4873
W_4	200	A_4	8000	$D_{h,4}$	67	L_4	3773
W_5	100	A_5	4000	$D_{h,5}$	57	L_5	5430
W_6	40	A_6	1600	$D_{h,6}$	40	L_6	3773
W_7	40	A_7	1600	$D_{h,7}$	40	L_7	3217
W_8	40	A_8	1600	$D_{h,8}$	40	L_8	400
W_9	40	A_9	1600	$D_{h,9}$	40	L_9	120
						L_{10}	2000
W_{11}	500	A_{11}	20000	$D_{h,11}$	74	L_{11}	3875

Table 4.2 *Geometries of a two layered homogeneous NOA81 channel*

However, this model neglected resistances that arose from inlets, corners, defects, and misalignments. To address this, we created a modified model that experimentally determined total hydrodynamic resistances by lumping previously neglected factors (Fig. 4.8).

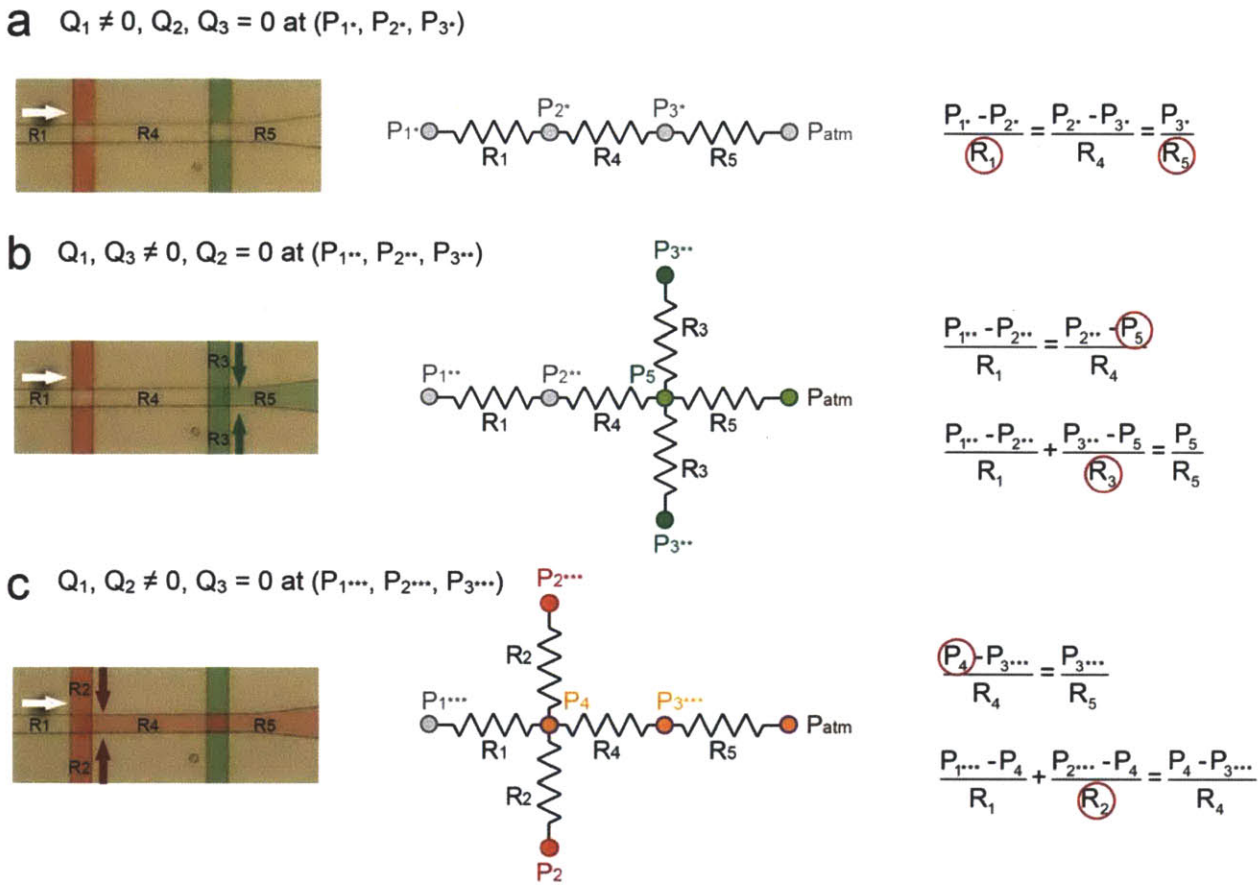

Figure 4.8: *On-the-fly alteration of particle height with inert flows (a) Schematic of microparticle synthesis in gas-impermeable NOA channel. Particles were synthesized and then carried out of the synthesis area using rapid, synchronized cycles of shutter-mediated UV exposure and pressure-driven flow. (b) A schematic to describe the vertical flow focusing process. Instead of volumetric flow rates, we controlled pressures at the inputs to provide rapid alternation between the flow and stoppage states. The middle monomer flow is sandwiched between top and bottom inert flows without mixing due to low Reynolds number flow conditions.*

In this approach, we control inlet pressures to generate the three meta-stable hydrodynamic states shown in Figure 4.8. In the first step, we set up all inlet pressures to a fixed value. 2.0 Psia. Then, we independently reduce P_2 and P_3 to satisfy each case. For the first case, we reduce both P_2 and P_3 to meet the moment at which flow colors are optically clear on intersections. As we use food coloring to distinguish flows, the moment stands for that volumetric flow rates, Q_2 and Q_3 are zero while Q_1 is non-zero. As shown in Figure 4.8a, Q_1 has no color while Q_2 and Q_3 colors are red and green, respectively. In this meta-stable

status, we can create a resistance diagram and successively set up two equations by mass conservation. The diagram and equations can be found next to the optical images in Figure 4.8. For the other two cases (Fig. 4.8b and c), we can do the same process and eventually write 6 equations with known 9 inlet pressures and R_4. Note that R_4 can be just estimated from channel geometry as the resistance is not combined with inlets and corners. As the 6 equations have 6 unknown variables, we can determine all hydrodynamic resistances. Table 4.3 ~ 4.6 summarize specific inlet pressures satisfying each case and hydrodynamic resistance values extracted from the pressures.

1) $Q_1 \neq 0$, Q_2, $Q_3 = 0$

P_{1*} (Psi)	P_{2*} (Psi)	P_{3*} (Psi)	R_1 (μm^{-3})	R_5 (μm^{-3})
2.0	0.8	0.6	0.027	0.014

Table 4.3 *Estimation of hydrodynamic resistances, R_1 and R_5*

2) Q_1, $Q_3 \neq 0$, $Q_2 = 0$

P_{1**} (Psi)	P_{2**} (Psi)	P_{3**} (Psi)	R_3 (μm^{-3})
2.0	1.0	2.0	0.048

Table 4.4 *Estimation of hydrodynamic resistances, R_3*

3) Q_1, $Q_2 \neq 0$, $Q_3 = 0$

P_{1***} (Psi)	P_{2***} (Psi)	P_{3***} (Psi)	R_2 (μm^{-3})
2.0	2.0	0.8	0.038

Table 4.5 *Estimation of hydrodynamic resistances, R_2*

We also calculated the resistance values of R_1, R_2, R_3, R_4, and R_5 from the previous model considering only channel geometries [125]. Then, we compare the values with the experimentally measured hydrodynamic resistances. This comparison shows considerable differences between two models. For example, unlike the previous model, R_2 and R_3 have larger values than R_1. Also, R_5 is under-estimated in the previous model.

Model	R_1 (μm^{-3})	R_2 (μm^{-3})	R_3 (μm^{-3})	R_4 (μm^{-3})	R_5 (μm^{-3})
Previous	0.036	0.022	0.032	0.0045	0.0035
Modified	0.027	0.038	0.048	0.0045	0.014

Table 4.6 *Comparison of hydrodynamic resistances estimated from two suggested models*

4.4.3 Symmetry Condition for Inert Flows ($Q_1 = Q_3$)

We demonstrate that the modified model is superior to the previous one in estimating hydrodynamic resistances and predicting inlet pressures to satisfy symmetry condition ($Q_1 = Q_3$) for inert flows. Using hydrodynamic resistances estimated from two models, we can express intersection pressure P_4 and P_5 in terms of inlet pressures P_1, P_2 and P_3. When we use a typical pressure 3 psi for P_2, P_3 should have linear relations with P_1 to achieve the symmetry condition.

1) Previous Model

$$\begin{bmatrix} P_4 \\ P_5 \end{bmatrix} = \begin{bmatrix} 0.14 & 0.22 & 0.063 \\ 0.06 & 0.091 & 0.084 \end{bmatrix} \begin{bmatrix} P_1 \\ P_2 \\ P_3 \end{bmatrix}, \qquad P_3 = 0.84P_1 - 1.07 \text{ (for symmetry condition, } P_2 = 3.0 \text{ Psi)} \qquad (4.1)$$

2) Modified Model

$$\begin{bmatrix} P_4 \\ P_5 \end{bmatrix} = \begin{bmatrix} 0.28 & 0.20 & 0.11 \\ 0.20 & 0.14 & 0.15 \end{bmatrix} \begin{bmatrix} P_1 \\ P_2 \\ P_3 \end{bmatrix}, \qquad P_3 = 1.4P_1 - 0.61 \text{ (for symmetry condition, } P_2 = 3.0 \text{ Psi)} \qquad (4.2)$$

The linear relations between P_3 and P_1 have differences in slopes and intercepts depending on applied model (Fig. 4.9). When P_1 is getting high, the difference between the two models to predict values for P_3 will significantly increase. If we use 150 psi (which is the maximum pressure that bonds can withstand) as P_1, the gap ΔP_3 reaches to 85 psi.

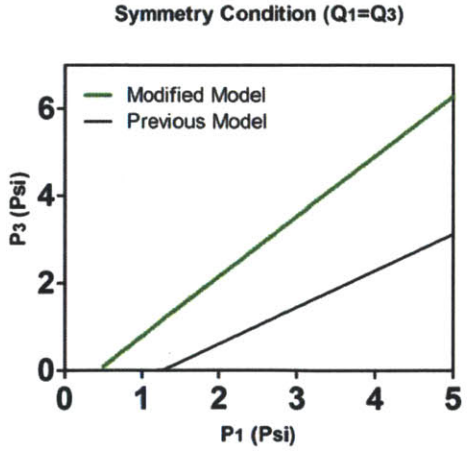

Figure 4.9: *The inlet pressure relation to achieve symmetry condition ($Q_1 = Q_3$). When we use a typical pressure 3.0 Psi as P_2, P_3 and P_1 have a linear relation with slopes and intercepts depending on which model is applied.*

Experimental results validated that the modified model could provide accurate prediction for inlet pressures to generate symmetrical inert flows. To visualize the symmetrical inert layers, we performed an experiment to synthesize three-layered particles in a PDMS channel (Fig. 4.10a). The middle layer has 0.01 wt% of rhodamine dye to distinguish top and bottom inert layers. For all layers, we used PEGDA 575 95% (v/v) and PI 5% (v/v). Fixing P_2 = 3.0 Psi, we selected a specific P_1 (= 4.9 Psi) pressure and used P_3 predicted from each model to generate symmetrical particles. After particle synthesis, we successfully prepared particles containing symmetrical top and bottom layers when we used inlet pressures predicted from the modified model (Fig. 4.10b).

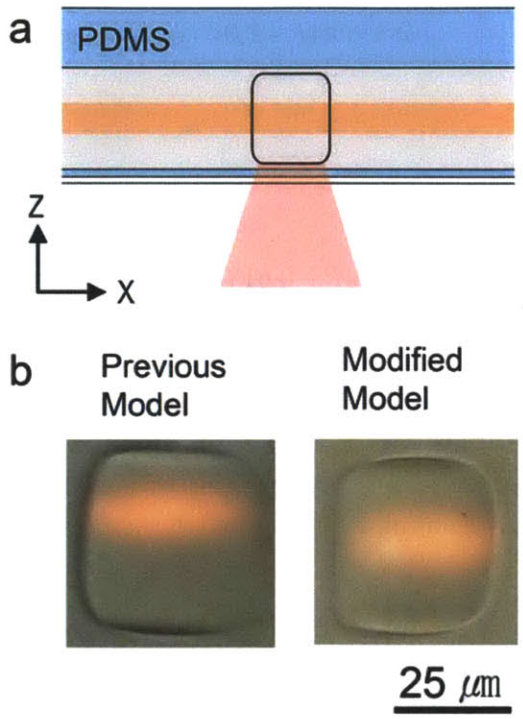

Figure 4.10: *Comparing modified hydrodynamic model with the previous model in achieving the symmetry condition. (a) A schematic description for preparing tri-layered particles containing red dye in the middle layer. The dye was used to visualize symmetry of layers. (b) Optical images of synthesized particles using inlet pressures predicted by each model. The modified model gives more accurate prediction for inlet pressures to achieve the symmetry condition.*

4.4.4 Middle Layer Thickness, H_m

We have used pressure control system to provide quick stoppage of flows on the order of milli-seconds. As a result, we have estimated volumetric flow rates from inlet pressures using the modified hydrodynamic resistance model. To predict the middle layer thickness (H_m), we need not only volumetric flow rates but also information for velocity profile of the flows. We assume the layered flows can have velocity profile of Poiseuille flow as our

channel geometry (channel aspect ratio < 0.1) is slit-like. The channel aspect ratio is defined to the ratio of the channel height divided by the channel width. This will be a valid assumption as previous work even shows that channel geometry with aspect ratio ~ 1 can almost produce velocity profile of Poiseuille flow [126].

$$v(z) = v_{\max}\left(1-\left(\frac{z}{h_c}\right)^2\right) \tag{4.3}$$

Where v is the velocity of flow and h_c is the half of the channel height. We also used following 3 assumptions: (i) Newtonian, incompressible, fully developed and laminar flows, (ii) negligible surface tension between solutions, and (iii) viscosity μ is the same in all inlet flow streams.

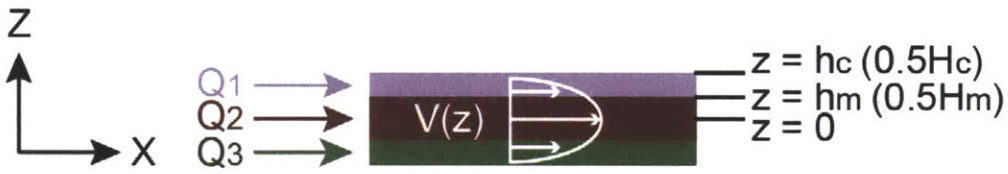

Figure 4.11: *A schematic diagram for flow profile in the channel*

We define the ratio of the volumetric flow rates of inert flow (Q_1) divided by the volumetric flow rates of middle monomer flow (Q_2) as B. Then, B can be expressed in terms of inlet pressures using the modified hydrodynamic model.

$$B = \frac{Q_1}{Q_2} = \frac{R_2(P_1 - P_3)}{R_1(P_2 - P_3)} \tag{4.4}$$

When we use the symmetry condition, B values are just function of P_1 (Fig. 4.12).

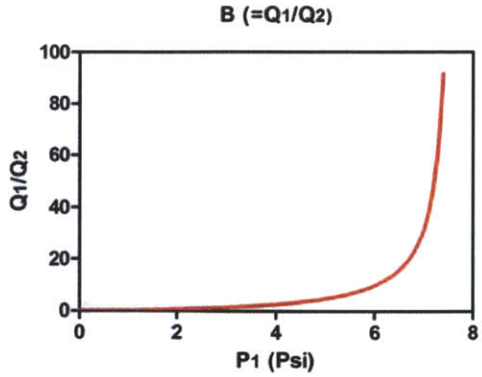

Figure 4.12: *A plot for B versus P_1. B is the ratio of the volumetric flow rates of inert flow (Q_1) divided by the volumetric flow rates of middle monomer flow (Q_2). In this plot, P_2 is fixed to 3.0 Psi while P_3 is the linear relation with P_1 to satisfy the symmetry condition.*

We use B values as the values are directly related to the middle layer thickness (H_m). To mathematically relate B values with H_m, we set up the mass balance equation.

$$B = \frac{Q_1}{Q_2} = \frac{\int_{h_m}^{h_c} \rho v \, dz}{\int_0^{h_m} \rho v \, dz} \tag{4.5}$$

Where ρ is the density of flow, and h_m is the half of the middle flow layer thickness (H_m). Putting equation (4.3) into equation (4.5), we can get the following depressed cubic equation that does not contain square term of h_m.

$$h_m^3 - 3h_c^2 h_m + \frac{2h_c^3}{(B+1)} = 0 \tag{4.6}$$

Solving this equation (4.6), we can get the final analytical expression of H_m.

$$H_m = 2h_c \cos\left(\frac{1}{3}\arccos\left(-\frac{1}{B+1}\right) - \frac{2\pi}{3}\right) \tag{4.7}$$

4.4.5 On-the-fly Alteration of Particle Heights

The particle heights (H_p) could be taken to be the same as the middle layer thickness (H_m) because we synthesize particles with sub-second monomer residence time. Estimating the flow time to the synthesis zone to be < 200 ms, the overall monomer residence time (flow time + stop time + polymerization time) was ~ 500 ms, which was much smaller than the characteristic time to diffuse the channel height ($h_c^2/D_{PEGDA575}$ ~ 80 s, see Fig. 4.15). As a result, we do not need to consider the additional thickness contributed by monomer diffusion in the height dimension. As shown in the graph of Figure 4.13, the H_m prediction compared well with measurements of particle heights.

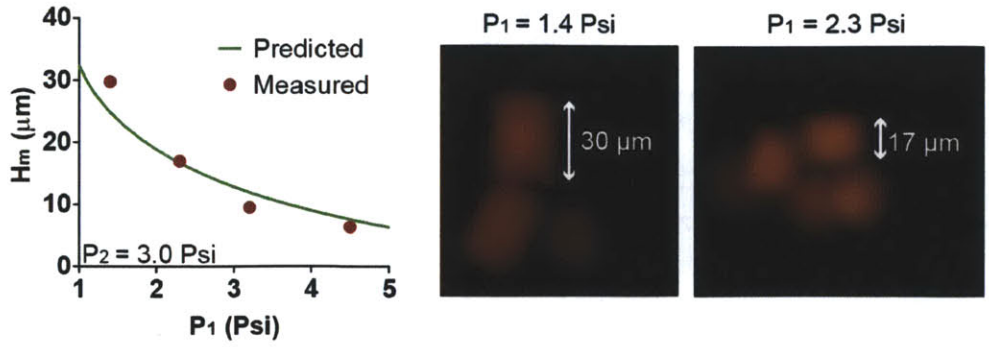

Figure 4.13: *Particle height as a function of P1. Height of cylindrical particles was seen to vary with inlet pressures in a manner that matched predictions from the hydrodynamic resistance model. As shown in the graph, the H_m prediction compared well with measurements of particle heights.*

Through the precise control of inlet pressures, oxygen-free FL can be used to easily and rapidly vary particle height in a channel with a fixed height. Current FL can synthesize only one particle height from one device as the oxygen inhibition layer thickness is fixed to ~ 2 μm, and thus new PDMS devices must be prepared for each different particle height that is desired. This requires the labor- and time-intensive fabrication of new master wafers. It is important to note that for such PDMS devices, our inert-flow approach can still be applied to generate particles with various heights. In Figure 4.14, we demonstrate the adjustment of particle height in a PDMS device. In a same way with NOA 81 devices, we used PEGDA 575 as monomer flow and inert PEG 200 as a tuning fluid in the top and bottom streams of a three-layer flow (Fig. 4.14a). The thickness of the tuning layers was adjusted by varying the inlet pressures of the streams. In a 40 μm high PDMS device, we produced triangular particles with reduced heights (Fig. 4.14b and c). For our channel, a B (Q_1/ Q_2) = 0.45 resulted in particles with a height of ~ 19 μm which was around 50 % of the height of particles generated without tuning fluids (Fig. 4.14d). The particle height predicted by the above equation (4.7) was 20 μm.

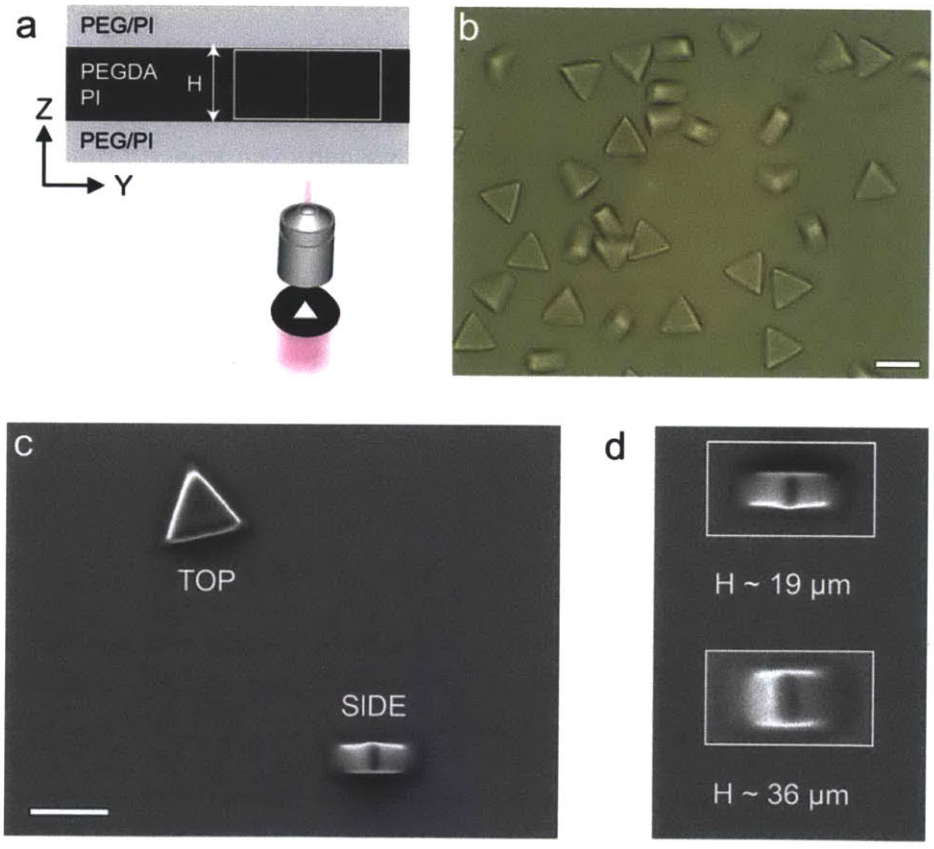

Figure 4.14: *On-the-fly alteration of particle heights in a PDMS device. (A) A schematic description for the process adjusting particle heights with inert tuning fluids (B) An optical image of collected particles in a reservoir. (C) A SEM image showing top and side of particles. (D) Comparison with the heights of original particles that were synthesized with oxygen lubrication layers (~2 μm). The top particle has altered height of 19 μm while the bottom one has almost channel height of 36 μm.*

In the oxygen-free FL setup, there is a minimum residence time of ~ 0.1 s, which can result in monomer diffusion into inert flows. Considering this time, the minimum particle height in oxygen-free FL can be estimated to be around 2 μm by the following calculation: For very thin middle layer, we can assume point source in 1D diffusion [127],

$$C(z,t) = \frac{m_0 e^{-z^2/(4Dt)}}{2(\pi Dt)^{1/2}}, \qquad m_0 = C_0\delta \tag{4.8}$$

Where δ is the thin middle monomer layer thickness. Putting the minimum residence time t ~ 0.1(s), the critical gel point C*~15%, and the diffusivity D ~ 5 μm²/s into the equation (4.8), we can estimate the z distance that the critical gel point front reach at the minimum residence time.

$$z(C^*) \sim \sqrt{2\ln\delta + 2} \tag{4.9}$$

The previous literature demonstrated that the minimum flow focusing thickness (δ_{min}) would be 0.5 μm [113]. Then, the smallest particle height, $H_{p,\,min}$ is,

$$H_{p,\min} \sim 2\sqrt{2\ln\delta_{\min} + 2} \sim 2\mu m \tag{4.10}$$

In experiments, the minimum particle height that we achieved was ~ 3 μm, which was close to the resolution noted above. Also, the transverse resolution was comparable with the one) that conventional FL techniques have provided. In our current setup, the transverse resolution for former FL techniques was 2 μm, which was achieved in 4.5 μm high channels [86].

4.5 Maximum Residence Time

In the synthesis of particles using inert lubrication layers, a short residence time is desirable in order to minimize the monomer/species diffusion into inert flows. However, complex particles that are generated by applying gravitational, magnetic or electrical fields often require longer residence times so that the external field can act sufficiently upon the system. For example, structurally colored particles are typically prepared with a residence time >1s to tune one-dimensional photonic crystal colors by magnetic field modulation and to fix the color with localized UV exposure [76].

4.5.1 Transverse Diffusion

To investigate transverse diffusion of monomer and the suitability of our strategy for longer residence times, we designed an experiment to visualize the diffusional thickness of PEG-DA 575 in PEG 200 (Fig. 4.15a). In this experiment, we used PDMS channels to generate co-flows with a simple two-dimensional flow-focusing technique. One of the co-flows was a green inert flow while the other was a gray monomer flow. We stopped the flow for specified

amounts of time to allow monomer to diffuse into the inert flow. Then, we synthesized "T"–shaped particles at the fluid interface such that the head of the "T" was aligned with the interface and the leg of the "T" could be used as an indicator of monomer penetration length (δ). Because the stop time was much larger than the sum of the flow and exposure times (~100 ms), we assumed the residence time to be roughly equal to the stop time. As shown in Figure 4.15b, the diffusion length increased when the residence time was increased, and the value of the slope (0.5) in a log-log plot of diffusional thickness (δ) versus residence time (t) confirmed the diffusion-based transport (Fig. 4.15c).

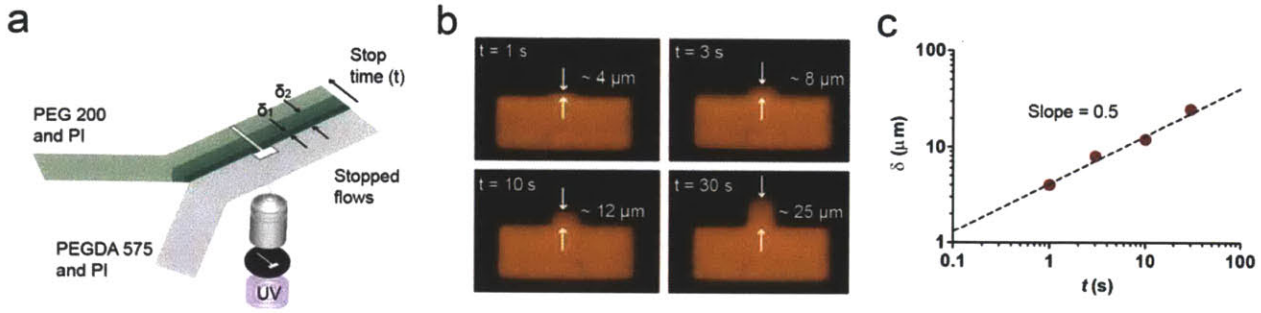

Figure 4.15: *Transverse monomer diffusion (a) Experimental setup for measurement of diffusion coefficient of PEG-DA 575 in PEG 200 in a PDMS device. The green stream consists of PEG 200 90% (v/v), PI 5% (v/v), food coloring 4% (v/v), and rhodamine acrylate 1% (v/v), while the gray stream is comprised of PEG-DA 575 94% (v/v), PI 5% (v/v), and rhodamine acrylate 1% (v/v). "T"-shaped exposure mask was used to determine the penetration depth (δ) of PEG-DA. (b) Fluorescence images of particles produced with various residence times. (c) Penetration depth as a function of residence time.*

4.5.2 Estimation of Monomer Diffusivity

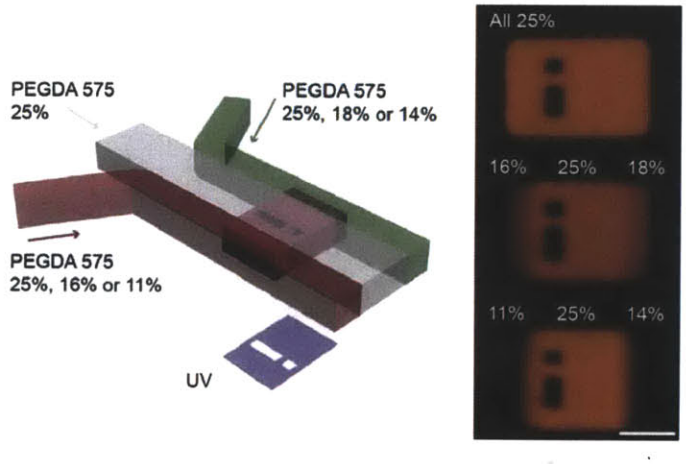

Figure 4.16: *Variation of PEG-DA 575 loading percentage to determine critical gel point (~15% monomer concentration) Synthesis was performed in PDMS devices, and all streams contained rhodamine acrylate for visualization of particle interfaces.*

When residence time is long, the diffusional broadening of monomers lead to additional polymerization thickness. The polymerization can proceed to until the reaction is terminated at the critical gel point of monomer. As a result, the end of diffusional length (δ) is the position of critical gel point (C*). We determined the critical gel point of the monomer (~15%) by visually checking for gelation at various monomer concentrations (Fig. 4.16). As we know the position of C* on a specific time, we can extract diffusion coefficient of monomer from a diffusion model. We used infinite 1D transient diffusion model as the diffusion characteristic time (10000s) was much larger than the investigated time scale (30s). The diffusion characteristic time was estimated by $L^2/D_{PEGDA575}$ where L is 250 μm, the half of channel width. We also assumed that channel wall effects could be neglected considering the monomer diffusion in the middle plane of the channel [128]. For infinite 1D transient model, well-established theoretical solution exists as so-called error function. Using the function and measured data, we estimate the diffusion coefficient of PEGDA 575 (in PEG 200) as 4.5 $\mu m^2/s$.

Time (s)	1.0	3.0	10.0	30.0	Average
Diffusivity ($\mu m^2/s$)	4.0	5.3	3.6	5.2	4.5

Table 4.7 *Estimated diffusivity of PEGDA 575 in PEG 200*

We compare the measured diffusivity with the value estimated from a previous literature [129]. The bulk diffusivity of PEG in water at 25 °C can be calculated from the following) equation.

$$D_{PEG} = 1.465 \times 10^{-4} \times \overline{M_W}^{-0.557} \qquad (cm^2/s) \tag{4.11}$$

We use this equation to estimate diffusivity of PEGDA 575 assuming PEGDA has similar diffusional behavior with PEG. Also, we neglect temperature differences between experiments. Then, the diffusivity of PEGDA 575 in water can be estimated to be 425 $\mu m^2/s$. To find the diffusivity of PEGDA 575 not in water (μ=1 cP) but in PEG200 (μ=57 cP), we use the Stokes-Einstein relation between viscosity and diffusivity.

$$\frac{\mu_{PEG200}}{\mu_{WATER}} = \frac{D_{PEGDA575} \quad \text{(in WATER)}}{D_{PEGDA575} \quad \text{(in PEG200)}} \tag{4.12}$$

The final diffusivity of PEGDA575 in PEG 200 was 7.5 $\mu m^2/s$. The estimated value is on the same order of magnitude with the measured diffusivity.

4.5.3 Theoretical Estimation for Maximum Residence Time

We then returned to the layered flow system of the gas-impermeable devices. In tri-layered stopped flows, monomer in the middle layer can be diffused into inert layers as time pass by.

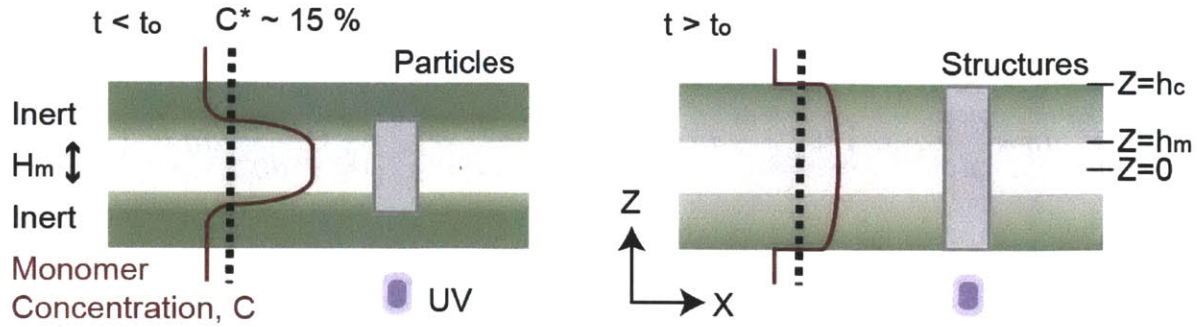

Figure 4.17: *Schematic descriptions for time evolution of monomer concentration. We estimate theoretical maximum value of time, t0, at which critical gel point front reaches walls of gas-impermeable device and induces particle sticking.*

We find the analytical solution for the time evolution of monomer concentration assuming 1D transient diffusion. In the first step, we write following governing equation and boundary conditions (BC's).

$$\frac{\partial C}{\partial t} = D\nabla^2 C, \qquad \frac{\partial C(h_c,t)}{\partial z} = 0, \qquad \frac{\partial C(0,t)}{\partial z} = 0 \tag{4.13}$$

Initial condition (IC) will be given in a step function of monomer concentration at time 0.

$$C(h,0) = \begin{cases} C_0 & (0 < h < h_m) \\ 0 & (h_m < h < h_c) \end{cases} \tag{4.14}$$

Using dimensionless groups,

$$\Theta = \frac{C}{C_0}, \qquad \eta = \frac{h}{h_c}, \qquad \tau = \frac{t}{h_c^2 / D} \tag{4.15}$$

We non-dimensionalize the governing equation, BC's and IC.

$$\frac{\partial \Theta}{\partial \tau} = \nabla^2 \Theta, \qquad \frac{\partial \Theta(1,\tau)}{\partial \eta} = 0, \qquad \frac{\partial \Theta(0,\tau)}{\partial \eta} = 0, \qquad \Theta(\eta,0) = \begin{cases} 1 & (0 < \eta < a) \\ 0 & (a < \eta < 1) \end{cases}, \qquad a = \frac{h_m}{h_c} \tag{4.16}$$

To solve this equation, we use Fast Fourier Transformation (FFT) method.

$$\Theta(\eta,\tau) = \sum_{n=1}^{\infty} \Theta_n(\tau)\Phi_n(\eta), \qquad \Phi'(1) = 0, \qquad \Phi'(0) = 0 \tag{4.17}$$

Considering the BC type, we can choose the case IV for basis function [127].

$$\Phi_0(\eta)=1, \qquad \Phi_n(\eta)=\sqrt{2}\cos n\pi\eta \qquad \text{(case IV)} \tag{4.18}$$

Then, we perform FFT transformation of the equation and IC. FFT transformation of the equation,

$$\int_0^1 \Phi_n \frac{\partial\Theta}{\partial\tau}d\eta=\frac{d\Theta_n}{d\tau}, \qquad \int_0^1 \Phi_n \frac{\partial^2\Theta}{\partial\eta^2}d\eta=\left[\Phi_n\frac{d\Theta}{d\eta}-\Theta\frac{d\Phi_n}{d\eta}\right]_{\eta=0}^{\eta=1}+\int_0^1\Theta\frac{d^2\Phi_n}{d\eta^2}d\eta=-(n\pi)^2\Theta_n$$

$$\frac{d\Theta_n}{d\tau}+(n\pi)^2\Theta_n=0, \qquad \Theta_n(\tau)=c_n e^{-(n\pi)^2\tau} \tag{4.19}$$

FFT transformation of the IC

$$\int_0^1 \Phi_n\Theta(\eta,0)d\eta=\Theta_n(0) \qquad \Theta_0(0)=a \tag{4.20}$$

$$\int_0^1 \Phi_n\Theta(\eta,0)d\eta=\int_0^a\sqrt{2}\cos n\pi\eta d\eta=\left[\frac{\sqrt{2}\sin n\pi\eta}{n\pi}\right]_0^a=\frac{\sqrt{2}\sin n\pi a}{n\pi} \qquad (n=1,2,3...) \tag{4.21}$$

$$\therefore \qquad \Theta_0(\tau)=a \qquad ,\Theta_n(\tau)=\frac{\sqrt{2}\sin n\pi a}{n\pi}e^{-(n\pi)^2\tau} \qquad (n=1,2,3...) \tag{4.22}$$

The analytical solution for time evolution of monomer concentration,

$$\Theta(\eta,\tau)=a+2\sum_{n=1}^{\infty}\frac{\sin n\pi a}{n\pi}e^{-(n\pi)^2\tau}\cos n\pi\eta \tag{4.23}$$

We can use the analytical solution to find maximum residence time t_0, at which critical gel point front reaches channel walls and particle sticking happens. When the h_m/ h_c is 0.5, the maximum residence time is estimated to be 5.1s from τ satisfying θ (0.99, τ) = 0.16 (from 15% critical gel point and 95% C_0).

4.5.4 Simulation Estimation for Maximum Residence Time

In addition, an accompanying COMSOL simulation showed good agreement with the maximum residence time calculated from the analytical solution (Fig. 4.18). For the case in which the middle monomer layer thickness (Hm) is 20 μm, we perform COMSOL simulation to check whether the 15% monomer concentration arise on the channel walls after 5.1s. In this simulation, we used 2D rectangular constriction (40 μm × 250 μm) for channel intersection and 5 $\mu m^2/s$ diffusivity of monomer. The concentration through the constriction was calculated using COMSOL Multiphysics finite element modeling software for a given monomer concentration at time 0s. As shown in the plot of Figure 4.18b, the

critical gel point front reaches channel walls after the maximum residence time, 5.1s. At infinite time, the concentration converges to 47.5% which is the half of the initial monomer concentration.

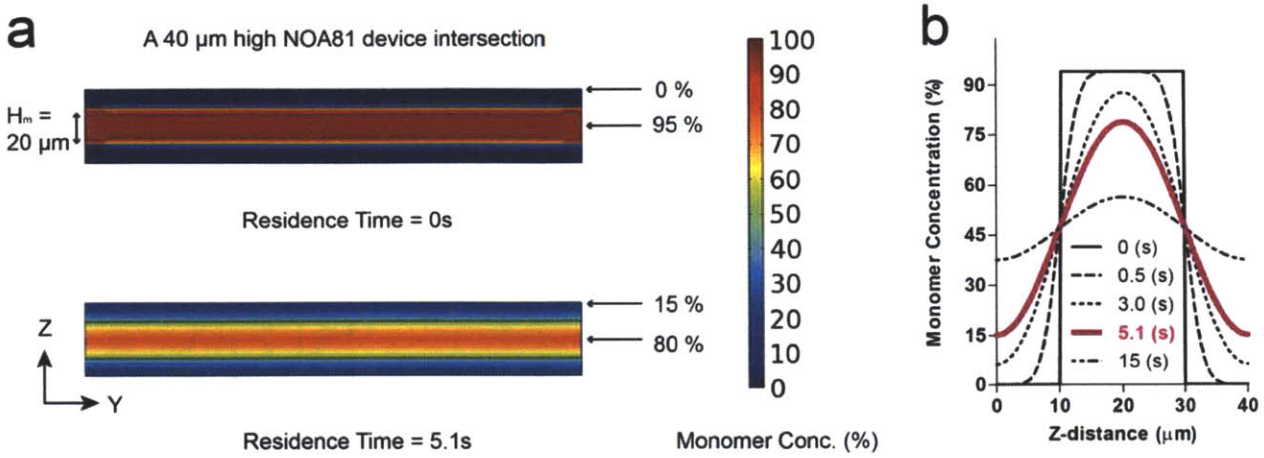

Figure 4.18: *COMSOL simulation for time evolution of monomer concentration in a slit-like NOA81 device (a) Simulation solution indicates the maximum residence time is 5.1 s for the creation of particles at H_m = 20 μm. (b) A plot for monomer concentration versus z-distance.*

4.6 Oxygen-free FL with Organic Precursors

Perhaps the most valuable feature of the oxygen-free FL in NOA devices is the ability to synthesize anisotropic particles using organic solvents, a process which is not possible with current PDMS-based FL approaches.

4.6.1 Particle Synthesis Using Organic Solvents

We demonstrated the synthesis of anisotropic particles encapsulating ruthenium complex (II) dyes dispersed in methanol/toluene (4:1 v/v) mixture (Fig. 4.19a). Previous work has shown that encapsulated ruthenium dyes in PEG structures can be used for oxygen sensing applications [130, 131]. Furthermore, particle-based sensors offer several detection advantages over microarrays and similar arrangements of immobile structures, including faster capture kinetics and rapid probe-set modification for more flexible assays [76, 78]. For this study with NOA81 devices and inert flows, we successfully synthesized triangular particles that exhibited homogeneous fluorescent signal, thus confirming entrapment of the ruthenium dyes (Fig. 4.19b and c). This proved that the new FL process could encapsulate functional entities inside particles with the same spatial resolution and efficacy as prior methods. We also synthesized geometrically complex particles from water-insoluble monomers dissolved in toluene (Fig. 4.19d). We chose to demonstrate this capability with

TMPTA (Trimethylolpropane triacrylate, ρ = 1.06 g/ml) and PUA (Polyurethane acrylate, ρ = 1.09 g/ml), water-insoluble monomers with applications in particle assembly [91] and soft molding [112], respectively. We could easily modulate the monomer composition in toluene to tune both chemical and mechanical properties of the microparticles. In this hydrophobic monomer system, we replaced the previously used PEG 200 inert flows with tergitol NP-10 (ρ = 1.06 g/ml) because the hydrophilic PEG was immiscible with the monomers and produced curved particle surfaces. The amphiphilic tergitol surfactant had good miscibility with and the same density as the monomers selected. In tri-layered tergitol-monomer-tergitol flows, we successfully created TMPTA and PUA particles using two different mask shapes (Fig. 4.19e and 4.19f). The generated particles were optically transparent and rigid enough to allow for rinsing in organic solvents without swelling-based deformation.

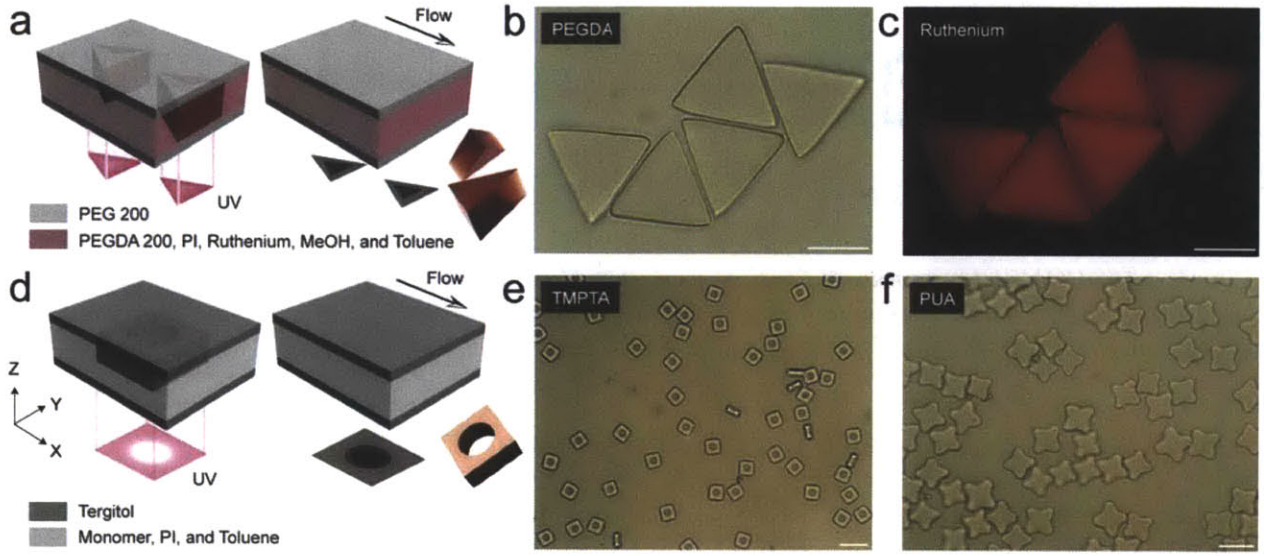

Figure 4.19: *Anisotropic particle synthesis from organic precursors (a) Triangular particle synthesis with PEG 200 inert flows in an NOA channel from organic precursor containing PEG-DA 200, ruthenium dye (mixed with methanol (MeOH) and toluene), and PI. (b and c) Brightfield and fluorescence images of triangular particles synthesized in (a). (d) Particle synthesis in NOA device with water-insoluble monomers (trimethylolpropane triacrylate (TMPTA) and polyurethane acrylate (PUA), mixed with toluene) and PI. Inert flows consisted of Tergitol surfactant to lower surface energy and prevent curvature in top and bottom faces of particle. (e and f) Images of particles synthesized from TMPTA and PUA. Scale bars are (b and c) 30 μm, (e) 100 μm, and (f) 50 μm.*

4.6.2 Synthesis of Near-infrared-active Anisotropic Particles

To further demonstrate the utility of oxygen-free FL, we synthesized near-infrared-active anisotropic particles from organic precursors. Near-infrared (NIR) fluorescence is emitted in a "biologically transparent" window thereby minimizing auto-fluorescence interference and tissue scattering [132]. Through the use of organic precursors that contain NIR-active nano-entities, we introduce unprecedented shape-encoded particles which exhibit NIR

fluorescence around the NIR II region (wavelengths between 1 ~ 1.4 μm) to maximize light penetration depth in tissue [133]. NIR-active QDs are more easily prepared in organic solvents than in water because the former provide synthetic advantages for the production of narrow size distributions as well as a wide range of available sizes [134]. The highest quality QDs produced from organic solvents are both hydrophobic and water-insoluble, making them incompatible with former FL techniques. We purchased commercial hydrophobic QDs dispersed in toluene and bearing a CdTeSe/ZnS core-shell structure with a NIR 915 nm emission peak. To ensure high trapping efficiency of the small QDs (1-10 nm) within the polymer matrix, we used NOA81 instead of PEG-DA. Although the minimum pore size of our PEG system can reach ~ 1 nm [104], PEG hydrogel particles can swell in water, leading to leakage of physically encapsulated QDs, a process that could introduce serious toxicity issues for potential biological applications. NOA81 is biocompatible and has smaller pores, which prevents the loss of entrapped QDs. To evenly disperse QDs in NOA81, we mixed the monomer with a QD solution at a 1:1 volume ratio. Then, we placed the resulting mixture layer between inert tergitol layers and produced triangular particles. The particles physically encapsulated QDs, as shown by the strong near-infrared photoluminescence (PL) signals in Figure 4.20a. Next, we synthesized particles with different loading concentrations of QDs and quantified the PL intensities exhibited by each batch. As expected, we found a simple linear relation between loading concentration and PL intensity (Fig. 4.20b).

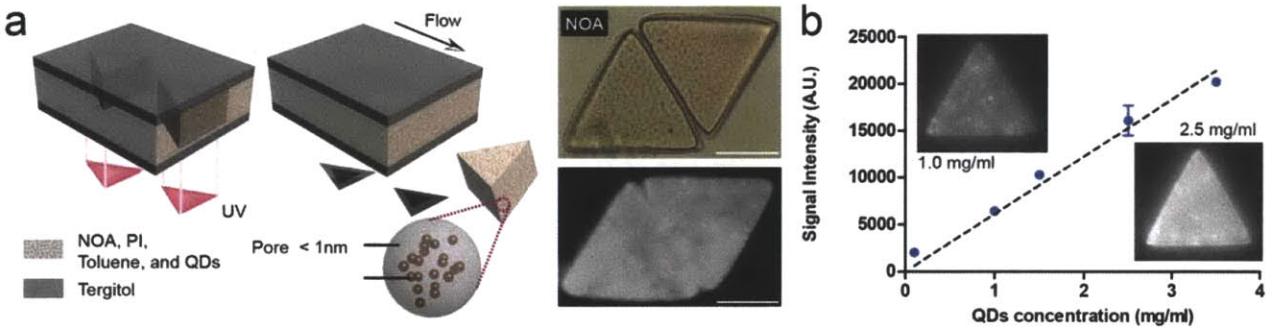

Figure 4.20: *Synthesis of near-infrared (NIR)-active anisotropic particles (a) NIR-active triangular particle synthesis. NIR emitting CdTeSe/ZnS quantum dots (QDs) were physically entrapped in NOA polymer particles produced in NOA device. (b) Fluorescent signal intensity as a function of quantum dot loading concentration. Fluorescence was integrated over a circle of radius 30 μm centered on the triangular particles. Each point represents mean measurement from three particles; error bars represent standard deviation.*

4.7 Discussion

Oxygen-free FL greatly expands the synthesis capabilities of FL in the following three categories: device construction, process control, and operable material. The new technique can be used in virtually any type of device, whereas conventional FL techniques have been

limited to PDMS devices. To achieve this flexibility, we utilized the iCVD nanoadhesive bonding technique for device construction. This strong and highly flexible bonding method greatly augments the range of devices that can be used, which in turn provides a variety of unique environments for particle synthesis. For example, the synthesis described here with the iCVD nano-adhesive and inert flows could be integrated with indium tin oxide (ITO) substrate for the fabrication of three-dimensional photonic crystal particles via dynamic modulation of electric fields [135]. Another advantage of oxygen-free FL is that the technique offers process control that is superior to former FL techniques. The use of hard devices and the high-strength bonding method provides a considerable reduction of process time scales for channel relaxation, polymerization, and flow. Also, the programmable sheath-like inert flows allow for on-the-fly alteration of particle height, a significant advantage over the current method in which particle height is dictated by channel height. Finally, oxygen-free FL greatly expands the library of synthesis materials that can be used, enabling the creation of particles from previously inaccessible reagents such as organic solvents. Through the fabrication of solvent compatible NOA81 devices, we synthesized new multifunctional particles from seven distinct organic precursors including four monomers (PEGDA, TMPTA, PUA, and NOA) for supporting matrix and three nano-entities (ruthenium, QDs and SWNTs) for functional units. Also, we demonstrated the synthesis of near-infrared barcoded particles capable of label-free and real-time detection of analyte. Significantly, all functions of the barcoded particles work around the second near-infrared window, which greatly reduces the likelihood of signal interference from tissues, cells, and biofluids in potential in-vivo multiplexed sensing applications. By allowing for a new range of synthesis conditions and environments, we believe that oxygen-free FL can be a powerful means to achieve novel categories of functional particles for diverse applications.

Chapter 5

Advanced Barcoded Particles

Multifunctional barcoded particles have been developed by Doyle group as promising diagnosis tools for rapid screening of biomolecules. The hydrogel barcoded particles have exhibited high sensitivities and favorable hybridization kinetics, providing water-like environments. The earliest form of barcoded particles was Janus type which had two compartments of graphical codes and probes. The particles were produced by standard SFL using precise mask alignments across the interface of two laminar flows. These barcoded particles were designed for the multiplexed detection of target biomolecules, bearing over a million unique codes to identify loaded probes. In multiplexed assays, the barcoded particles are rapidly scanned in a microfluidic device, passing a detection region where the codes are recognized and targets quantified. After the primitive version of barcoded particles emerged, control regions were added to the barcoded particles to provide the basis of target quantification. Also, the shape of the barcoded particles was changed for high-throughput flow alignment of the particles. The development of advanced flow lithography could further allow us to modify the barcoded particles to enhance functionalities, introducing new structures and materials. In this section, we present following three kinds of advanced barcoded particles: (1) magnetic barcoded particles, (2) reinforced barcoded particles, and (3) near-infrared barcoded particles.

5.1 Magnetic Barcoded Particles

Magnetic polymer particles consist of magnetically addressable components entrapped within or coated on a polymer matrix that can be precisely tuned to exhibit a range of desired physical and chemical properties. This powerful combination of functionality and customization has enabled the use of such particles in biomedical applications [62, 136-138], micro-scale assembly [29, 139-141], structural color printing [142], imaging [143], and purification technology [144]. In addition, the particles have been employed in microfluidic channels for bioassays [145-148], mixing [149-151], trapping [152], transporting [153], and separation [154-158]. Recently, biological entities including cells and aptamers were labeled with magnetic polymer particles and subsequently separated in a spatially-addressable sorting manner by generating magnetic field gradients in microfluidic channels [159, 160]. The enormous potential of magnetic polymer particles has fueled the development of several distinct synthesis methods. The conventional emulsification methods based on homogenization use shear forces to encase superparamagnetic nanoparticles of metal oxides within polymer droplets [161]. Unfortunately, these approaches produce droplets with a wide size distribution and consume large amounts of energy [161]. Membrane [162] and microchannel emulsifications [163-165] have been introduced as alternative methods that can provide higher degrees of monodispersity for a fraction of the energy cost. Microchannel emulsification in particular has produced anisotropic magnetic gel particles using channel geometries [163] or a double emulsion technique [164]. Janus superparamagnetic gel particles have also been generated with this approach [165]. However, the above methods have limited the particle morphologies to spheres or deformed spheres. A more flexible synthesis system would expand the possible geometries and thereby augment the applicability of the magnetic polymer particles produced. Encoded microparticles have been suggested as diagnostic tools for the rapid, multiplexed screening of biomolecules due to their advantages in detection and quantification [7, 166, 167]. Compared to traditional planar arrays, particle-based arrays offer easier probe-set modification, more efficient mixing steps, and higher degrees of reproducibility. While polymer microspheres doped with fluorescent dyes have been used most extensively [168], there are numerous systems under development that employ chemical, graphical, electronic, or physical encoding schemes for use in multiplexed detection [166]. Microcarriers fabricated from a variety of advanced materials such as inverse-opaline photonic beads [169] have the potential to transform the biodiagnostic field by enabling the analysis of complex sample media (such as serum), eliminating the need for costly and time-consuming labelling steps, and lowering limits of detection. Barcoded hydrogels are an emerging subclass of encoded particles that exhibit higher sensitivities and more favorable hybridization kinetics than common metallic and polystyrene microparticles that immobilize probe species on solid surfaces [77]. To capture target molecules and report interaction information in multiplexed analysis, each anisotropic particle bears a probe region and a corresponding graphical code region that identifies the probe species. Production of these particles requires a novel synthesis method called stop flow lithography

(SFL), which affords precise control over morphology and functionality through the semi-continuous photopolymerization across coflowing laminar streams of various chemical compositions in microfluidic channels. While the resulting gel-based particles have proven to be effective tools in past multiplexed sensing of DNA and RNA, their use in suspension assays and other screening processes would be greatly simplified with the introduction of an appropriate means for addressing and aligning the particles during rinsing, mixing, and analysis procedures. Magnetic barcoded particles are now introduced as an enhanced version of hydrogel microparticles for suspension assays that can be manipulated using magnetic fields. Through a slight modification of the SFL technique [73], it is now possible to incorporate magnetically addressable entities within a specific region of the microparticles. Particles synthesized with a magnetic tail region respond to weak magnetic fields, while still maintaining the ability to sensitivity and specifically detect oligonucleotide targets in solution. The advantages of the magnetic tail are demonstrated through directed orientation as well as bulk separation using a magnet.

5.1.1 Experimental Methods

Materials

All particles shown in this work were made from poly(ethylene glycol) (700) diacrylate (PEG-DA 700, Sigma Aldrich). The code regions were synthesized using prepolymer solutions of 35% (v/v) PEG-DA 700, 20% poly(ethylene glycol) (200) (PEG 200, Sigma Aldrich), 5% Darocur 1173 (Sigma Aldrich) initiator, and 40% 3× Tris-EDTA (pH =8.0, EMD) buffer. Rhodamine acrylate (Sigma Aldrich) and food coloring (Tone Brothers Inc.) were mixed into the prepolymer solutions for the code to give final concentrations of 0.4% and 2%, respectively. The composition of prepolymer for the probe regions was 20% PEG-DA 700, 40% PEG 200, 5% Darocur 1173, and 35 % 3× Tris-EDTA buffer. Oligonucleotide probes, #1 (5'-ATA GCA GAT CAG CAG CCA GA-3') and #2 (5'-CAC TAT GCG CAG GTT CTC AT-3'), were purchased from IDT with acrydite modifications on the 5' end and mixed into the probe prepolymer to give a final concentration of 50 μM. Lastly, the magnetic region was prepared using solutions of 35% PEG-DA 700, 5% Darocur 1173, and 60 % magnetic bead solutions (Seradyn Inc., carboxylate-modified, 5% solids). Prior to being incorporated into the particles, the commercial superparamagnetic beads exhibited a short response time upon the introduction of a magnetic field, a high saturation magnetization value of 25 emu/g, and had uniform size (779 nm ± 10%, diameter). A perfusion solution consisting of PEG-DA 700 was also used to move un-incorporated magnetic beads into a waste reservoir to prevent the excess beads from sticking to the probe and code regions of the synthesized particles.

Microfluidic Devices and SFL Setup

In each device, the particle synthesis chamber was 300 μm in width and 20 μm in height, while the perfusion channel was 70 μm in width and 110 μm in height. For synthesis,

devices were mounted on an inverted microscope (Axiovert 200, Zeiss) equipped with a VS25 shutter system (UniBlitz) to precisely control the UV exposure dose. A reservoir was cut into the PDMS to collect the particles. The other setups were same with Chapter 2.

Magnetic Responsiveness

To investigate the response of the magnetic barcoded particles in the presence of an external magnetic field, we fabricated analysis reservoirs by sealing a PDMS rectangular frame (5 × 5 × 5 mm) onto a PDMS-coated glass slide. Each reservoir was filled with the magnetic barcoded particles suspended in deionized water with 0.005% (v/v) Tergitol NP-10 (Sigma Aldrich, St. Louis,MO) (to reduce interfacial tension that can cause hydrogel particles to stick together) and then placed in a uniform magnetic field (planar or normal) induced by an electromagnetic coil connected to a DC power supply (GPS-2303, GWInsteck). The magnetic fields were calibrated using a Gauss meter (SYPRIS) with an axial probe (for the normal induced magnetic field) or a transverse probe (for the planar induced field).

Hybridization and Labeling

Incubation mixtures were prepared by adding ~ 50 particles of each desired type to a 0.65 mL Eppendorf tube containing a hybridization buffer of 0.5 M NaCl in TET (1× Tris-EDTA with 0.05% Tween-20 (Sigma Aldrich)). Particles were incubated with either 0 or 200 amol of two different biotinylated target oligonucleotides at 50 °C for 90 min using a thermomixer (Quantifoil Rio) with a mixing speed of 1800 rpm. Following hybridization, the samples were rinsed twice with 450 µl TET and then twice with 450 µl PBST (1× PBS (Cellgro) with 0.05% Tween-20). Then, the probe-target complexes were labeled by adding streptavidin-phycoerythrin (SAPE) diluted 1:500 in TET to the Eppendorf tube. The labeling process was carried out at 21.5 °C for 45 min with mixing at 1500 rpm in a Multi-Therm shaker (Biomega). Before imaging, the particles were rinsed three times with 450 µl TET and then twice with 450 µl PTET (5× Tris-EDTA buffer with 25% PEG 200 and 0.05% Tween-20).

Imaging for Quantitative Analysis

A 15-µl droplet containing ~ 20 particles was pipetted onto a glass slide and sandwiched for analysis using an 18 × 18 mm coverslip. The sample was mounted on a Zeiss Axiovert 200 microscope equipped with a UV Illumination source (X-Cite series 120, Exfo), and a custom macro in NIH Image was used to capture ten sequential frames from an EB-CCD camera (C7190-20, Hamamatsu) mounted to the side port of the microscope. Each frame had an exposure time of 1/33 sec, and the macro produced a final output image for analysis by averaging over the ten frames. Camera settings of 10, 1.6, and 9.9 for gain, offset, and sensitivity, respectively, were used. Images were analyzed using Image J.

5.1.2 Synthesis of Magnetic Barcoded Particles

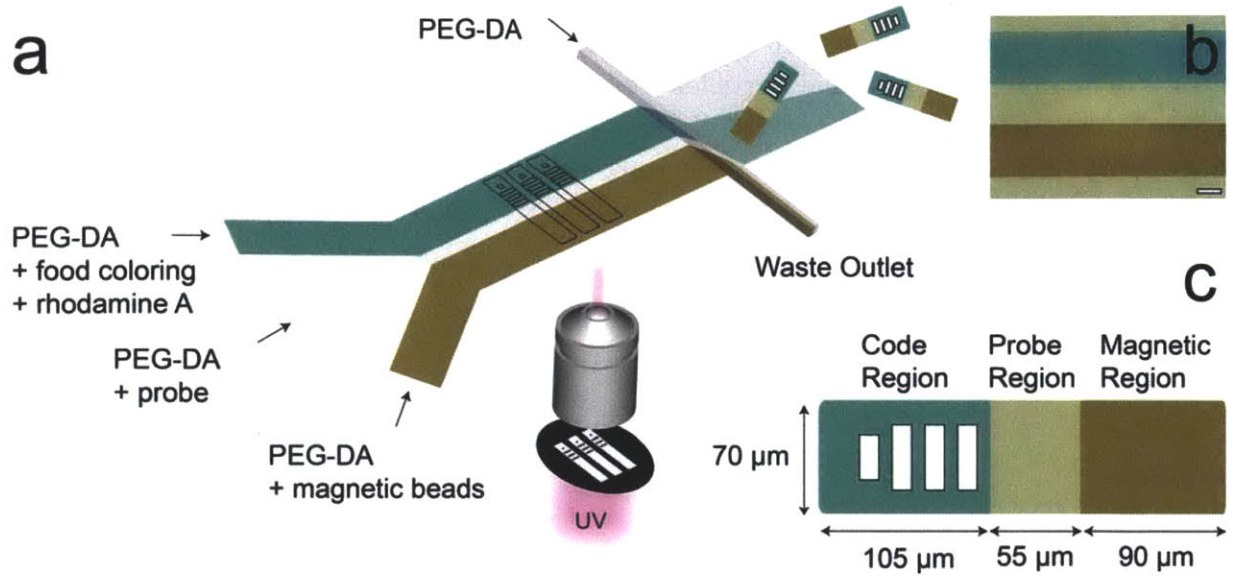

Figure 5.1: *Production of magnetic barcoded particles. (a) Synthesis process of magnetic barcoded particles. Stop flow lithography (SFL) is used to generate particles with three distinct chemical regions. The top stream is comprised of PEG-DA with food coloring and rhodamine A, while the other streams consist of PEG-DA with probe oligonucleotide and magnetic beads, respectively. Downstream of the synthesis site, a PEG-DA perfusion stream is used to move un-incorporated magnetic beads into a waste outlet. (b) An experimental bright field image of the three phases flowing in the channel. The magnetic beads in the bottom flow are seen to be well-dispersed. (c) Dimensions of a magnetic barcoded particle. Coding holes are designed with the following dimensions: '1' (12 × 15 µm), '2' (12 × 27.5 µm), and '3' (12 × 40 µm). The code in this illustration is '2333'. The scale bar is 50 µm.*

Figure 5.1a shows a schematic depicting the synthesis of magnetic barcoded particles. Different prepolymer mixtures are infused into the three inlets, thereby generating stable three-phase laminar flows. The middle stream is composed of PEG-DA with an acrylate modified DNA probe, while the top and bottom streams consist of PEG-DA with a fluorescent dye, rhodamine acrylate, and with magnetic beads, respectively. The flows can be stopped via pressure release, during which an array of magnetic barcoded particles are formed by a 75 ms UV exposure through a transparency mask using a standard fluorescence microscope. A pressure pulse is then used to advect the polymerized particles into a collection reservoir. This process is repeated using an automated setup, allowing for the high-throughput synthesis of particles (18,000 per hour) in a semi-continuous manner. Prior to collection in the reservoir, a perfusion stream with flow perpendicular to that in the synthesis chamber was used to move un-incorporated magnetic beads into a waste outlet. This technique was introduced to simplify the rinsing procedures. While the excess beads flowed into the perfusion line, the much larger encoded particles were only collected in the

reservoir of the synthesis chamber. The commercially available superparamagnetic beads were well-mixed with PEG monomer solutions and well-dispersed in microfluidic channels (Fig. 5.1b). Aside from the addition of the simple perfusion stream, no special processing steps or chemical treatments were required to integrate the magnetic streams into the SFL process. The magnetic barcoded particles were comprised of three distinct regions: (1) code region for identifying particle and probe embedded within, (2) probe region for detecting target, and (3) magnetic region for providing magnetic addressability. The dimensions of each region were 105 × 70 μm, 55 × 70 μm, and 90 × 70 μm, successively (Fig. 5.1c).

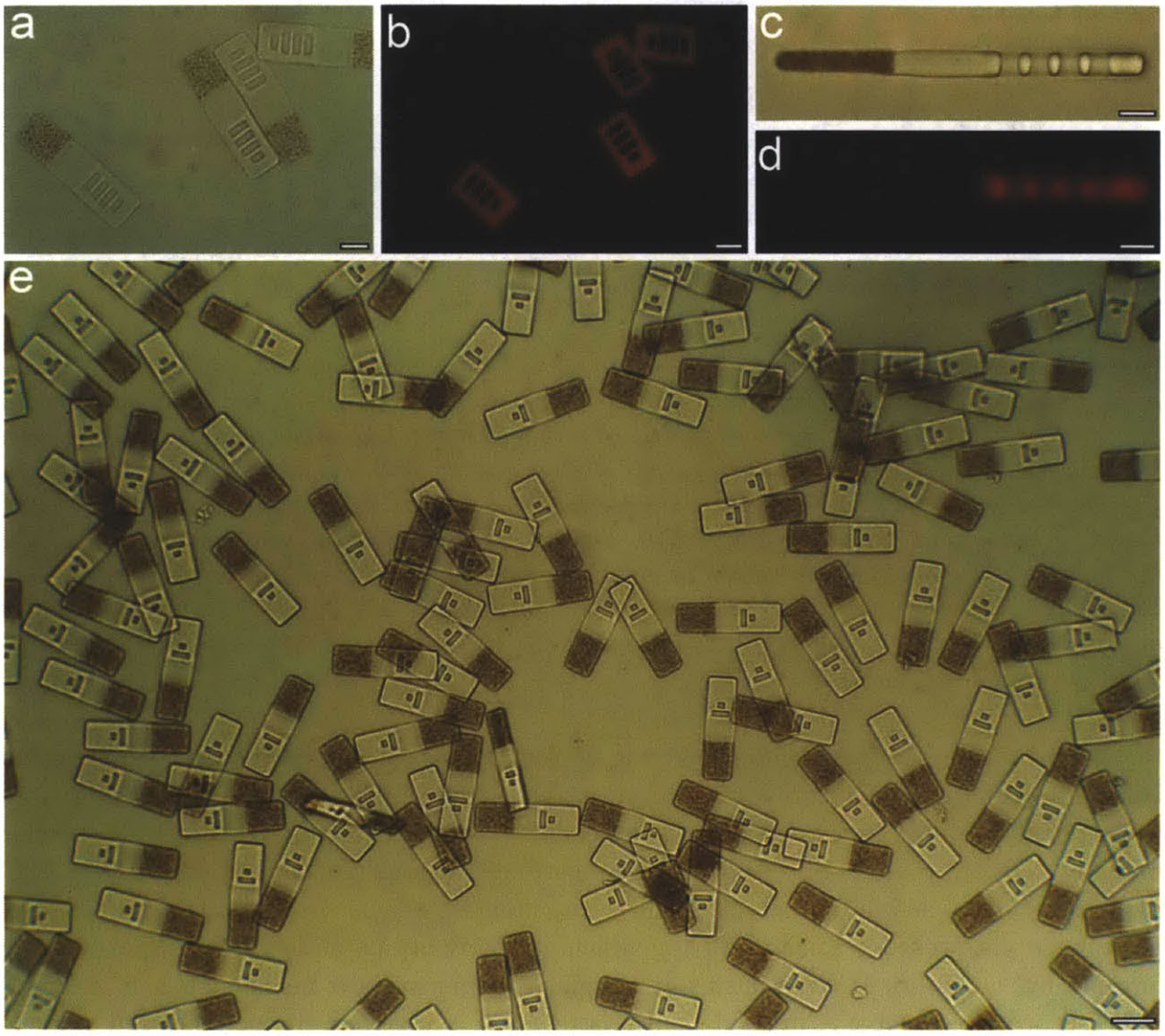

Figure 5.2: *Magnetic barcoded particles. (a) A bright field image (20× objective) of magnetic barcoded particles with code '2333'. (b) A fluorescent image of (a). (c) The side view of a magnetic barcoded particle in a bright field image (20× objective). (d) A fluorescent image of (c). (e) A bright field image (5× objective) of magnetic barcoded particles with code '0013'. Scale bars are 50 μm (a and b), 25 μm (c and d) and 100 μm (e).*

The size (0, 1, 2, and 3) and order of unpolymerized holes in the wafer structure were used to construct a graphical code to distinguish particle types. The number "0" was designed as a non-punched area, while the punched dimensions of numbers "1", "2", and "3" were 12 × 15 μm, 12 × 27.5 μm, and 12 × 40 μm, respectively. Careful focusing and inlet pressure control during the photopolymerization process ensured a high degree of reproducibility in the creation of the coding holes and the different chemical regions on each microparticle. Figure 5.2 contains images of the synthesized magnetic barcoded particles. As seen in brightfield images (Fig. 5.2a, c and e), the brown magnetic regions are clearly separated from the neighboring probe regions. Well-developed code regions are shown in fluorescent images (Fig. 5.2b and d), with sharp interfaces and feature resolution provided by the SFL process. We prepared magnetic barcoded particles ~ 16 μm in height by using 20 μm-high channels (Fig. 5.2c). The difference between particle and channel heights can be attributed to the ~ 2 μm-thick oxygen inhibition layer on both the top and bottom channel surfaces. Compared to code and probe regions, it was observed that the magnetic region was slightly thinner due to UV absorption by the iron oxide cores of the magnetic beads. We also observed that the code regions were thinner than the probe regions. Compared to the code regions, the probe regions were synthesized using twice the concentration of porogen (PEG 200) in order to provide high porosity for fast transport of target molecules. The higher porosity and lower cross-link density of the gel matrix in the probe regions led to a greater degree of swelling in aqueous solutions.

5.1.3. Saturation Magnetization of Magnetic Barcoded Particles

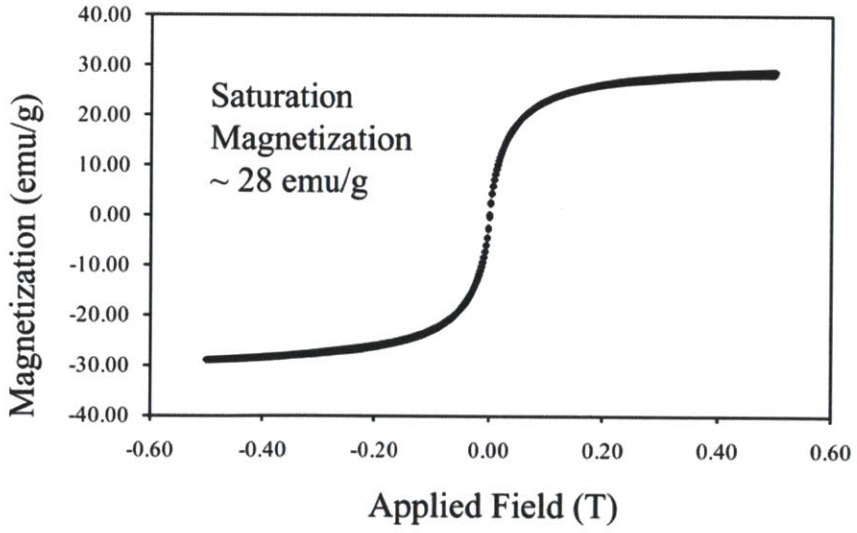

Figure 5.3: *AGM magnetization curve for the commercial magnetic beads that were used in synthesis of the magnetic barcoded particles. The saturation magnetization of the beads was found to be around 28 emu/g.*

Prior to being incorporated into the particles, the commercial superparamagnetic beads had a density of 1.4 g/ml and uniform size (779 nm ± 10%, diameter), and exhibited a short response time upon the introduction of a magnetic field. The reported value for saturation magnetization of the beads was ~ 25 emu/g. Using alternating gradient magnetometry (AGM, MicroMagTM 2900), we made a plot for magnetization of the beads as a function of applied field. The magnetization curve shows superparamagnetic behavior, and no hysteresis was found (Fig. 5.3). In the experiments, the saturation magnetization for the beads was around 28 emu/g, which was quite close to the reported value.

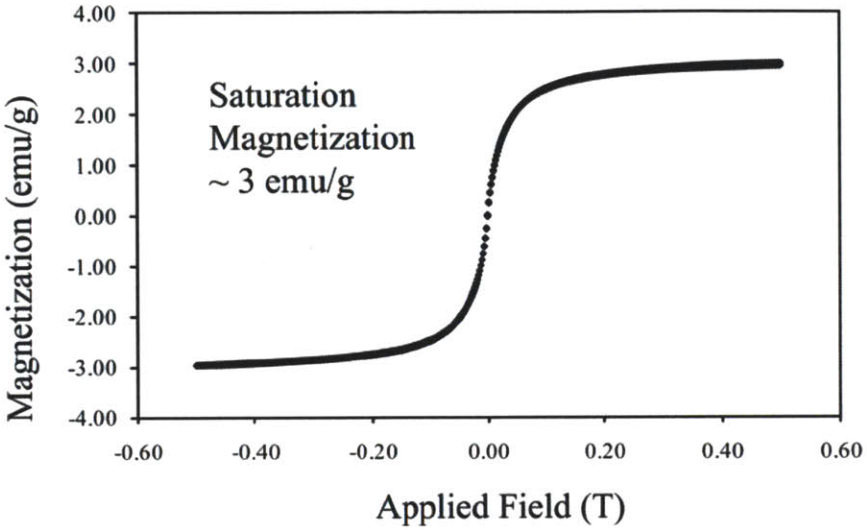

Figure 5.4: *AGM magnetization curve for magnetic regions (dried) of the barcoded particles. The curve also shows superparamagnetic behavior, and no hysteresis was found.*

We also prepared a curve for magnetization of the magnetic regions of the barcoded particles. As the mass of each barcoded microparticle varied depending on the code design, we polymerized particles consisting of only a magnetic region and measured the magnetization value for these simple hydrogels. Like the commercial magnetic beads, the magnetic hydrogels exhibited superparamagnetic behavior and no hysteresis as shown in Figure 5.4. The measured saturation magnetization value for the magnetic regions of the barcoded particles was ~ 3.0 emu/g. From the initial composition of the magnetic prepolymer solution (assuming full conversion of PEG-DA during the polymerization), we estimated the weight ratio of magnetic beads incorporated in the magnetic regions (assuming all beads are encapsulated during polymerization) to be 9.7%. The saturation magnetization value for the magnetic regions was thus anticipated to be 9.7% of the saturation magnetization value for dried beads, ~ 2.7 emu/g. The good agreement between the measured (3.0 emu/g) and estimated (2.7 emu/g) saturation magnetization values for the magnetic regions leads us to conclude that the magnetic content in the regions can be controlled by simply tuning initial compositions of magnetic prepolymer solutions.

5.1.4 Magnetic Response of Magnetic Barcoded Particles

To investigate magnetic response, we exposed the magnetic barcoded particles dispersed in a 0.005% (v/v) aqueous Tergitol NP-10 solution in a PDMS reservoir to a weak homogeneous field (21.1 ± 0.1 mT) perpendicular to the reservoir substrate. Suspended in a non-magnetic medium, the particles acquired dipole moments and flipped up perpendicular to the plane, forming columnar structures along the applied field direction (Fig. 5.5a). In the presence of a weak homogenous field (14.7 ± 0.1 mT) parallel to the substrate plane, attractive induced dipolar interactions lead to tail-to-tail self assembly of the particles (Fig. 5.5b). The magnetic functionality can be used to orient and transport the barcoded particles as shown in Figure 5.6a-c. Using a hand magnet, it was possible to remotely and precisely manipulate the orientation of magnetic barcoded particles at the inlet of a microfluidic channel to aspirate all particles such that they proceeded down the analysis chamber in a "probe first" (versus "code first") orientation. Figure 5.6a shows the reorientation process of a barcoded particle from "code first" to "probe first" within a microfluidic channel.

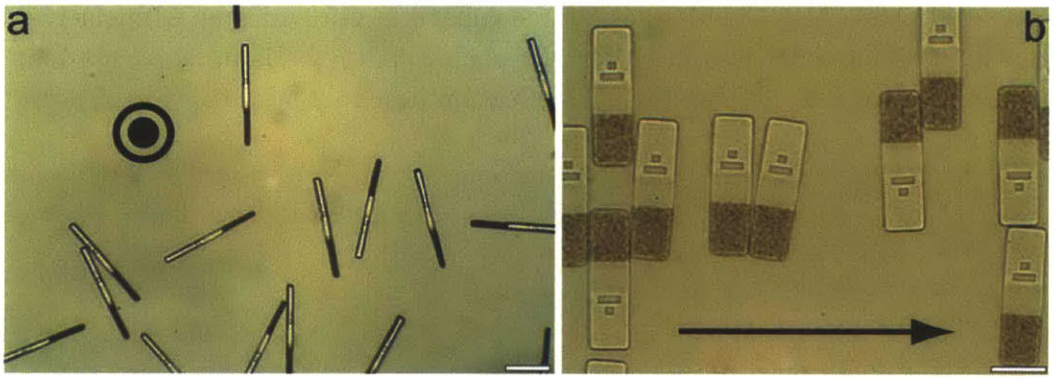

Figure 5.5: *Response of magnetic barcoded particles. (a) Response of magnetic barcoded particles to out-of-plane (21.1±0.1mT) magnetic field. (b) Response of magnetic barcoded particles to in-plane (14.7±0.1mT) magnetic field. Scale bars are 100 μm.*

By moving a more powerful magnet even closer to the channel, it was possible to then transport this reoriented particle from the inlet to a more narrow zone used for single-particle analysis (Fig. 5.6b). Although the transportation velocity was only 10 μm/s in this experiment, the process was performed in a simple manner using a common magnet. This pumpless method for orientation and movement does not require the complex setup used in pressure-driven alignment processes and does not subject the soft hydrogel particles to the significant hydrodynamic forces that pressure-driven processes can introduce in microchannels. This capacity to address the position and orientation of individual particles provides a means for improving upon recently developed particle analysis methods. In particular, the fabrication of a magnetic aspiration column could be used to deliver all particles to a flow-through scanning chamber with the same probe-first orientation. As existing high-throughput flow alignment methods cannot control which end of the particle

leads in the flow [170], decoding algorithms that determine probe identity and amount of bound target must additionally ascertain the orientation of the particle for accurate analysis. This requires using one of the coding elements as an orientation marker. If all particles could be magnetically addressed to give the same orientation prior to entrance into the flow chamber, this would no longer be necessary and the coding capacity of these microparticles could be expanded by a factor of four. It should also be noted that the simultaneous reorientation and transportation of multiple barcoded particles was achieved in a large reservoir using a hand magnet (Fig. 5.6c). This capability could potentially be exploited for the ordered presentation of post-hybridization particles in a plate-based stationary scan. The magnetic functionality also introduces a new means by which the barcoded particles can be concentrated and subsequently separated from a carrier solution. In previous implementations of barcoded hydrogel particles for biomolecule detection, ten centrifugal separations were required for the rinsing steps in a typical assay. This density-based separation strategy tends to concentrate fibers and other particulate matter along with the encoded microparticles at the bottom of the sample tube. If these contaminants then stick to the particles, they can interfere with the analysis of the fluorescence emitted by the code and probe regions. Magnetic force separation provides an alternative approach to segregating the barcoded particles for rinsing procedures. Using a permanent magnet, we separated the particles on the side of a collection tube in 2 minutes (Fig. 5.6d).

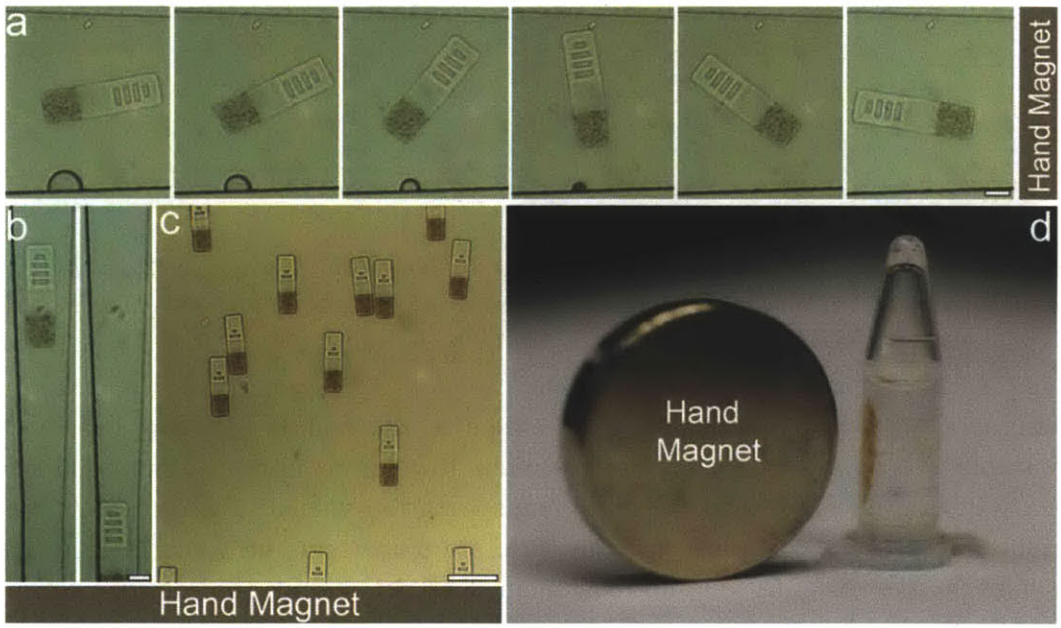

Figure 5.6: *Orientation, transportation, and separation of magnetic barcoded particles. (a) Reorientation of a magnetic barcoded particle in a microfluidic channel using a hand magnet. (b) Snapshots of magnetic transportation of a magnetic barcoded particle using a hand magnet. The particle was transported towards a narrow region in the microfluidic channel used for single-particle scanning analysis. (c) Image of reoriented magnetic barcoded particles moving towards a hand magnet. (d) Bulk separation of magnetic barcoded particles using a hand magnet. Scale bars are 50 μm (a and b), and 200 μm (c).*

In further experiments, the ten rinsing steps of a DNA hybridization assay were carried out using magnetic barcoded hydrogel microparticles and only magnetic separation steps. Upon analysis of the particles, it was determined that the vast majority of particles had been retained and, furthermore, a considerably smaller amount of particulate matter was seen in the carrier solution (Fig. 5.7).

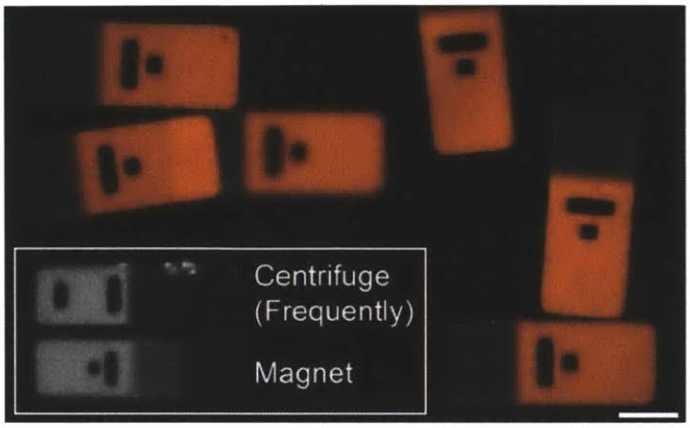

Figure 5.7: *Comparison between density-based separation strategy and magnetic force separation. Fluorescent images of the magnetic barcoded particles after the ten rinsing steps of a DNA hybridization assay were carried out. Insert image clearly shows that magnetic force separation can provide a considerably smaller amount of particulate matter in the carrier solution than the density-based separation strategy. The scale bar is 50 μm.*

5.1.5 Bioassays Using Magnetic Barcoded Particles

A wide variety of geometrically and chemically complex magnetic barcoded particles can be prepared by SFL using simple mask replacements and inlet fluid exchanges. Table 5.1 summarizes the four particle types used in a multiplexed DNA sensing study, illustrating the code, the identity of incorporated probe, and the presence or absence of magnetic beads in the tail region. Types 1, 2, and 3 featured a magnetic tail and were incorporated with no probe (type 1), probe #1 (type 2), or probe #2 (type 3) in the central region. Type 4 featured a non-magnetic tail, bore probe #1, and was used to investigate the effect of the added magnetic material on target detection. If the magnetic region is indeed inert with respect to target capture, the mean signals from the target panels on types 2 and 4 should be the same when incubated with target corresponding to probe #1.

Particle Type	Code	Probe	Magnetic Tail
1	2333	None	Yes
2	2003	Probe #1	Yes
3	0013	Probe #2	Yes
4	2013	Probe #1	No

Table 5.1 *Design of the four different magnetic barcoded particle types.*

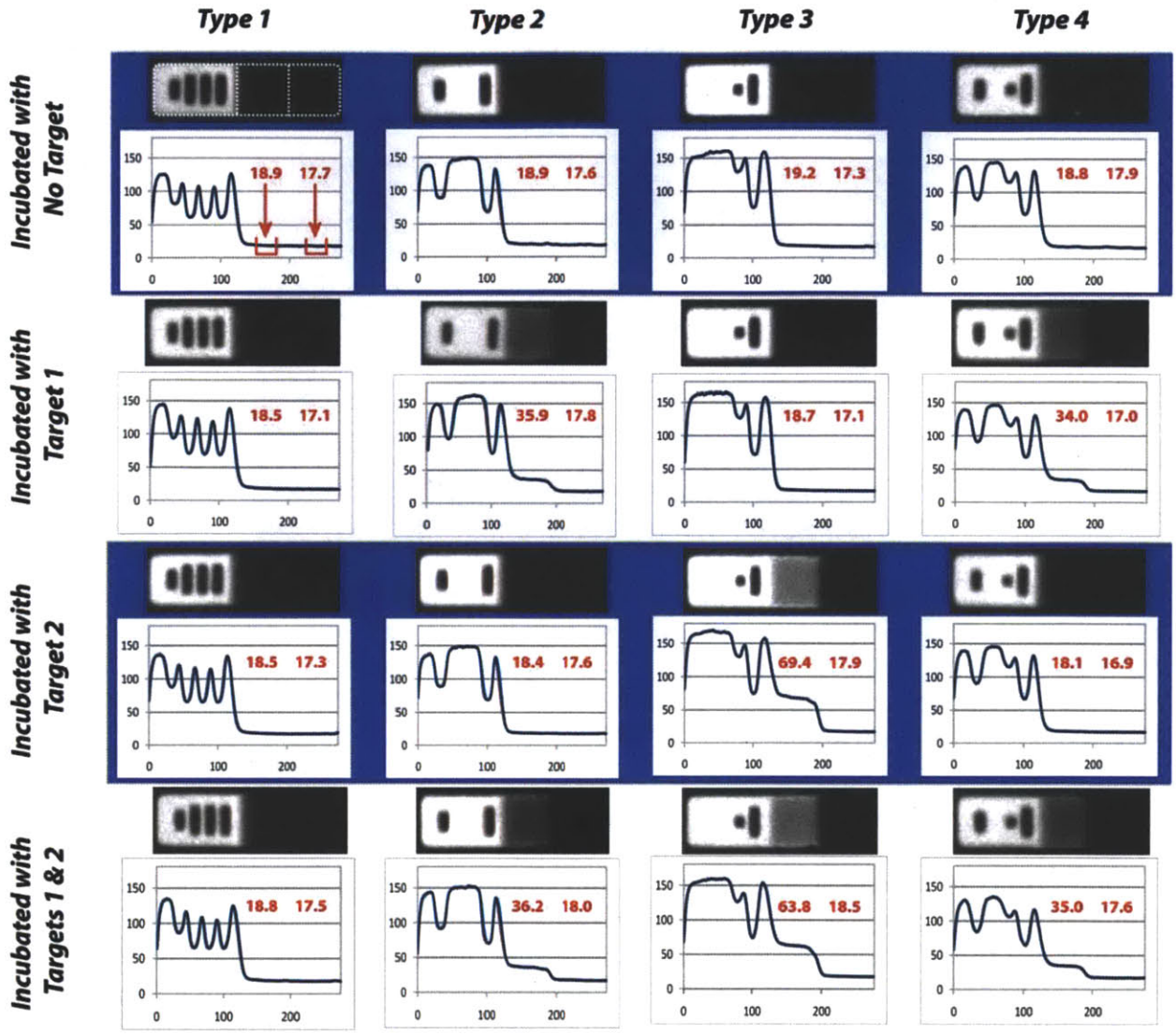

Figure 5.8: *Incubation matrix. Particles with a fluorescent code region, an internal probe region, and a tail region were synthesized and incubated with either 0 or 200 amol of two different biotinylated target oligonucleotides at 50 °C for 90 min. Following incubation, probe-target complexes were labeled with streptavidin-phycoerythrin (SAPE) at 21.5 °C for 45 min. Particle type 1 featured no probe, a magnetic tail, and code '2333'; type 2 featured probe 1, a magnetic tail, and code '2003'; type 3 featured probe 2, a magnetic tail, and code '0013'; type 4 featured probe 1, a non-magnetic tail, and code '2013.' Each plot shows the average of 5 scans of each particle type at the specified incubation condition. Horizontal axis is axial (lengthwise) position in pixels, and vertical axis is mean fluorescent intensity in arbitrary units. The mean signal across the width of the particle has been computed and plotted at each axial position. The red numbers above each scan indicate the mean fluorescent intensity measured in the probe region and in the tail region. The red bars in the first plot indicate the windows over which the averages were taken. Quoted numbers represent the mean of five separate scans.*

The four particle types were hybridized with either 0 or 200 amol of two different biotinylated target oligonucleotides. Following hybridization and labeling with SAPE, the fluorescent images of five particles of each type for each incubation condition were analyzed. An incubation matrix was prepared to compare the performance of the various particles (Fig. 5.8). Each plot in the matrix represents the average signal of 5 scans of each particle type at the specified incubation condition. The mean fluorescent intensity across the width of the particle (vertical axis, A.U.) was calculated and then plotted at each lengthwise position (horizontal axis, pixels) along the particle. The fluorescent intensities in the probe and tail regions were crucial to evaluating the success of the detection and examining the effect of the magnetic regions. As illustrated by a comparison of the results from types 2 and 4 in Figure 5.8, the mean signals in these regions are similar whether the tail region is magnetic or non-magnetic, indicating that the magnetic material does not interfere with the sensitive and specific detection of the oligonucleotides. It should be noted that target 1 generated a lower signal than target 2 when incubations were performed with all four types simultaneously in a single Eppendorf tube. The lower signal for target 1 can be attributed to the presence of two particle types (2 and 4) bearing probe 1 in the incubation mixture. Because of this redundancy, target 1 was spread over ~100 total particles per incubation, whereas target 2 was spread over only ~50 total particles per incubation.

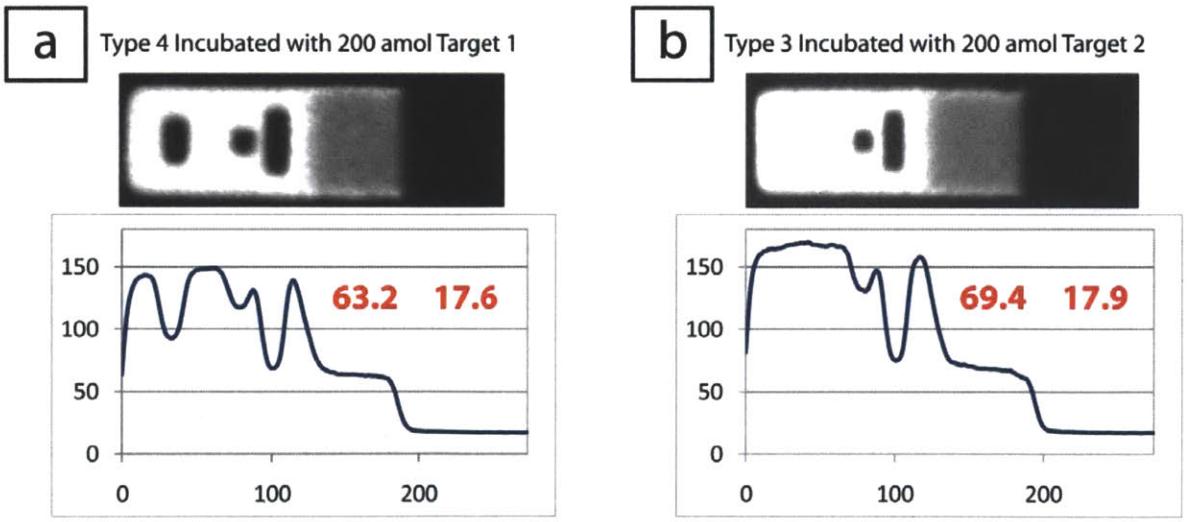

Figure 5.9: *Effect of Particle Density on Target Signal. Each plot shows the average of 5 scans of each particle type at the specified incubation condition. Data for (a) was taken from an incubation of ~50 particles of only type 4 with 200 amol of target 1. Data for (b) was taken from an incubation of ~50 particles of each of the four types with 200 amol of target 2. For the two cases, the total number of particles bearing probe complementary to the indicated target is roughly equal. The comparable signal intensities (63.2, 69.4 AU) in the probe regions indicate that the lower signals seen for types 2 and 4 in Figure 5.8 are in fact the result of spreading the available target among a greater number of particles. Horizontal axis is axial (lengthwise) position in pixels, and vertical axis is mean fluorescent intensity in arbitrary units. Mean signals for each of the regions are calculated as described in Figure 5.8.*

When the same amount of target 1 (200 amol) was incubated with ~50 particles of type 4 (probe 1, non-magnetic) alone, a signal (~63.2 AU) as high as that seen with the particles bearing probe 2 in the earlier assays was observed, thus confirming that the particle density led to the disparity in the original target levels (Fig. 5.9).

5.1.6 Summary

We have demonstrated that a modified form of SFL can be used to generate magnetic barcoded particles through the addition of a monomer stream containing superparamagnetic beads, as well as a perfusion rinse stream. The added magnetic region can acquire dipole moments in the presence of low-strength homogeneous magnetic fields, allowing the particles to align along the applied field direction. The magnetic barcoded particles have exhibited an enhanced range of functionality, providing novel means for orientation and separation during biological assays. The magnetic region has no apparent negative effects on the sensitive and specific multiplexed sensing of oligonucleotide targets. Although we have demonstrated the creation and use of relatively simple magnetic barcoded particles, the flow lithographic process for loading magnetic materials described here can perhaps be combined with more complex, multidimensional synthesis strategies such as lock release lithography (LRL) and hydrodynamic focusing lithography (HFL) to produce microparticles with additional novel properties advantageous for self-assembly and biomolecule detection studies.

5.2 Reinforced Barcoded Particles

Barcoded hydrogel particles have been used for detection of small biomarkers including DNAs, miRNAs, and low molecular weight (M.W.) proteins. For the case of large target biomolecules, barcoded particles should require more porous probe regions than before. We performed an experiment to check whether the adjustment of porosity for probe regions could control penetration of target molecules into gel networks. For the probe-target binding chemistry, we used the click chemistry of biotin- streptavidin as mentioned in section 3.5. Using the advanced flow lithography of HFL, we prepared 4 layered particles (Fig. 5.10). In the middle layer of the particles, the one region (A2) was comprised of biotin-PEGA 10% (v/v) and PEGDA 700 60% (v/v) while the other region (B) consisted of biotin-PEGA 10% (v/v) and PEGDA 700 10% (v/v). The particles were also bounded on the top and bottom by a blocking layer (A1). The blocking layers were inert without incorporating with biotin, and prevented diffusion of targets into the layers as they had porosity < ~ 1nm. After incubation, streptavidin (~ 5 nm) only diffused into the region of lower PEGDA concentration as shown in Figure 5.10. This validated that we should enlarge porosity of gel matrix to detect large biomolecules. Interestingly, the layered particles allowed us to visualize the degree of the protein diffusion as time passed. The time graph could be useful for extracting kinetic information such as the diffusivity of the proteins in the gel network.

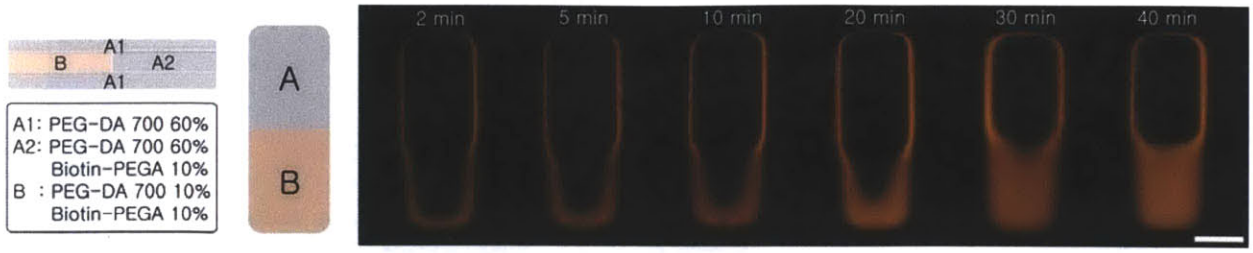

Figure 5.10: *Porosity control for diffusion of target molecules The schematic describes compositions of a 4 layered particle produced by HFL. After incubating the particles with streptavidin, the proteins did not combine with the biotins in A2 region of the particles due to size exclusion. The scale bar is 50 μm.*

Highly porous barcoded particles that are prepared by low concentration (< 10%) of PEGDA monomer can offer sensing capability to detect large targets. However, the pure soft barcoded particles cannot have been scanned in a microfluidic device, showing the mechanical instability that results in the bending or folding of the particles (Fig. 5.11a). To address this, we synthesized trilayered reinforced barcoded particles using HFL. In the particles, two soft porous layers were comprised of < 10% PEGDA while one hard supporting layer consisted of > 40% PEGDA. As shown in Figure 5.11b and c, the supporting middle layer prevented the distortion of soft top and bottom layers. Compared to the particle structure in Figure 5.10, this configuration for the layer arrangements is advantageous to maximize detection regions.

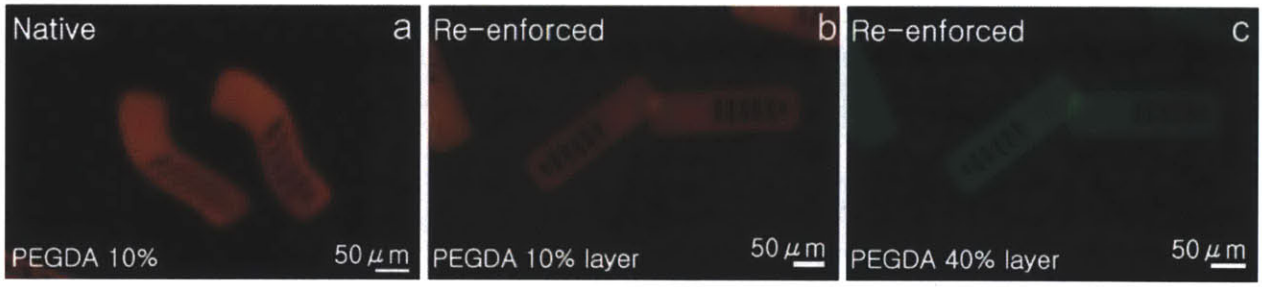

Figure 5.11: *Reinforced barcoded particles (a) Fluorescent image of soft PEG particles that were bent due to the mechanical instability. (b-c) Fluorescent images of reinforced barcoded particles. The sandwiched particles consisted of three layers: (1) two soft porous layers in the top and bottom of the particles (Red) and (2) a hard supporting layer in the middle of the particles (Green).*

Lastly, graphical code regions should be added on the above particles for practical applications. This has required dual-axis functionality of the particles. As shown in Figure 5.12, we successfully prepared those particles utilizing 5-layered flows in HFL. This new platform could expand the detection ranges of current barcoded particles to micron-sized targets such as viruses.

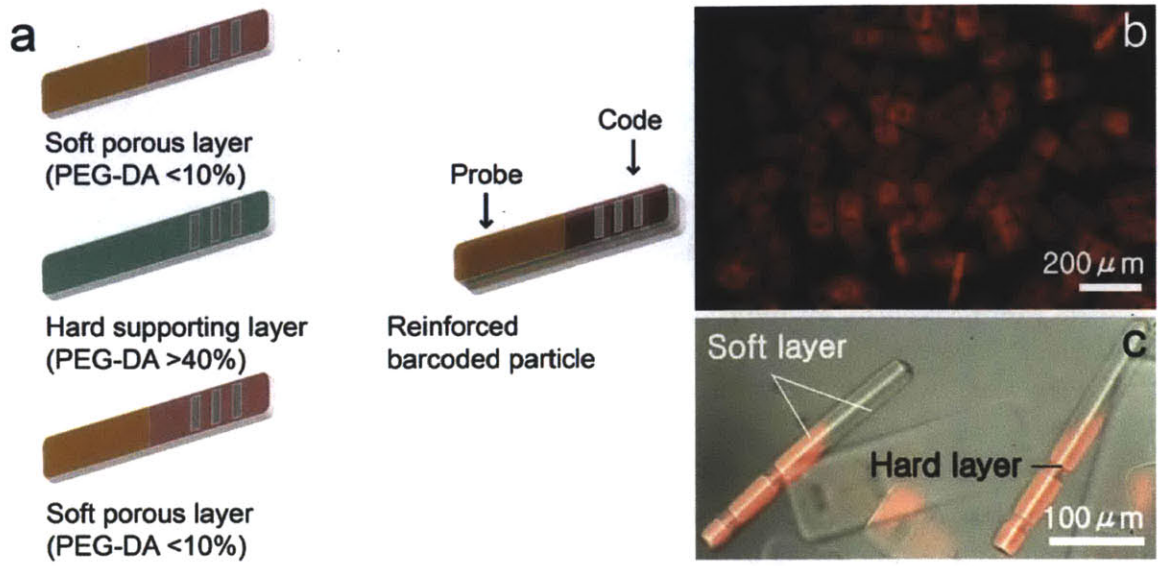

Figure 5.12: *Reinforced barcoded particles with 5 layered structures (a) A schematic description for the structures of a 5 layered barcoded particle. The center consisted of a PEGDA 40% monomer while the top and bottom comprised of side-by-side stacked PEGDA 10% monomers. Each top and bottom layer has two regions of code and probe. (b) Fluorescent microscopy image of the barcoded particles in (a). (c) Composite bright-field and fluorescent image of the barcoded particles in (b).*

5.3 Near-infrared Barcoded Particles

Although current barcoded particles have been extremely sensitive and working in high-throughput manner, the particles have required complex post-labeling steps. Also, the particles have not been used to examine dynamic information of probe-target binding events. Furthermore, target quantification has been achieved using the fluorescently labeled reporters which are excited by UV light. As a result, the particles are inappropriate for *in-vivo* multiplexed detection because the UV light has short penetration depth in tissue. Here, we introduce near-infrared barcoded particles to overcome these limitations.

5.3.1 Experimental Methods

Materials

In the synthesis of near-infrared barcoded particles, the code region was made of 10 % (v/v) PI, 40% (v/v) NOA81 (Norland Products), 30% (v/v) QDs solution and 20% (v/v) PEG-DA 700. The PEG probe region was made of 10 % (v/v) PI, 30 % (v/v) SWNT/PDDFs toluene solution, and 60% (v/v) PEG-DA 700. To disperse SWNT in toluene, a 5 mg portion of SWNT was added into 10 mL of toluene containing poly(9,9-dioctylfluorenyl)-2,7-diyl (PDDF, 100 mg). The resulting mixture was then sonicated using a probe-tip sonicator for 90 min at 10 W in an ice bath. The SWNT solution was centrifuged for 40 min at 16000 g, and then the supernatant was decanted for further experiments. Lastly, tergitol inert flows were tergitol NP-10 (Sigma Aldrich) containing 10% (v/v) PI.

Near infrared Fluorescence Spectrum Analysis

Near infrared fluorescence spectra of SWNTs from barcoded particles were measured using a home-built near infrared fluorescence microscope. Briefly, a Zeiss AxioVision inverted microscope was coupled to a Princeton Instruments InGaAs 1-D array detector through a PI-Acton SP150 spectrograph. Samples were excited by a 785 nm laser at 30 mW and the emission from 900 nm to 1400 nm was detected. Spectra were acquired for 2 sec using a 50x objective. For proton detection using a Janus particle, a particle was placed in the channel, which was mounted on the microscope stage. Then, a particle was focused using a 50x objective to maximize its near infrared fluorescence intensity. A diluted solution of HCl (70 μL, 7.2 M) was slowly added into the solution (140 μL) in the channel, and the near infrared fluorescence response to protons was measured in real-time for 10 min (785 nm laser, 2 sec of exposure time).

5.3.2 Synthesis of Near-infrared Barcoded Particles

We previously demonstrated that virtually any number of flows could be stacked increasing number of inlets entering from the top and bottom layers of the devices (Fig. 5.13a). To generate the structured flows shown in upper right corner of Figure 5.13b, inert flows are introduced in at both the top and second bottom channel while the monomers contained in the middle layer are combined at the first bottom inlet. In the 4-layered flows, we synthesized Janus triangular particles at the interface of the two flows in the middle layer. Each compartment of the particles was labeled using different fluorescent dyes to confirm the synthesis of Janus particles (Fig. 5.13c).

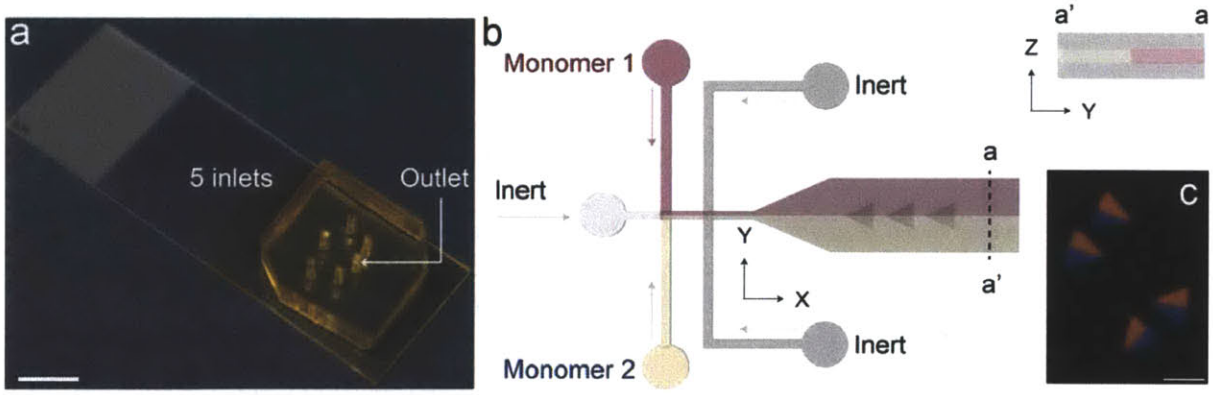

Figure 5.13: *Synthesis of Janus particles using structured microflows in a NOA 81 channel. (a) An optical image of a NOA81 device for Janus particle synthesis. In the first step, we prepared a two-layered NOA81 device with 5 inlets and 1 outlet. Using soft lithography, we could easily generate top and bottom NOA81 channels with geometries for the creation of 4 layered flows. To combine these two channels, we also used the iCVD nano-adhesive bonding method. (b) A schematic description for the generation of layered microflows which contain in their center side-by-side stacked monomers which are bounded on inert flows (c) A fluorescent image for Janus particles synthesized from this process. The scale bar is 50 μm.*

Using this process, we fabricated near-infrared barcoded particles embedded with QDs in the code region and SWNTs in the probe region (Fig. 5.14). The central stream corresponding to the code was the same composition as the QD monomer mixture in Section 4.6.2, except 20% (v/v) of toluene was replaced with PEG-DA 700 to promote gelation at the probe/code interface. The central stream corresponding to the probe was PEG-DA/PI containing 30% (v/v) SWNTs/toluene dispersion. Dispersing SWNTs in the PEG-DA/PI mixture presented a significant challenge due to the SWNTs tendency to aggregate in the meta-phase of the hydrophilic monomer and hydrophobic PI. Although SWNTs can be dispersed via covalent attachment of a polymer to their sidewall, this covalent functionalization disrupts the electronic structure and PL of the SWNT [171, 172]. Therefore, it is crucial to stably disperse SWNTs with polymers in a non-covalent manner in order to retain the properties that make them effective optical sensors [173]. To overcome these difficulties, we non-covalently dispersed SWNTs by hydrophobic poly(9,9-di-n-dodecylfluorenyl-2,7-diyl) polymer (PDDF) in toluene to preserve their sensing abilities. Then, we mixed the solution with PEG-DA/PI by vortexing for 30 s and dispersed SWNTs in the monomer mixture by toluene solvation. By sandwiching the two central streams between bounding tergitol flows, we were able to synthesize bifunctional barcoded particles.

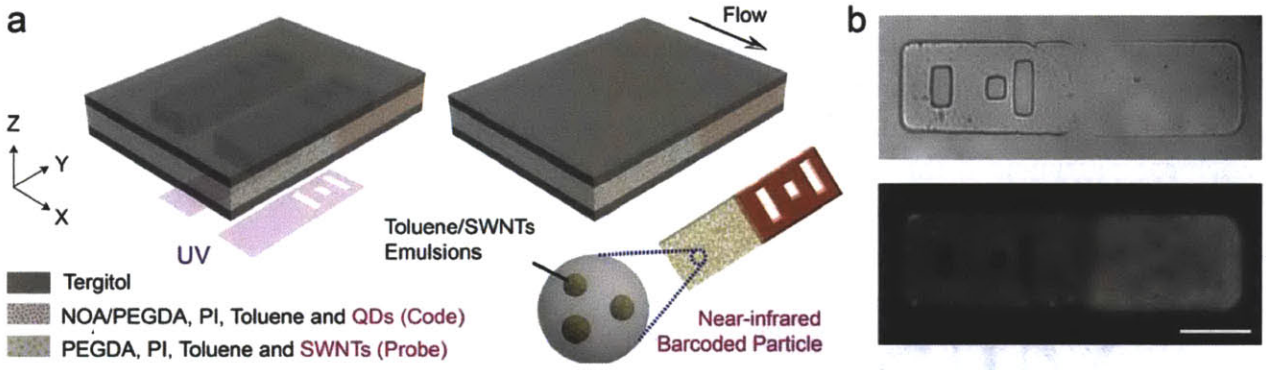

Figure 5.14: *Synthesis of near-infrared (NIR)-active barcoded particles (a) A schematic description for NIR-active multifunctional encoded particle synthesis. Using Tergitol for inert flows, Janus particles were created with a graphical barcode bearing near-infrared emitting QDs and a separate probe region embedded with single-walled nanotubes (SWNTs) for label-free and real-time detection. (b) DIC and near-infrared photoluminescence images of particles from (a). The scale bar is 50 μm.*

In near-infrared imaging of the particles, we observed the expected signal patterns from the '2013' graphical code region and the SWNT-embedded probe region (Fig. 5.14b). Importantly, the near-infrared fluorescence of barcoded particles was stable during long periods of laser excitation, a feature that is crucial for read-out of barcodes and accurate quantification of targets in real-time experiments.

5.3.3 Performance of Near-infrared Barcoded Particles

The SWNTs embedded within probe regions were able to detect a specific target in real-time, with label-free reporting of the binding events. Selectivity for a particular target was achieved by adjusting the wrapping of compounds around the SWNTs [173, 174]. This ability to tune selectivity suggests that this platform can be used for the multiplexed detection of several targets in a single assay. A distinct advantage of the SWNT probes used in these experiments is the possibility of label-free detection. When a SWNT encounters a target, the PL signal intensity of the SWNT is reduced and the emission wavelength shifts. This emission change allows for the detection and quantification of targets without complex post-target-capture labeling steps, thereby streamlining the assay process and eliminating the possibility of cross-reactivity between probes and labeling reagents. To illustrate the sensing capabilities of near-infrared fluorescence-barcoded particles, we performed simple proton detection through near-infrared fluorescence response. Before the introduction of protons, the spectrum of the probe region showed peaks generated from different types of SWNTs: (9,2), (11,3), (8,7) and (12,4). Among the four peak signals, we used the highest signal of (8,7) type for the analysis. Upon the introduction of 2.4 M HCl, the signal of (8,7) type was reduced to 26% of the original signal (Fig. 5.15a). We also extracted proton quenching kinetic information as the signal reduction was tracked in real time. We used an exponential quenching model to fit experimental data and found quenching kinetic parameters of $0.01s^{-1}$ and $0.02\ s^{-1}$ for 0.6 and 2.4 M target concentrations, respectively (Fig. 5.15b).

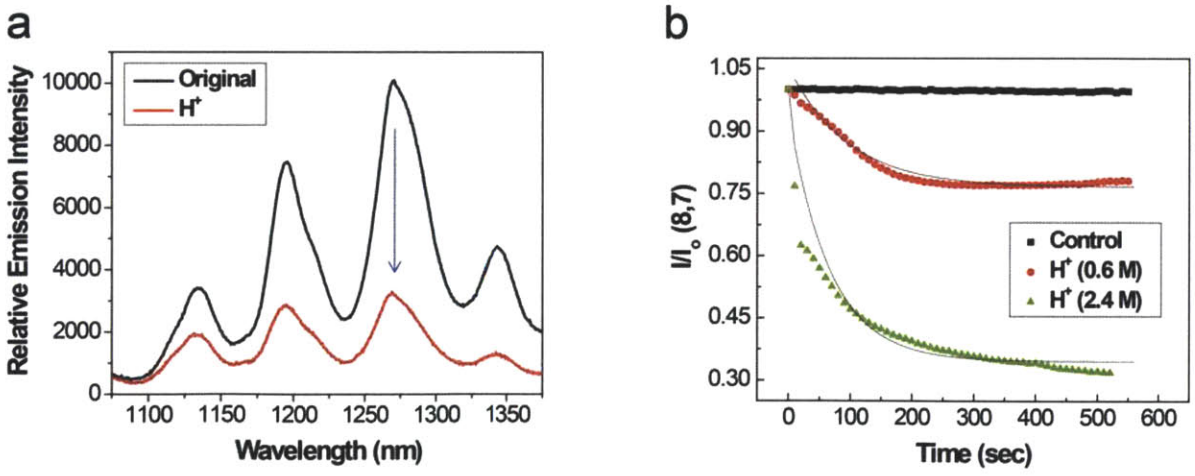

Figure 5.15: *Synthesis of near-infrared (NIR)-active barcoded particles (a) Shift in emission spectrum of embedded SWNTs upon introduction of 2.4 M HCl. Blue arrow indicates most pronounced shift, produced by (8,7)-type SWNT. (b) Intensity decay for (8,7)-type SWNT during H+ detection. Exponential quenching model was fit to the experimental data, providing moderate proton quenching kinetic parameters.*

5.3.4 Summary

We demonstrated the synthesis of near-infrared barcoded particles capable of label-free and real-time detection of analyte. As QDs and SWNTs were dispersed in toluene, the precursor solutions were organic phase which was not compatible with standard SFL process. As a result, we used the advanced flow lithography of oxygen-free FL in solvent-resistant NOA81 devices. Generating 4 layered microflows inside the devices, we synthesized Janus type barcoded particles that contained QDs in a code region and SWNTs in a separate probe region. Then, we performed a simple proton detection to check functions of the barcoded particles. In the experiments, we showed label-free detection via fluorescent signal shifts of embedded SWNTs. We also examined proton quenching kinetics utilizing the real-time detection abilities of SWNTs. Significantly, all functions of the barcoded particles work around the second near-infrared window ($\lambda \sim 1$ μm), which greatly reduces the likelihood of signal interference from tissues, cells, and biofluids in potential in-vivo multiplexed sensing applications.

Chapter 6

Outlook

In this thesis, we have improved the synthesis capabilities of FL and performance of barcoded particles. However, there are still needs to refine these techniques or develop more advanced methods and applications. For example, although LRL and HFL have greatly expanded the control over particle geometry and chemical patchiness, these techniques have not been used for clear applications, yet. In this section, we suggest future directions for advanced flow lithography and barcoded particles.

6.1 LRL and HFL

LRL can provide complex 2D chemical patterns in x-y dimension of particles while HFL can offer z-directional chemical patterns. The combination of these two techniques can allow for 3D chemical patterning in particles and yield new applications.

Future Direction

Previous studies have shown that 2D patterned films have transformed to 3D structures against diverse stimuli such as magnetic fields [175], heat [176-185], light [186-189], electrical voltage [190], and pH [13, 94, 191-196]. As shown in Figure 6.1a, various 3D structures have self-assembled from magnetically patterned 2D elastomeric sheets [175]. Also, the wrapping of a liquid droplet by a planar sheet has resulted in 3D structures whose variety and complexity are governed by number, order and orientation of folds (Fig. 6.1b)

[197]. Complex 3D structures have been further constructed by patterning mechanical properties onto 2D sheets of metal and polymer thin films (Fig. 6.1c) [198]. Recently, 2D patterned gel sheets were also transformed to 3D shapes by thermally induced buckling [184, 185].

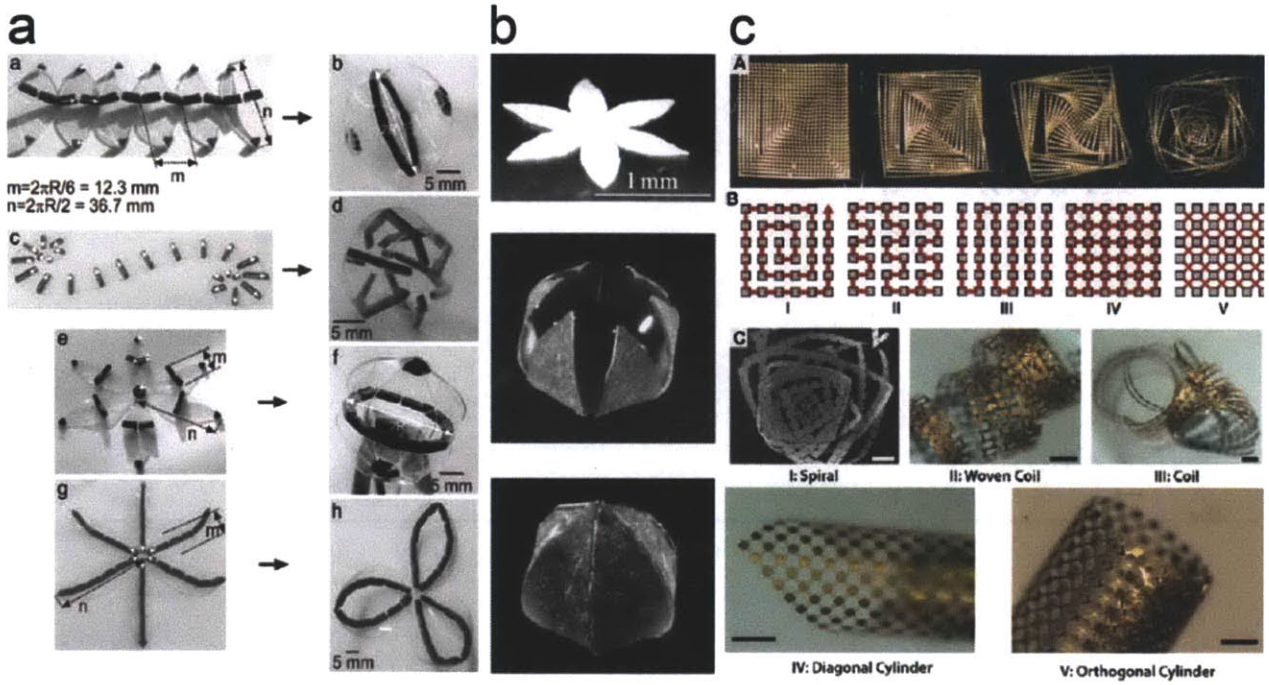

Figure 6.1: *3D folding of 2D patterned sheets (a) 3D structures self-assembled from magnetically patterned sheets. Images adapted from ref. 175. (b) 3D structures self-assembled from the interaction between elasticity and capillarity. Images adapted from ref. 197. (c) 3D structures self-assembled from 2D metal sheets with patterned mechanical properties. Images adapted from ref. 198. Scale bars are 250 μm (c).*

As LRL and HFL can spatially arrange multiple chemistries in all dimensions of particles, the techniques could be used for the design of smart particles to transform to elegant three-dimensional shapes. A simple example could be the synthesis of cross-shaped particles shown in Figure 6.2a. The particle contains magnetic materials (e.g. γ-Fe2O3) in six arms while the center consists of non-magnetic materials (e.g. PEG-DA). In the presence of an external magnetic field, the magnetic portions get induced dipole moments. Then, long-range dipolar interactions between the portions can induce columnar structures along the applied field direction [163]. Therefore, if the direction of the magnetic field is out of plane, the particle would be a 3D container as six arms stand up (Fig. 6.2a). When magnetic particles are patterned with heat responsive polymers such as PNIPAM (PolyN-isopropylacrylamide) [199] and HEMA (2-hydroxyethyl methacrylate) [200], the particles could experience a two-step stimuli induction process (Fig. 6.2b). First, these particles could be heated by irradiation with alternating electromagnetic fields [201, 202]. Then, the

induced hyperthermia could make the heat responsive polymers swelled, enlarging porosity of the polymers for drug release. These smart particles could be efficiently used for curing cancers because they can generate hyperthermia and drugs at the same time by a magnetic field. Particles with precisely positioned swelling/non-swelling chemistries would be also an interesting self-actuating material. A preliminary result for the proof-of-concept was made using the particle that has a cross-shaped rigid support and pH-responsive, fluorescent fins between each arm (Fig. 2.10c-e). Instead of displaying homogeneous swelling characteristics, these particles have shown anisotropic and reversible shape changing process. The pH-responsive particles could be useful for applications of microactuation [93, 203] and optics [204].

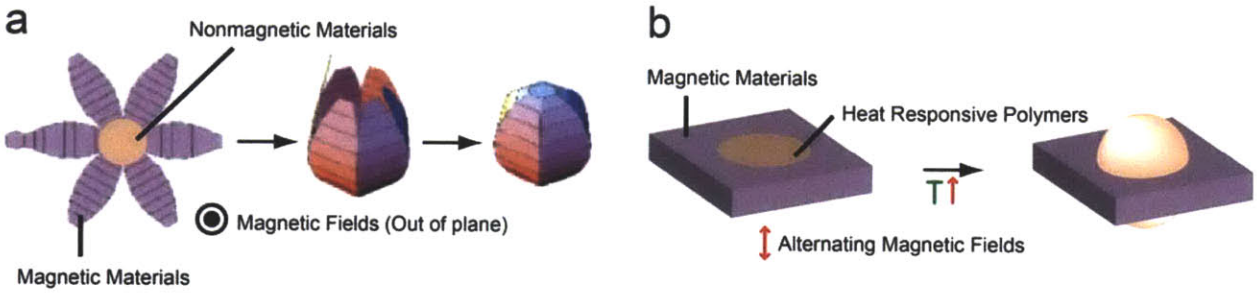

Figure 6.2: *Designs of smart particles (a) A scheme illustrating three stages for folding of a magnetic composite particle by magnetic fields. Image adapted from ref. 175. b. A schematic illustrating shape-changing process of a magnetic composite particle with heat responsive polymer.*

6.2 Solvent Compatible FL

We have synthesized particles from organic precursors using oxygen-free FL in solvent resistance NOA81 devices. However, the device fabrication process in oxygen-free FL is somewhat complex as the devices should be prepared as 3D channels for flow-stacking. On this reason, we have sought an alternative way to achieve solvent compatible FL without flow stacking process. If a device provides oxygen permeability as well as solvent resistance, we can do solvent-based particle synthesis using the prior oxygen lubrication layers.

Future Direction

Very recently, we have been attracted to a fluorinated elastomer called perfluoropolyether (PFPE). This material not only is commercially available (Product Name: SIFEL X71-8115) but also enables soft lithography. This product has two parts: (1) Part A that consists of a PFPE backbone capped with vinyl silicone and (2) Part B that consists of a PFPE backbone capped with silicon hydride. During soft lithography, the two parts are mixed in the ratio of 1 to 1 and cured by a hydrosilation reaction in the presence of platinum catalysts at 120 °C. The curing process is very similar to the PDMS curing process. The distinct merit of PFPE

is that the material has chemical resistances against organic solvents, acids, and alkali [205]. Before fabricating the PFPE devices, we designed an above simple experiment and checked whether the PFPE-silicone elastomer could provide oxygen lubrication layers for FL (Fig. 6.3). Typically, photocrosslinked PEGDA microparticles between glass slides were adhered onto the glass surfaces. Due to the oxygen impermeability of glass, the radical polymerization between glass slides was able to propagate to the glass surfaces without inhibition and thereby generated photo-patterned structures that were affixed to the surfaces. However, the photo-polymerized PEGDA structures between the PFPE layers were mobile just after UV exposure. This result implied that the oxygen permeability of PFPE elastomer could be high enough to create oxygen lubrication layers.

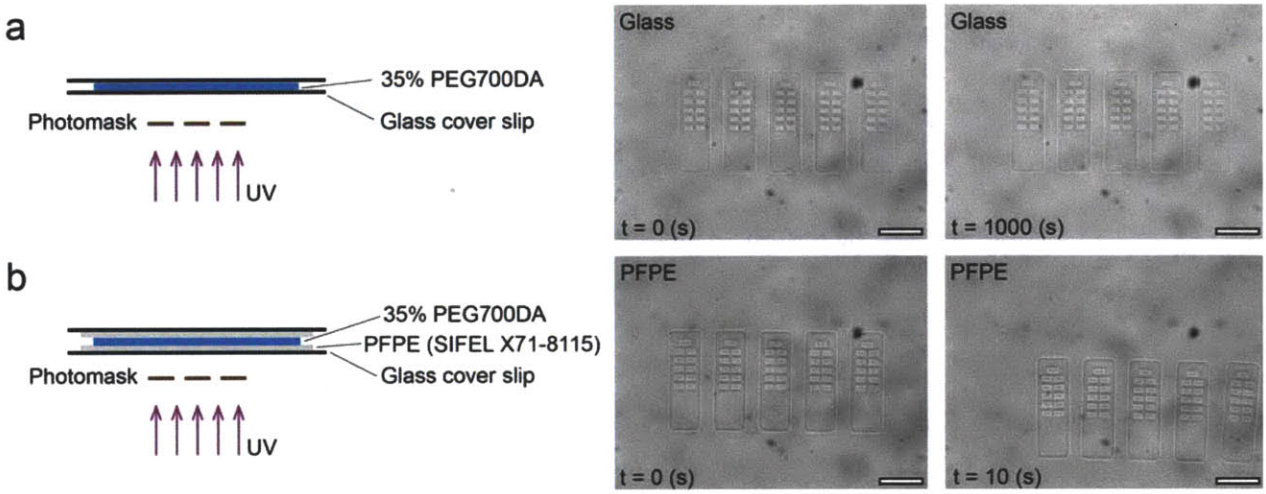

Figure 6.3: *Oxygen permeable perfluoropolyether (PFPE) (a) A schematic depicting a simple experiment to check the existence of oxygen lubrication layers. In the experiment, a droplet of PEGDA/PI was sandwiched between glass layers and polymerized by mask-defined UV light. Photopolymerized PEGDA structures between glass slides were immobile even after 1000 seconds. (b) The same experiment was performed for PFPE layers. Photo-polymerized PEGDA structures between the PFPE layers were mobile just after UV exposure. This validated that PFPE could provide oxygen lubrication layers. Scale bars are 100 μm.*

As multilayered microfluidic PFPE devices were fabricated by off-ratio bonding technique in a previous study, we prepared PFPE devices via the literature procedures [205]. Then, we used stop flow lithography to generate microparticles inside the devices. As expected, we found oxygen lubrication layers to allow for the fabrication of mobile particulates and synthesized homogeneous triangular particles as shown in Figure 6.4b. Also, we prepared PFPE devices with three inlets, and synthesized multifunctional barcoded particles on three phase laminar flows (Fig. 6.4c). These results demonstrated that PFPE devices could be used to synthesize particles in same throughput and spatial resolution as prior PDMS devices. To further evaluate the performance of PFPE devices for SFL process, we compared PFPE with PDMS from previous literatures. In Table 6.1, we summarized key properties of

both materials for SFL process. As the oxygen permeability and elastic modulus of PFPE are close to those of PDMS, PFPE devices can provide similar oxygen lubrication layers and channel response time to PDMS devices [206]. Also, PFPE has extremely low surface energy which is less than half of the PDMS surface energy, allowing for non-destructive SFL device construction [207, 208]. Furthermore, the fluorinated devices can minimize the monomer accumulation on surfaces, extending the SFL process time. In the long run of SFL process, PDMS devices has led to monomer accumulation at synthesis spot, eventually resulting in particles sticking to PDMS walls. Actually, we performed an experiment to determine process time at which particle sticking started for each device, and found that PFPE devices could offer about 2 times longer process time than PDMS devices.

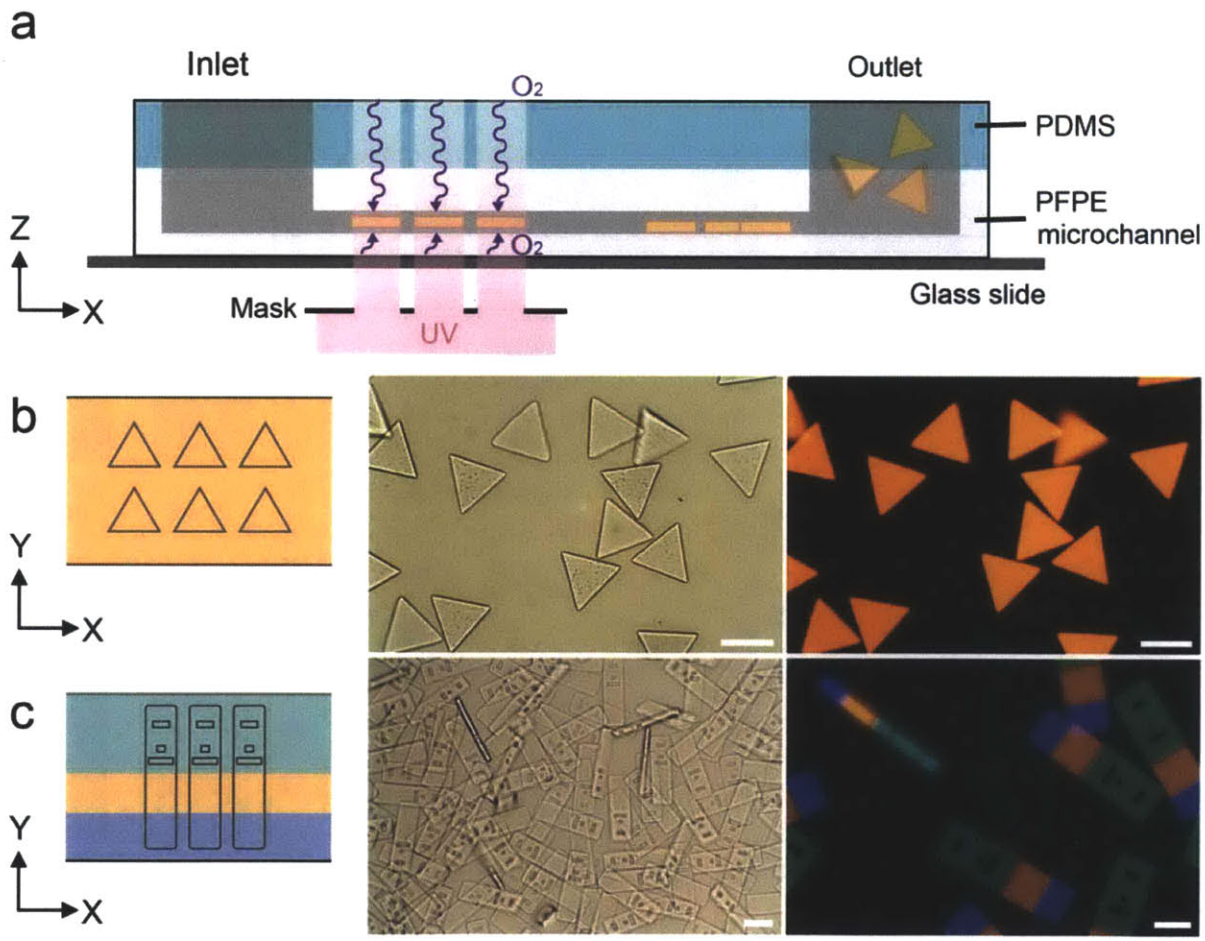

Figure 6.4: *SFL in a PFPE device (a) A schematic depicting the SFL process to synthesize triangular particles in a PFPE device. By virtue of oxygen lubrication layers, PFPE devices can allow for the production of free-floating particles. (b) The inserted schematic shows a top view of the process (a). Bright-field and fluorescent images show particles synthesized in (a). (c) Synthesis of multifunctional barcoded particles. A mask with an array of barcode particle shapes was aligned on three phase laminar flows that were created in a PFPE device with multiple inlets. Bright-field and fluorescent images show the barcoded particles with three distinct compartments. Scale bars are 100 μm (a) and 70 μm (b).*

Material	PDMS	PFPE
Oxygen Permeability (Barrers) [ref. 206]	550	400
Young's Modulus (MPa) [ref. 206]	2.4	3.9
Surface Energy (mN/m) [ref. 207]	25	12

Table 6.1: *Comparison of properties between PDMS and PFPE*

As mentioned before, PFPE devices can have similar SFL environments to PDMS devices. To demonstrate this, we synthesized cylindrical particles with high aspect ratio in both devices using same SFL process conditions. As particles were toppled by flows, we easily measured the width and height of particles for each device. In PDMS devices, the width of particles was 14.4 μm while the height of particles was 21.8 μm. In PFPE devices, the width of particles was 13.5 μm while the height of particles was 21.2 μm. Importantly, the differences of the particle dimensions between devices were only below 1 μm (Fig. 6.5). This result validate that PFPE devices can provide SFL environments akin to the PDMS devices.

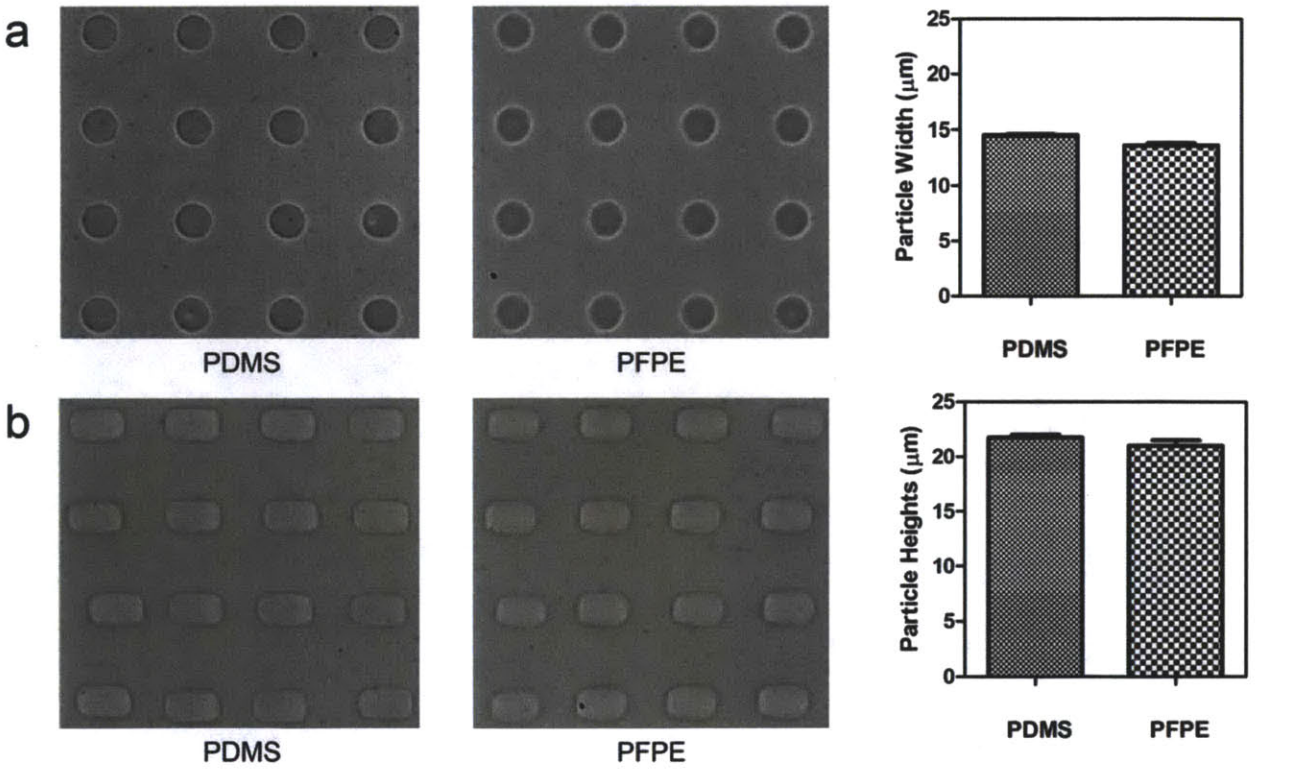

Figure 6.5: *Comparison of SFL performance between PDMS and PFPE devices (a) Top view of particles synthesized in both devices. The cylindrical particles were synthesized by SFL process using a mask with an array of 15 μm circles. For both devices, the diameters of sixteen particles were measured and plotted. The error bars indicate standard deviation. (b) Side view of particles. The particles were toppled by stable laminar flow in microfluidic devices. Like (a), the particle heights were measured and plotted with error bars.*

The most valuable feature of PFPE devices is that the devices have solvent resistances. In both PDMS and PFPE devices, we synthesized 300 μm long bar-shaped particles from water-insoluble monomers dissolved in toluene. The shape was chosen to investigate channel shape after swelling on the coordinate of channel width. In these experiments, the particles synthesized in PDMS devices were deformed reflecting swollen channel shape (Fig. 6.6a and b). On the other hand, the particles synthesized in PFPE devices were flat without shape distortion (Fig. 6.6e and f). We further quantified the fluorescent signals on the particle distance (Fig. 6.6c and g). The fluorescent signal of particles synthesized in PDMS devices was two times lower than the signal of particles synthesized in PFPE devices, validating that the former particles had thinner thickness than the latter particles. Also, the former particles had shown concave fluorescent signals which represented the deformed shapes of the particles. This result clearly demonstrated that PFPE devices could be used to synthesize anisotropic particles using organic solvents. However, solvent-based FL in PFPE devices could have some of drawbacks. First, the devices can be swollen as times goes by and unsuitable for long time synthesis. Also, the kinds of operable solvents in PFPE device have been limited. For these cases, we could use the previous oxygen-free FL [209].

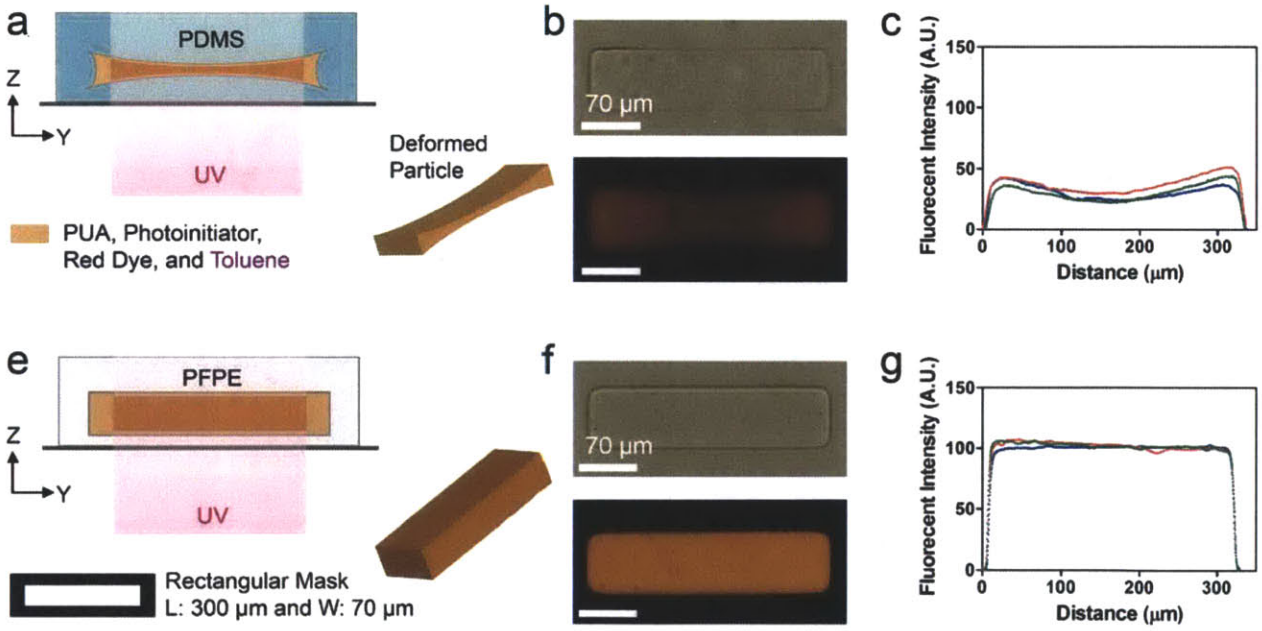

Figure 6.6: *Comparison of solvent-based SFL between PDMS and PFPE devices (a) A schematic depicting toluene-based SFL process in PDMS devices. The particles have curved shapes due to the swelling of the PDMS walls. The precursor consists of water insoluble monomer (polyurethane acrylate (PUA)), toluene, photoinitiator, and rhodamine acrylate. (b) Bright-field and fluorescent miscopy images of curved particles. (c) The fluorescent signals of three particles were quantitatively analyzed on particle distance using Image J software. (e) A schematic depicting toluene-based SFL process in PFPE devices. The particles have flat shapes due to toluene resistance of PFPE devices. (f) Bright-field and fluorescent images of flat particles. (g) Like (c), the fluorescent signals of three particles were analyzed on particle distance.*

6.3 Advanced Barcoded Particles

Although barcoded particles have been used for the detection of various biomolecules including DNAs, RNAs, Proteins, and viruses, the particles have not been used for living cell assays yet. For these assays, it would be important to incorporate ECM (extracellular matrix) with encoded particles.

Future Direction

To begin with, we suggest a fabrication way to prepare ECM microspheres encapsulating shape-coded particles. Usually, natural ECM such as collagen, alginate, and chitosan can be thermally or chemically cured [210-219]. Droplet based microfluidics have been successfully used to produce various ECM microspheres because the technique is compatible with various curing processes [220-223]. As a result, we propose to synchronize FL with drop-based microfluidics to create the suggested particles. Numerous works have been made in forming droplets by cross-flow shear method in T-junction microfluidic devices [158, 224-230]. However, any of these researches has not been performed with the stop flow system. We introduced the compressed-air flow control system [74] that could provide the rapid pulsing of microflows in order to synthesize particles in a stationary fluid for higher feature resolution and improved throughput.

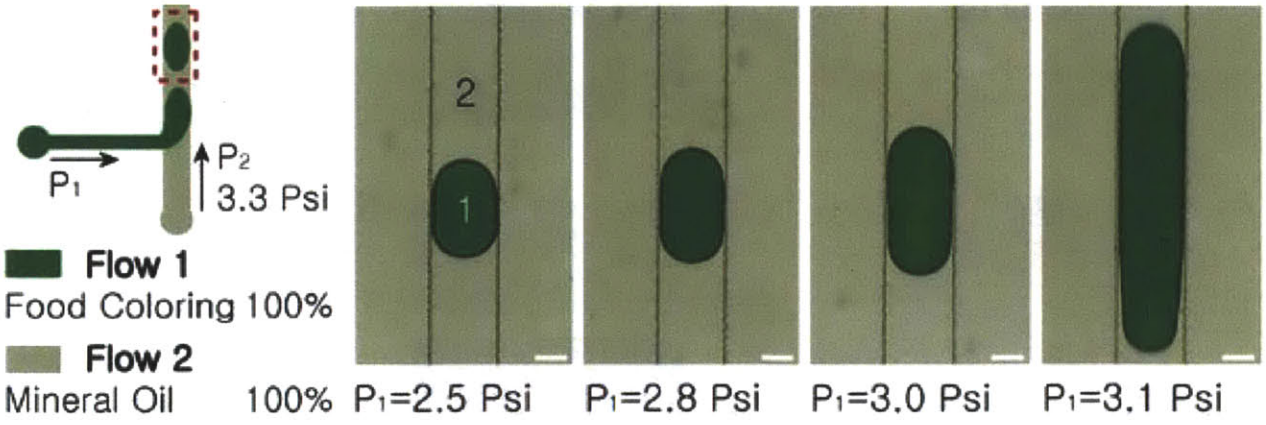

Figure 6.7: *Droplet size modulation using the compressed-air flow control system. Images taken downstream from a T-junction demonstrate the size range that can be achieved by simple adjustment of the dispersed phase driving pressure. All scale bars are 50 μm.*

The control system can be further utilized to produce monodisperse droplets with flow-focusing channels (Fig 6.7). Generally, in droplet-based microfluidics, syringe pumps have been used as a driving source to squeeze droplets into immiscible flows using channel geometry [231]. Our system can be implemented for this application for only 20% of the cost of the syringe approach. In addition, as syringes use a rotary motor to control volumetric

flow rates, the size variation of droplets can be substantial at low flow rates [231]. Our system exhibited high monodispersity at these reduced rates, and the rapid response of the pressure-driven setup was used to quickly change droplet size during experiments.

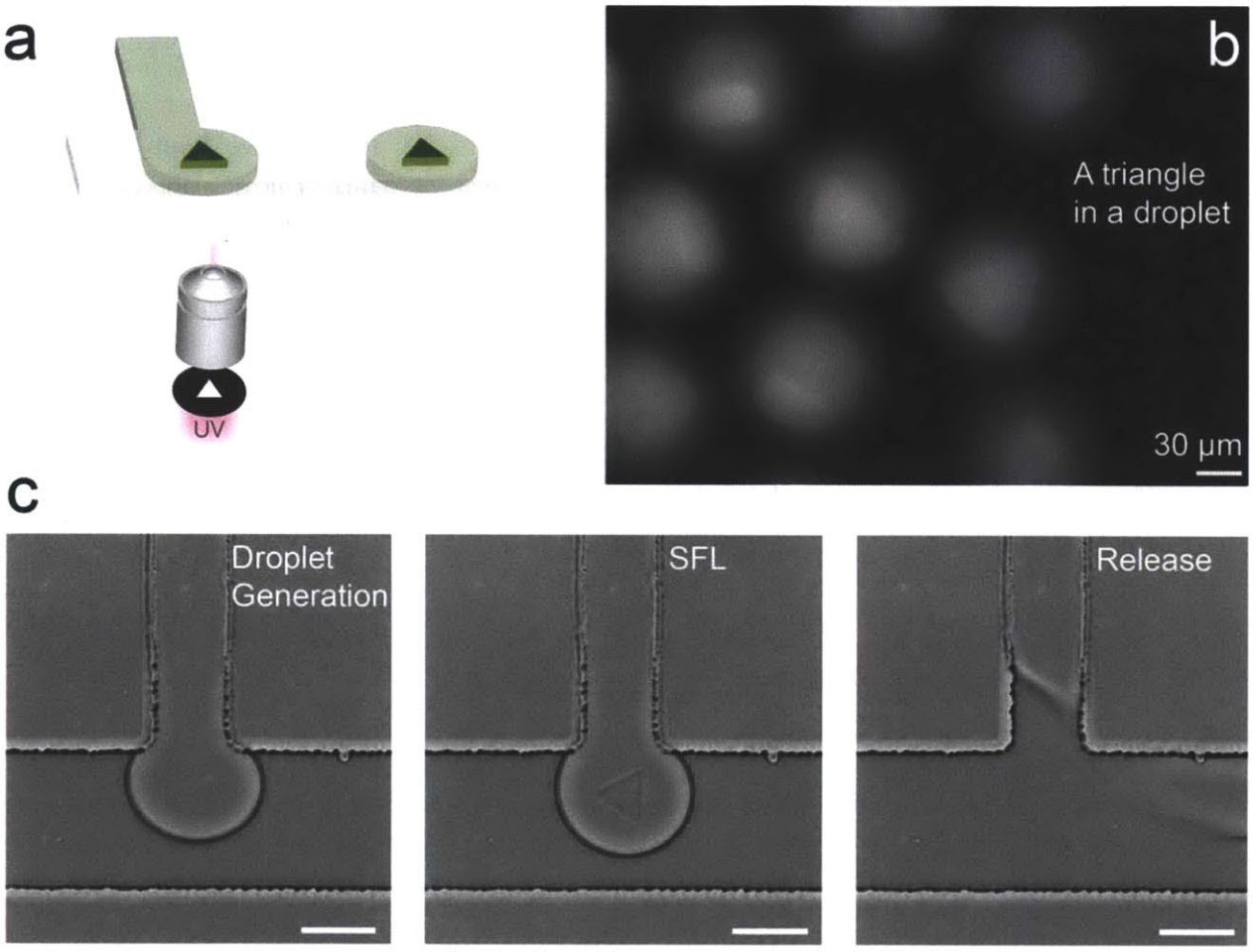

Figure 6.8: *Synchronization of SFL in droplet-based microfluidics (a) A schematic depicting the synchronization process. A droplet is stopped prior to SFL polymerization. Then, mask-defined particles are generated inside the droplet. After that, the droplet containing anisotropic particles is released by flows. (b) A fluorescent image of particles prepared by process (a). Each droplet contains a triangle particle inside. (c) Sequential DIC images to show the experimental process. Scale bars are 50 μm.*

Also, the system can instantly stop and start flow with milli-seconds resolution. On this time scale, we can easily control picoliter flow volume that is equivalent with a single droplet volume. In the squeezing regime, simple scaling analysis suggests that we could manipulate a single droplet when the flow time (t) is,

$$\frac{HWL_p}{Q_d} < t < \frac{2HWL_p}{Q_d} \quad , \quad \frac{L_p}{W} - \varepsilon = \omega \frac{Q_d}{Q_c}$$

Where Q_d is the volumetric flow rates of disperse phase, Q_c is the volumetric flow rates of continuous phase, H is the height of the main channel, W is the width of the main channel, ε and ω are the fitting parameters, and L_p is the length of a plug. The left term in the inequality is the time required for the generation of single droplet while the right term is the time required for the generation of double droplets. As long as we keep flow time between these two times, we can manipulate single droplet. Here, the attractive point is that we can synchronize this single droplet manipulation with shutter-mediated lithography and generate droplets containing anisotropic shaped particles with 100% accuracy. This schematic in Figure 6.8a describes how the process works. Using this process, we prepared droplets containing a triangle (Fig. 6.8b and c).

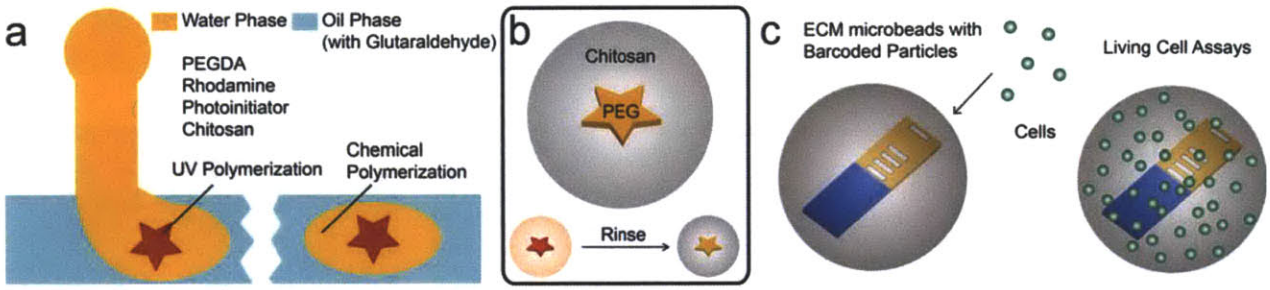

Figure 6.9: *Advanced barcoded particles for living cell assays (a) A schematic depicting the synthesis of extracellular matrix (ECM) microbeads encapsulating anisotropic particles. (b) A schematic showing the final product in process (a). (c) Living cell assays. During cell cultures on ECM microbeads, interior barcoded particles can be used to detect biomolecules secreted from living cells.*

Of particular interest, the use of two independent cross-linking mechanisms can allow us to create particles that have two different layers comprised of same phases. The synthesis of this type of particles has been challenging in emulsion techniques. In Figure 6.9a, we show the schematic description for the process. Using a disperse phase containing PEG-DA, chitosan (one of natural ECMs), photoinitiator, and rhodamine, we can generate anisotropic PEG particles inside a droplet by UV polymerization. Then, the outer chitosan shell can be chemically crosslinked by glutaraldehyde in the continuous phase. After that, unreacted PEG-DA, rhodamine and photoinitiator in the shell can be removed by rinsing the particles. The final product can be shown in Figure 6.9b. In this process, the encapsulated particles can be Janus type particles when two disperse phases are used. As a result, we could prepare the advanced barcoded particle shown in Figure 6.9c. As the outer shell of the particles consists of natural ECMs, we anticipate that cells would be favorably attached to the particles, and well-cultured. A recent study has shown that ECM microspheres can be used for an excellent scaffold for cell-cultures [223]. It is also important to note that cell

cultures on microspheres might be different with cell cultures in microwells as the spheres can provide scaffold similar to 3D environments. These particles could be novel platform for the multiplexed detection of biomolecules secreted from living cells.

Bibliography

[1] Lavan, D. A., Mcguire, T. and Langer, R., "Small-scale systems for in vivo drug delivery," *Nat. Biotech.* **21**, 1184-1191 (2003).

[2] Ehrbar, M., Schoenmakers, R., Christen, E. H., Fussenegger, M. and Weber, W., "Drug-sensing hydrogels for the inducible release of biopharmaceuticals," *Nat. Mater.* **7**, 800-804 (2008).

[3] He, H. Y., Cao, X. and Lee, L. J., "Design of a novel hydrogel-based intelligent system for controlled drug release," *J. Control Release* **95**, 391-402 (2004).

[4] Du, Y., Lo, E., Ali, S. and Khadernhosseini, A., "Directed assembly of cell-laden microgels for fabrication of 3D tissue constructs," *Proc. Natl. Acad. Sci. USA.* **105**, 9522-9527 (2008).

[5] Peppas, N. A., Hilt, J. Z., Khademhosseini, A. and Langer, R., "Hydrogels in biology and medicine: From molecular principles to bionanotechnology," *Adv. Mater.* **18**, 1345-1360 (2006).

[6] Koh, W. G., Itle, L. J. and Pishko, M. V., "Molding of hydrogel multiphenotype cell microstructures to create microarrays," *Anal. Chem.* **75**, 5783-5789 (2003).

[7] Pregibon, D. C., Toner, M. and Doyle, P. S., "Multifunctional encoded particles for high-throughput biomolecule analysis," *Science* **315**, 1393-1396 (2007).

[8] Katz, J. S., Doh, J. and Irvine, D. J., "Composition-tunable properties of amphiphilic comb copolymers containing protected methacrylic acid groups for multicomponent protein patterning," *Langmuir* **22**, 353-359 (2006).

[9] Hur, S. C., Choi, S. E., Kwon, S. and Di Carlo, D., "Inertial focusing of non-spherical microparticles," *Appl. Phys.* **99**, 044101 (2011).

[10] Randhawa, J. S., Keung, M. D., Tyagi, P. and Gracias, D. H., "Reversible Actuation of Microstructures by Surface-Chemical Modification of Thin-Film Bilayers," *Adv. Mater.* **22**, 407-410 (2010).

[11] Leong, T. G., Randall, C. L., Benson, B. R., Bassik, N., Stern, G. M. and Gracias, D. H., "Tetherless thermobiochemically actuated microgrippers," *Proc. Natl. Acad. Sci. USA* **106**, 703-708 (2009).

[12] Cho, J. H. and Gracias, D. H., "Self-Assembly of Lithographically Patterned Nanoparticles," *Nano Lett.* **9**, 4049-4052 (2009).

[13] Shim, T. S., Kim, S. H., Heo, C. J., Jeon, H. C. and Yang, S. M., "Controlled Origami Folding of Hydrogel Bilayers with Sustained Reversibility for Robust Microcarriers," *Angew. Chem. Int. Ed.* **51**, 1420-1423 (2012).

[14] Liu, Y., Boyles, J. K., Genzer, J. and Dickey, M. D., "Self-folding of polymer sheets using local light absorption," *Soft Matter* **8**, 1764-1769 (2012).

[15] Pandey, S., Ewing, M., Kunas, A., Nguyen, N., Gracias, D. H. and Menon, G., "Algorithmic design of self-folding polyhedra," *Proc. Natl. Acad. Sci. USA* **108**, 19885-19890 (2011).

[16] Vukusic, P. and Sambles, J. R., "Photonic structures in biology," *Nature* **424**, 852-855 (2003).

[17] Waits, C. M., Morgan, B., Kastantin, M. and Ghodssi, R., "Microfabrication of 3D silicon MEMS structures using gray-scale lithography and deep reactive ion etching," *Sensor. Actuat. a-Phys.* **119**, 245-253 (2005).

[18] Randhawa, J. S., Laflin, K. E., Seelam, N. and Gracias, D. H., "Microchemomechanical Systems," *Adv. Funct. Mater.* **21**, 2395-2410 (2011).

[19] Park, J. R., Choi, D. S., Gracias, D. H., Leong, T. G., Presser, N., Stupian, G. W., Leung, M. S. and Kim, Y. K., "Fabrication and characterization of RF nanoantenna on a nanoliter-scale 3D microcontainer," *Nanotechnology* **22**, (2011).

[20] Klug, A., "From Macromolecules to Biological Assemblies (Nobel Lecture)," *Angew. Chem. Int. Ed.* **22**, 565-582 (1983).

[21] Whitesides, G. M. and Grzybowski, B., "Self-assembly at all scales," *Science* **295**, 2418-2421 (2002).

[22] Glotzer, S. C. and Solomon, M. J., "Anisotropy of building blocks and their assembly into complex structures," *Nat. Mater.* **6**, 557-562 (2007).

[23] Kim, S. H., Lee, S. Y. and Yang, S. M., "Janus Microspheres for a Highly Flexible and Impregnable Water-Repelling Interface," *Angew. Chem. Int. Ed.* **49**, 2535-2538 (2010).

[24] Nisisako, T., Torii, T., Takahashi, T. and Takizawa, Y., "Synthesis of monodisperse bicolored janus particles with electrical anisotropy using a microfluidic co-flow system," *Adv. Mater.* **18**, 1152-1156 (2006).

[25] Yin, S. N., Wang, C. F., Yu, Z. Y., Wang, J., Liu, S. S. and Chen, S., "Versatile Bifunctional Magnetic-Fluorescent Responsive Janus Supraballs Towards the Flexible Bead Display," *Adv. Mater.* **23**, 2915-2919 (2011).

[26] Gangwal, S., Cayre, O. J. and Velev, O. D., "Dielectrophoretic Assembly of Metallodielectric Janus Particles in AC Electric Fields," *Langmuir* **24**, 13312-13320 (2008).

[27] Xing, H., Wang, Z. D., Xu, Z. D., Wong, N. Y., Xiang, Y., Liu, G. L. G. and Lu, Y., "DNA-Directed Assembly of Asymmetric Nanoclusters Using Janus Nanoparticles," *Acs Nano* **6**, 802-809 (2012).

[28] Rosenthal, G. and Klapp, S. H. L., "Ordering of amphiphilic Janus particles at planar walls: A density functional study," *J. Chem. Phys.* **134**, (2011).

[29] Smoukov, S. K., Gangwal, S., Marquez, M. and Velev, O. D., "Reconfigurable responsive structures assembled from magnetic Janus particles," *Soft Matter* **5**, 1285-1292 (2009).

[30] Yuet, K. P., Hwang, D. K., Haghgooie, R. and Doyle, P. S., "Multifunctional Superparamagnetic Janus Particles," *Langmuir* **26**, 4281-4287 (2010).

[31] Walther, A. and Muller, A. H. E., "Janus particles," *Soft Matter* **4**, 663-668 (2008).

[32] Howse, J. R., Jones, R. a. L., Ryan, A. J., Gough, T., Vafabakhsh, R. and Golestanian, R., "Self-motile colloidal particles: From directed propulsion to random walk," *Phys. Rev. Lett.* **99**, (2007).

[33] Golestanian, R., Liverpool, T. B. and Ajdari, A., "Propulsion of a molecular machine by asymmetric distribution of reaction products," *Phys. Rev. Lett.* **94**, (2005).

[34] Gracias, D. H., Tien, J., Breen, T. L., Hsu, C. and Whitesides, G. M., "Forming electrical networks in three dimensions by self-assembly," *Science* **289**, 1170-1172 (2000).

[35] Randhawa, J. S., Leong, T. G., Bassik, N., Benson, B. R., Jochmans, M. T. and Gracias, D. H., "Pick-and-Place Using Chemically Actuated Microgrippers," *J. Am. Chem. Soc.* **130**, 17238-17239 (2008).

[36] Ye, H. K., Randall, C. L., Leong, T. G., Slanac, D. A., Call, E. K. and Gracias, D. H., "Remote radio-frequency controlled nanoliter chemistry and chemical delivery on substrates," *Angew. Chem. Int. Ed.* **46**, 4991-4994 (2007).

[37] Leong, T. G., Randall, C. L., Benson, B. R., Zarafshar, A. M. and Gracias, D. H., "Self-loading lithographically structured microcontainers: 3D patterned, mobile microwells," *Lab Chip* **8**, 1621-1624 (2008).

[38] Randall, C. L., Kalinin, Y. V., Jamal, M., Shah, A. and Gracias, D. H., "Self-folding immunoprotective cell encapsulation devices," *Nanomed.-Nanotechnol. Biol. Med.* **7**, 686-689 (2011).

[39] Du, Y. A., Lo, E., Ali, S. and Khademhosseini, A., "Directed assembly of cell-laden microgels for fabrication of 3D tissue constructs," *Proc. Natl. Acad. Sci. USA* **105**, 9522-9527 (2008).

[40] Panda, P., Ali, S., Lo, E., Chung, B. G., Hatton, T. A., Khademhosseini, A. and Doyle, P. S., "Stop-flow lithography to generate cell-laden microgel particles," *Lab Chip* **8**, 1056-1061 (2008).

[41] Zuo, Y. C., Xiao, W. Q., Chen, X. Q., Tang, Y. J., Luo, H. R. and Fan, H. S., "Bottom-up approach to build osteon-like structure by cell-laden photocrosslinkable hydrogel," *Chem. Commun.* **48**, 3170-3172 (2012).

[42] Kawata, S., Sun, H. B., Tanaka, T. and Takada, K., "Finer features for functional microdevices - Micromachines can be created with higher resolution using two-photon absorption.," *Nature* **412**, 697-698 (2001).

[43] Kuebler, S. M., Braun, K. L., Zhou, W. H., Cammack, J. K., Yu, T. Y., Ober, C. K., Marder, S. R. and Perry, J. W., "Design and application of high-sensitivity two-photon initiators for three-dimensional microfabrication," *J. Photochem. Photobiol. a-Chem.* **158**, 163-170 (2003).

[44] Wu, S. H., Serbin, J. and Gu, M., "Two-photon polymerisation for three-dimensional micro-fabrication," *J. Photochem. Photobiol. a-Chem.* **181**, 1-11 (2006).

[45] Lafratta, C. N., Li, L. J. and Fourkas, J. T., "Soft-lithographic replication of 3D microstructures with closed loops," *Proc. Natl. Acad. Sci. USA* **103**, 8589-8594 (2006).

[46] Lafratta, C. N., Fourkas, J. T., Baldacchini, T. and Farrer, R. A., "Multiphoton fabrication," *Angew. Chem. Int. Ed.* **46**, 6238-6258 (2007).

[47] Tao, S. L., Popat, K. and Desai, T. A., "Off-wafer fabrication and surface modification of asymmetric 3D SU-8 microparticles," *Nat. Protoc.* **1**, 3153-3158 (2006).

[48] Hernandez, C. J. and Mason, T. G., "Colloidal alphabet soup: Monodisperse dispersions of shape-designed LithoParticles," *J. Phys. Chem. C* **111**, 4477-4480 (2007).

[49] Badaire, S., Cottin-Bizonne, C., Woody, J. W., Yang, A. and Stroock, A. D., "Shape selectivity in the assembly of lithographically designed colloidal particles," *J. Am. Chem. Soc.* **129**, 40-41 (2007).

[50] Khademhosseini, A., Yeh, J., Ling, Y. B., Karp, J. M., Gantz, J., Chandawarkar, A., Eng, G., Blumling, J. and Langer, R., "Micromolding of shape-controlled, harvestable cell-laden hydrogels," *Biomaterials* **27**, 5391-5398 (2006).

[51] Perry, J. L., Herlihy, K. P., Napier, M. E. and Desimone, J. M., "PRINT: A Novel Platform Toward Shape and Size Specific Nanoparticle Theranostics," *Accounts Chem. Res.* **44**, 990-998 (2011).

[52] Merkel, T. J., Herlihy, K. P., Nunes, J., Orgel, R. M., Rolland, J. P. and Desimone, J. M., "Scalable, Shape-Specific, Top-Down Fabrication Methods for the Synthesis of Engineered Colloidal Particles," *Langmuir* **26**, 13086-13096 (2010).

[53] Zhang, H., Nunes, J. K., Gratton, S. E. A., Herlihy, K. P., Pohlhaus, P. D. and Desimone, J. M., "Fabrication of multiphasic and regio-specifically functionalized PRINT (R) particles of controlled size and shape," *New J. Phys.* **11**, 075018 (2009).

[54] Jeong, U., Wang, Y. L., Ibisate, M. and Xia, Y. N., "Some new developments in the synthesis, functionalization, and utilization of monodisperse colloidal spheres," *Adv. Funct. Mater.* **15**, 1907-1921 (2005).

[55] Landfester, K., "Synthesis of colloidal particles in miniemulsions," *Ann. Rev. Mater. Res.* **36**, 231-279 (2006).

[56] Abou-Hassan, A., Sandre, O. and Cabuil, V., "Microfluidics in Inorganic Chemistry," *Angew. Chem. Int. Ed.* **49**, 6268-6286 (2010).

[57] Gunther, A., Il Park, J., Saffari, A., Kumar, S. and Kumacheva, E., "Microfluidic Synthesis of Polymer and Inorganic Particulate Materials," *Ann. Rev. Mater. Res.,* **40**, 415-443 (2010).

[58] Xu, S., Nie, Z., Seo, M., Lewis, P., Kumacheva, E., Stone, H. A., Garstecki, P., Weibel, D. B., Gitlin, I. and Whitesides, G. M., "Generation of monodisperse particles by using microfluidics: Control over size, shape, and composition," *Angew. Chem. Int. Ed.* **44**, 3799-3799 (2005).

[59] Teh, S. Y., Lin, R., Hung, L. H. and Lee, A. P., "Droplet microfluidics," *Lab Chip* **8**, 198-220 (2008).

[60] Utada, A. S., Lorenceau, E., Link, D. R., Kaplan, P. D., Stone, H. A. and Weitz, D. A., "Monodisperse double emulsions generated from a microcapillary device," *Science* **308**, 537-541 (2005).

[61] Il Park, J., Saffari, A., Kumar, S., Gunther, A. and Kumacheva, E., "Microfluidic Synthesis of Polymer and Inorganic Particulate Materials," *Ann. Rev. Mater. Res.,* **40**, 415-443 (2010).

[62] Millman, J. R., Bhatt, K. H., Prevo, B. G. and Velev, O. D., "Anisotropic particle synthesis in dielectrophoretically controlled microdroplet reactors," *Nat. Mater.* **4**, 98-102 (2005).

[63] Rastogi, V., Garcia, A. A., Marquez, M. and Velev, O. D., "Anisotropic Particle Synthesis Inside Droplet Templates on Superhydrophobic Surfaces," *Macromol. Rapid Commun.* **31**, 190-195 (2010).

[64] Roh, K. H., Martin, D. C. and Lahann, J., "Biphasic Janus particles with nanoscale anisotropy," *Nat. Mater.* **4**, 759-763 (2005).

[65] Bhaskar, S., Hitt, J., Chang, S. W. L. and Lahann, J., "Multicompartmental Microcylinders," *Angew. Chem. Int. Ed.* **48**, 4589-4593 (2009).

[66] Farokhzad, O. C., Rhee, M., Valencia, P. M., Rodriguez, M. I., Langer, R. and Karnik, R., "Synthesis of Size-Tunable Polymeric Nanoparticles Enabled by 3D Hydrodynamic Flow Focusing in Single-Layer Microchannels," *Adv. Mater.* **23**, H79-H83 (2011).

[67] Farokhzad, O. C., Karnik, R., Gu, F., Basto, P., Cannizzaro, C., Dean, L., Kyei-Manu, W. and Langer, R., "Microfluidic platform for controlled synthesis of polymeric nanoparticles," *Nano Lett.* **8**, 2906-2912 (2008).

[68] Jeon, N. L., Baskaran, H., Dertinger, S. K. W., Whitesides, G. M., Van De Water, L. and Toner, M., "Neutrophil chemotaxis in linear and complex gradients of interleukin-8 formed in a microfabricated device," *Nat. Biotech.* **20**, 826-830 (2002).

[69] Takayama, S., Mcdonald, J. C., Ostuni, E., Liang, M. N., Kenis, P. J. A., Ismagilov, R. F. and Whitesides, G. M., "Patterning cells and their environments using multiple laminar fluid flows in capillary networks," *Proc. Natl. Acad. Sci. USA* **96**, 5545-5548 (1999).

[70] Moore, J. S., Zhao, B. and Beebe, D. J., "Surface-directed liquid flow inside microchannels," *Science* **291**, 1023-1026 (2001).

[71] Hatch, A., Kamholz, A. E., Hawkins, K. R., Munson, M. S., Schilling, E. A., Weigl, B. H. and Yager, P., "A rapid diffusion immunoassay in a T-sensor," *Nat. Biotech.* **19**, 461-465 (2001).

[72] Dendukuri, D., Pregibon, D. C., Collins, J., Hatton, T. A. and Doyle, P. S., "Continuous-flow lithography for high-throughput microparticle synthesis," *Nat. Mater.* **5**, 365-369 (2006).

[73] Dendukuri, D., Gu, S. S., Pregibon, D. C., Hatton, T. A. and Doyle, P. S., "Stop-flow lithography in a microfluidic device," *Lab Chip* **7**, 818-828 (2007).

[74] Bong, K. W., Chapin, S. C., Pregibon, D. C., Baah, D., Floyd-Smith, T. M. and Doyle, P. S., "Compressed-air flow control system," *Lab Chip* **11**, 743-747 (2011).

[75] Dendukuri, D., Panda, P., Haghgooie, R., Kim, J. M., Hatton, T. A. and Doyle, P. S., "Modeling of Oxygen-Inhibited Free Radical Photopolymerization in a PDMS Microfluidic Device," *Macromolecules* **41**, 8547-8556 (2008).

[76] Lee, H., Kim, J., Kim, H., Kim, J. and Kwon, S., "Colour-barcoded magnetic microparticles for multiplexed bioassays," *Nat. Mater.* **9**, 745-749 (2010).

[77] Pregibon, D. C. and Doyle, P. S., "Optimization of Encoded Hydrogel Particles for Nucleic Acid Quantification," *Anal. Chem.* **81**, 4873-4881 (2009).

[78] Chapin, S. C., Appleyard, D. C., Pregibon, D. C. and Doyle, P. S., "Rapid microRNA Profiling on Encoded Gel Microparticles," *Angew. Chem. Int. Ed.* **50**, 2289-2293 (2011).

[79] Chapin, S. C. and Doyle, P. S., "Ultrasensitive Multiplexed MicroRNA Quantification on Encoded Gel Microparticles Using Rolling Circle Amplification," *Anal. Chem.* **83**, 7179-7185 (2011).

[80] Appleyard, D. C., Chapin, S. C. and Doyle, P. S., "Multiplexed Protein Quantification with Barcoded Hydrogel Microparticles," *Anal. Chem.* **83**, 193-199 (2011).

[81] Appleyard, D. C., Chapin, S. C., Srinivas, R. L. and Doyle, P. S., "Bar-coded hydrogel microparticles for protein detection: synthesis, assay and scanning," *Nat. Protoc.* **6**, 1761-1774 (2011).

[82] Srinivas, R. L., Chapin, S. C. and Doyle, P. S., "Aptamer-Functionalized Microgel Particles for Protein Detection," *Anal. Chem.* **83**, 9138-9145 (2011).

[83] Tan, W. S., Lewis, C. L., Horelik, N. E., Pregibon, D. C., Doyle, P. S. and Yi, H. M., "Hierarchical Assembly of Viral Nanotemplates with Encoded Microparticles via Nucleic Acid Hybridization," *Langmuir* **24**, 12483-12488 (2008).

[84] Chung, S. E., Park, W., Shin, S., Lee, S. A. and Kwon, S., "Guided and fluidic self-assembly of microstructures using railed microfluidic channels," *Nat. Mater.* **7**, 581-587 (2008).

[85] Hwang, D. K., Oakey, J., Toner, M., Arthur, J. A., Anseth, K. S., Lee, S., Zeiger, A., Van Vliet, K. J. and Doyle, P. S., "Stop-Flow Lithography for the Production of Shape-Evolving Degradable Microgel Particles," *J. Am. Chem. Soc.* **131**, 4499-4504 (2009).

[86] Haghgooie, R., Toner, M. and Doyle, P. S., "Squishy Non-Spherical Hydrogel Microparticles," *Macromol. Rapid Commun.* **31**, 128-134 (2010).

[87] Helgeson, M. E., Moran, S., An, H. and Doyle, P. S., "Mesoporous organohydrogels from thermogelling photocrosslinkable nanoemulsions," *Nat. Mater.* DOI:10.1038/nmat3248 (2012).

[88] An, H., Helgeson, M. E. and Doyle, P. S., "Nanoemulsion Composite Microgels for Orthogonal Encapsulation and Release," *Adv. Mater.* DOI:10.1002/adma.201200214 (2012).

[89] Shepherd, R. F., Panda, P., Bao, Z., Sandhage, K. H., Hatton, T. A., Lewis, J. A. and Doyle, P. S., "Stop-Flow Lithography of Colloidal, Glass, and Silicon Microcomponents," *Adv. Mater.* **20**, 4734-4739 (2008).

[90] Kim, J., Chung, S. E., Choi, S. E., Lee, H., Kim, J. and Kwon, S., "Programming magnetic anisotropy in polymeric microactuators," *Nat. Mater.* **10**, 747-752 (2011).

[91] Dendukuri, D., Hatton, T. A. and Doyle, P. S., "Synthesis and self-assembly of amphiphilic polymeric microparticles," *Langmuir* **23**, 4669-4674 (2007).

[92] Kim, H., Ge, J., Kim, J., Choi, S., Lee, H., Lee, H., Park, W., Yin, Y. and Kwon, S., "Structural colour printing using a magnetically tunable and lithographically fixable photonic crystal," *Nat. Photonics* **3**, 534-540 (2009).

[93] Beebe, D. J., Moore, J. S., Bauer, J. M., Yu, Q., Liu, R. H., Devadoss, C. and Jo, B. H., "Functional hydrogel structures for autonomous flow control inside microfluidic channels," *Nature* **404**, 588-590 (2000).

[94] Kaehr, B. and Shear, J. B., "Multiphoton fabrication of chemically responsive protein hydrogels for microactuation," *Proc. Natl. Acad. Sci. USA* **105**, 8850-8854 (2008).

[95] Rolland, J. P., Maynor, B. W., Euliss, L. E., Exner, A. E., Denison, G. M. and Desimone, J. M., "Direct fabrication and harvesting of monodisperse, shape-specific nanobiomaterials," *J. Am. Chem. Soc.* **127**, 10096-10100 (2005).

[96] Sung, K. E., Vanapalli, S. A., Mukhija, D., Mckay, H. A., Millunchick, J. M., Burns, M. A. and Solomon, M. J., "Programmable fluidic production of microparticles with configurable anisotropy," *J. Am. Chem. Soc.* **130**, 1335-1340 (2008).

[97] Jang, J. H., Ullal, C. K., Kooi, S. E., Koh, C. and Thomas, E. L., "Shape control of multivalent 3D colloidal particles via interference lithography," *Nano Lett.* **7**, 647-651 (2007).

[98] Cheung, Y. K., Gillette, B. M., Zhong, M., Ramcharan, S. and Sia, S. K., "Direct patterning of composite biocompatible microstructures using microfluidics," *Lab Chip* **7**, 574-579 (2007).

[99] Gervais, T., El-Ali, J., Gunther, A. and Jensen, K. F., "Flow-induced deformation of shallow microfluidic channels," *Lab Chip* **6**, 500-507 (2006).

[100] Hoffman, J. M., Shao, J., Hsu, C. H. and Folch, A., "Elastomeric Molds with tunable microtopography," *Adv. Mater.* **16**, 2201-2206 (2004).

[101] Unger, M. A., Chou, H. P., Thorsen, T., Scherer, A. and Quake, S. R., "Monolithic microfabricated valves and pumps by multilayer soft lithography," *Science* **288**, 113-116 (2000).

[102] Jang, J. H., Dendukuri, D., Hatton, T. A., Thomas, E. L. and Doyle, P. S., "A route to three-dimensional structures in a microfluidic device: Stop-flow interference lithography," *Angew. Chem. Int. Ed.* **46**, 9027-9031 (2007).

[103] Chung, S. E., Park, W., Park, H., Yu, K., Park, N. and Kwon, S., "Optofluidic maskless lithography system for real-time synthesis of photopolymerized microstructures in microfluidic channels," *Appl. Phys. Lett.* **91**, 041106 (2007).

[104] Mellott, M. B., Searcy, K. and Pishko, M. V., "Release of protein from highly cross-linked hydrogels of poly(ethylene glycol) diacrylate fabricated by UV polymerization," *Biomaterials* **22**, 929-941 (2001).

[105] Kane, R. S., "Fabricating complex polymeric micro- and nanostructures: Lithography in microfluidic devices," *Angew. Chem. Int. Ed.* **47**, 1368-1370 (2008).

[106] Geng, Y., Dalhaimer, P., Cai, S. S., Tsai, R., Tewari, M., Minko, T. and Discher, D. E., "Shape effects of filaments versus spherical particles in flow and drug delivery," *Nat. Nanotech.* **2**, 249-255 (2007).

[107] Champion, J. A. and Mitragotri, S., "Role of target geometry in phagocytosis," *Proc. Natl. Acad. Sci. USA* **103**, 4930-4934 (2006).

[108] Gratton, S. E. A., Ropp, P. A., Pohlhaus, P. D., Luft, J. C., Madden, V. J., Napier, M. E. and Desimone, J. M., "The effect of particle design on cellular internalization pathways," *Proc. Natl. Acad. Sci. USA* **105**, 11613-11618 (2008).

[109] Bong, K. W., Pregibon, D. C. and Doyle, P. S., "Lock release lithography for 3D and composite microparticles," *Lab Chip* **9**, 863-866 (2009).

[110] Simonnet, C. and Groisman, A., "High-throughput and high-resolution flow cytometry in molded microfluidic devices," *Anal. Chem.* **78**, 5653-5663 (2006).

[111] Chang, C. C., Huang, Z. X. and Yang, R. J., "Three-dimensional hydrodynamic focusing in two-layer polydimethylsiloxane (PDMS) microchannels," *J. Micromech. Microeng.* **17**, 1479-1486 (2007).

[112] Choi, S. J., Yoo, P. J., Baek, S. J., Kim, T. W. and Lee, H. H., "An ultraviolet-curable mold for sub-100-nm lithography," *J. Am. Chem. Soc.* **126**, 7744-7745 (2004).

[113] Simonnet, C. and Groisman, A., "Two-dimensional hydrodynamic focusing in a simple microfluidic device," *Appl. Phys. Lett.* **87**, 114104 (2005).

[114] Ozaydin-Ince, G. and Gleason, K. K., "Transition between kinetic and mass transfer regimes in the initiated chemical vapor deposition from ethylene glycol diacrylate," *J. Vac. Sci. Technol. A* **27**, 1135-1143 (2009).

[115] Xu, J. J. and Gleason, K. K., "Conformal, Amine-Functionalized Thin Films by Initiated Chemical Vapor Deposition (iCVD) for Hydrolytically Stable Microfluidic Devices," *Chem. Mater.* **22**, 1732-1738 (2010).

[116] Mao, Y. and Gleason, K. K., "Hot filament chemical vapor deposition of poly(glycidyl methacrylate) thin films using tert-butyl peroxide as an initiator," *Langmuir* **20**, 2484-2488 (2004).

[117] Lau, K. K. S. and Gleason, K. K., "Particle surface design using an all-dry encapsulation method," *Adv. Mater.* **18**, 1972-1977 (2006).

[118] Im, S. G., Bong, K. W., Lee, C. H., Doyle, P. S. and Gleason, K. K., "A conformal nano-adhesive via initiated chemical vapor deposition for microfluidic devices," *Lab Chip* **9**, 411-416 (2009).

[119] Bartolo, D., Degre, G., Nghe, P. and Studer, V., "Microfluidic stickers," *Lab Chip* **8**, 274-279 (2008).

[120] Carlborg, C. F., Haraldsson, T., Oberg, K., Malkoch, M. and Van Der Wijngaart, W., "Beyond PDMS: off-stoichiometry thiol-ene (OSTE) based soft lithography for rapid prototyping of microfluidic devices," *Lab Chip* **11**, 3136-3147 (2011).

[121] Sollier, E., Murray, C., Maoddi, P. and Di Carlo, D., "Rapid prototyping polymers for microfluidic devices and high pressure injections," *Lab Chip* **11**, 3752-3765 (2011).

[122] Futterer, C., Minc, N., Bormuth, V., Codarbox, J. H., Laval, P., Rossier, J. and Viovy, J. L., "Injection and flow control system for microchannels," *Lab Chip* **4**, 351-356 (2004).

[123] Yoon, S. K., Mitchell, M., Choban, E. R. and Kenis, P. J. A., "Gravity-induced reorientation of the interface between two liquids of different densities flowing laminarly through a microchannel," *Lab Chip* **5**, 1259-1263 (2005).

[124] Suh, S. K., Bong, K. W., Hatton, T. A. and Doyle, P. S., "Using Stop-Flow Lithography To Produce Opaque Microparticles: Synthesis and Modeling," *Langmuir* **27**, 13813-13819 (2011).

[125] Bong, K. W., Bong, K. T., Pregibon, D. C. and Doyle, P. S., "Hydrodynamic Focusing Lithography," *Angew. Chem. Int. Ed.* **49**, 87-90 (2010).

[126] Lee, G. B., Chang, C. C., Huang, S. B. and Yang, R. J., "The hydrodynamic focusing effect inside rectangular microchannels," *J. Micromech. Microeng.* **16**, 1024-1032 (2006).

[127] Deen, W. M. Analysis of Transport Phenomena, Oxford University Press, New York, 1st edn. (1998).

[128] Ismagilov, R. F., Stroock, A. D., Kenis, P. J. A., Stone, H. A. and Whitesides, G., "Experimental and theoretical scaling laws for transverse diffusive broadening in two-phase laminar flows in microchannels," *Appl. Phys. Lett.* **76**, 2376-2378 (2000).

[129] Shao, J. H. and Baltus, R. E., "Hindered diffusion of dextran and polyethylene glycol in porous membranes," *Aiche J.* **46**, 1149-1156 (2000).

[130] O'neal, D. P., Meledeo, M. A., Davis, J. R., Ibey, B. L., Gant, V. A., Pishko, M. V. and Cote, G. L., "Oxygen sensor based on the fluorescence quenching of a ruthenium complex immobilized in a biocompatible poly(ethylene glycol) hydrogel," *IEEE Sens. J.* **4**, 728-734 (2004).

[131] Park, J., Hong, W. and Kim, C. S., "Color Intensity Method for Hydrogel Oxygen Sensor Array," *IEEE Sens. J.* **10**, 1855-1862 (2010).

[132] R, W. and V, N., "Shedding light onto live molecular targets.," *Nat. Med.* **9**, 123-128 (2003).

[133] Welsher, K., Sherlock, S. P. and Dai, H. J., "Deep-tissue anatomical imaging of mice using carbon nanotube fluorophores in the second near-infrared window," *Proc. Natl. Acad. Sci. USA* **108**, 8943-8948 (2011).

[134] Murray, C. B., Norris, D. J. and Bawendi, M. G., "Synthesis and Characterization of Nearly Monodisperse Cde (E = S, Se, Te) Semiconductor Nanocrystallites," *J. Am. Chem. Soc.* **115**, 8706-8715 (1993).

[135] Shim, T. S., Kim, S. H., Sim, J. Y., Lim, J. M. and Yang, S. M., "Dynamic Modulation of Photonic Bandgaps in Crystalline Colloidal Arrays Under Electric Field," *Adv. Mater.* **22**, 4494-4498 (2010).

[136] Lee, D., Cohen, R. E. and Rubner, M. F., "Antibacterial properties of Ag nanoparticle loaded multilayers and formation of magnetically directed antibacterial microparticles," *Langmuir* **21**, 9651-9659 (2005).

[137] Lee, D., Cohen, R. E. and Rubner, M. F., "Heterostructured magnetic nanotubes," *Langmuir* **23**, 123-129 (2007).

[138] Voltairas, P. A., Fotiadis, D. I. and Michalis, L. K., "Hydrodynamics of magnetic drug targeting," *J. Biomech.* **35**, 813-821 (2002).

[139] Doyle, P. S., Bibette, J., Bancaud, A. and Viovy, J. L., "Self-assembled magnetic matrices for DNA separation chips," *Science* **295**, 2237-2237 (2002).

[140] Helseth, L. E., Muruganathan, R. M., Zhang, Y. and Fischer, T. M., "Colloidal rings in a liquid mixture," *Langmuir* **21**, 7271-7275 (2005).

[141] Helseth, L. E., "Self-assembly of colloidal pyramids in magnetic fields," *Langmuir* **21**, 7276-7279 (2005).

[142] Kim, H., Ge, J. P., Kim, J., Choi, S., Lee, H., Lee, H., Park, W., Yin, Y. and Kwon, S., "Structural colour printing using a magnetically tunable and lithographically fixable photonic crystal," *Nat. Photonics* **3**, 534-540 (2009).

[143] Hoehn, M., Kustermann, E., Blunk, J., Wiedermann, D., Trapp, T., Wecker, S., Focking, M., Arnold, H., Hescheler, J., Fleischmann, B. K., Schwindt, W. and Buhrle, C., "Monitoring of implanted stem cell migration in vivo: A highly resolved in vivo magnetic resonance imaging investigation of experimental stroke in rat," *Proc. Natl. Acad. Sci. USA* **99**, 16267-16272 (2002).

[144] Berensmeier, S., "Magnetic particles for the separation and purification of nucleic acids," *Appl. Microbiol. Biotech.* **73**, 495-504 (2006).

[145] Peyman, S. A., Iles, A. and Pamme, N., "Mobile magnetic particles as solid-supports for rapid surface-based bioanalysis in continuous flow," *Lab Chip* **9**, 3110-3117 (2009).

[146] Hayes, M. A., Polson, N. A., Phayre, A. N. and Garcia, A. A., "Flow-based microimmunoassay," *Anal. Chem.* **73**, 5896-5902 (2001).

[147] Choi, J. W., Oh, K. W., Thomas, J. H., Heineman, W. R., Halsall, H. B., Nevin, J. H., Helmicki, A. J., Henderson, H. T. and Ahn, C. H., "An integrated microfluidic biochemical detection system for protein analysis with magnetic bead-based sampling capabilities," *Lab Chip* **2**, 27-30 (2002).

[148] Gijs, M. a. M., Lacharme, F. and Lehmann, U., "Microfluidic Applications of Magnetic Particles for Biological Analysis and Catalysis," *Chem. Rev.* **110**, 1518-1563 (2009).

[149] Rida, A. and Gijs, M. a. M., "Dynamics of magnetically retained supraparticle structures in a liquid flow," *Appl. Phys. Lett.* **85**, 4986-4988 (2004).

[150] Biswal, S. L. and Gast, A. P., "Micromixing with linked chains of paramagnetic particles," *Anal. Chem.* **76**, 6448-6455 (2004).

[151] Rida, A. and Gijs, M. a. M., "Manipulation of self-assembled structures of magnetic beads for microfluidic mixing and assaying," *Anal. Chem.* **76**, 6239-6246 (2004).

[152] Lee, C. S., Lee, H. and Westervelt, R. M., "Microelectromagnets for the control of magnetic nanoparticles," *Appl. Phys. Lett.* **79**, 3308-3310 (2001).

[153] Deng, T., Whitesides, G. M., Radhakrishnan, M., Zabow, G. and Prentiss, M., "Manipulation of magnetic microbeads in suspension using micromagnetic systems fabricated with soft lithography," *Appl. Phys. Lett.* **78**, 1775-1777 (2001).

[154] Ostergaard, S., Blankenstein, G., Dirac, H. and Leistiko, O., "A novel approach to the automation of clinical chemistry by controlled manipulation of magnetic particles," *J. Magn. Magn. Mater.* **194**, 156-162 (1999).

[155] Pamme, N. and Manz, A., "On-chip free-flow magnetophoresis: Continuous flow separation of magnetic particles and agglomerates," *Anal. Chem.* **76**, 7250-7256 (2004).

[156] Pamme, N., "Magnetism and microfluidics," *Lab Chip* **6**, 24-38 (2006).

[157] Pamme, N., "Continuous flow separations in microfluidic devices," *Lab Chip* **7**, 1644-1659 (2007).

[158] Zhang, K., Liang, Q. L., Ma, S., Mu, X. A., Hu, P., Wang, Y. M. and Luo, G. A., "On-chip manipulation of continuous picoliter-volume superparamagnetic droplets using a magnetic force," *Lab Chip* **9**, 2992-2999 (2009).

[159] Lou, X. H., Qian, J. R., Xiao, Y., Viel, L., Gerdon, A. E., Lagally, E. T., Atzberger, P., Tarasow, T. M., Heeger, A. J. and Soh, H. T., "Micromagnetic selection of aptamers in microfluidic channels," *Proc. Natl. Acad. Sci. USA* **106**, 2989-2994 (2009).

[160] Adams, J. D., Kim, U. and Soh, H. T., "Multitarget magnetic activated cell sorter," *Proc. Natl. Acad. Sci. USA* **105**, 18165-18170 (2008).

[161] Yuan, Q. C. and Williams, R. A., "Large scale manufacture of magnetic polymer particles using membranes and microfluidic devices," *China Particuology* **5**, 26-42 (2007).

[162] Vladisavljevic, G. T. and Williams, R. A., "Recent developments in manufacturing emulsions and particulate products using membranes," *Adv. Colloid Interfac.* **113**, 1-20 (2005).

[163] Hwang, D. K., Dendukuri, D. and Doyle, P. S., "Microfluidic-based synthesis of non-spherical magnetic hydrogel microparticles," *Lab Chip* **8**, 1640-1647 (2008).

[164] Chen, C. H., Abate, A. R., Lee, D. Y., Terentjev, E. M. and Weitz, D. A., "Microfluidic Assembly of Magnetic Hydrogel Particles with Uniformly Anisotropic Structure," *Adv. Mater.* **21**, 3201-3204 (2009).

[165] Yuet, K. P., Hwang, D. K., Haghgooie, R. and Doyle, P. S., "Multifunctional Superparamagnetic Janus Particles," *Langmuir* **26**, 4281-4287 (2009).

[166] Wilson, R., Cossins, A. R. and Spiller, D. G., "Encoded microcarriers for high-throughput multiplexed detection," *Angew. Chem. Int. Ed.* **45**, 6104-6117 (2006).

[167] Birtwell, S. and Morgan, H., "Microparticle encoding technologies for high-throughput multiplexed suspension assays," *Integr. Biol.* 1, 345-362 (2009).

[168] Kellar, K. L. and Douglass, J. P., "Multiplexed microsphere-based flow cytometric immunoassays for human cytokines," *J. Immunol. Methods* **279**, 277-285 (2003).

[169] Zhao, Y. J., Zhao, X. W., Hu, J., Xu, M., Zhao, W. J., Sun, L. G., Zhu, C., Xu, H. and Gu, Z. Z., "Encoded Porous Beads for Label-Free Multiplex Detection of Tumor Markers," *Adv. Mater.* **21**, 569-572 (2009).

[170] Chapin, S. C., Pregibon, D. C. and Doyle, P. S., "High-throughput flow alignment of barcoded hydrogel microparticles," *Lab Chip* **9**, 3100-3109 (2009).

[171] Dyke, C. A., Usrey, M. L., Barone, P. W., Allen, M. J., Shan, H. W., Kittrell, C., Hauge, R. H., Tour, J. M., Smalley, R. E. and Strano, M. S., "Electronic structure control of single-walled carbon nanotube functionalization," *Science* **301**, 1519-1522 (2003).

[172] Usrey, M. L., Lippmann, E. S. and Strano, M. S., "Evidence for a two-step mechanism in electronically selective single-walled carbon nanotube reactions," *J. Am. Chem. Soc.* **127**, 16129-16135 (2005).

[173] Kim, J. H., Heller, D. A., Jin, H., Barone, P. W., Song, C., Zhang, J., Trudel, L. J., Wogan, G. N., Tannenbaum, S. R. and Strano, M. S., "The rational design of nitric oxide selectivity in single-walled carbon nanotube near-infrared fluorescence sensors for biological detection," *Nat. Chem.* **1**, 473-481 (2009).

[174] Zhang, J. Q., Boghossian, A. A., Barone, P. W., Rwei, A., Kim, J. H., Lin, D. H., Heller, D. A., Hilmer, A. J., Nair, N., Reuel, N. F. and Strano, M. S., "Single Molecule Detection of Nitric Oxide Enabled by d(AT)(15) DNA Adsorbed to Near Infrared Fluorescent Single-Walled Carbon Nanotubes," *J. Am. Chem. Soc.* **133**, 567-581 (2011).

[175] Boncheva, M., Andreev, S. A., Mahadevan, L., Winkleman, A., Reichman, D. R., Prentiss, M. G., Whitesides, S. and Whitesides, G. M., "Magnetic self-assembly of three-dimensional surfaces from planar sheets," *Proc. Natl. Acad. Sci. USA* **102**, 3924-3929 (2005).

[176] Hu, Z. B., Zhang, X. M. and Li, Y., "Synthesis and Application of Modulated Polymer Gels," *Science* **269**, 525-527 (1995).

[177] Behl, M., Razzaq, M. Y. and Lendlein, A., "Multifunctional Shape-Memory Polymers," *Adv. Mater.* **22**, 3388-3410 (2010).

[178] Simpson, B., Nunnery, G., Tannenbaum, R. and Kalaitzidou, K., "Capture/release ability of thermo-responsive polymer particles," *J. Mater. Chem.* **20**, 3496-3501 (2010).

[179] Stoychev, G., Puretskiy, N. and Ionov, L., "Self-folding all-polymer thermoresponsive microcapsules," *Soft Matter* **7**, 3277-3279 (2011).

[180] Azam, A., Laflin, K. E., Jamal, M., Fernandes, R. and Gracias, D. H., "Self-folding micropatterned polymeric containers," *Biomed. Microdevices* **13**, 51-58 (2011).

[181] Kalaitzidou, K. and Crosby, A. J., "Adaptive polymer particles," *Appl. Phys. Lett.* **93**, 041910 (2008).

[182] Zakharchenko, S., Puretskiy, N., Stoychev, G., Stamm, M. and Ionov, L., "Temperature controlled encapsulation and release using partially biodegradable thermo-magneto-sensitive self-rolling tubes," *Soft Matter* **6**, 2633-2636 (2010).

[183] Leong, T. G., Benson, B. R., Call, E. K. and Gracias, D. H., "Thin Film Stress Driven Self-Folding of Microstructured Containers," *Small* **4**, 1605-1609 (2008).

[184] Klein, Y., Efrati, E. and Sharon, E., "Shaping of elastic sheets by prescription of non-Euclidean metrics," *Science* **315**, 1116-1120 (2007).

[185] Kim, J., Hanna, J. A., Byun, M., Santangelo, C. D. and Hayward, R. C., "Designing Responsive Buckled Surfaces by Halftone Gel Lithography," *Science* **335**, 1201-1205 (2012).

[186] Camacho-Lopez, M., Finkelmann, H., Palffy-Muhoray, P. and Shelley, M., "Fast liquid-crystal elastomer swims into the dark," *Nat. Mater.* **3**, 307-310 (2004).

[187] Lendlein, A., Jiang, H. Y., Junger, O. and Langer, R., "Light-induced shape-memory polymers," *Nature* **434**, 879-882 (2005).

[188] Ikeda, T., Nakano, M., Yu, Y. L., Tsutsumi, O. and Kanazawa, A., "Anisotropic bending and unbending behavior of azobenzene liquid-crystalline gels by light exposure," *Adv. Mater.* **15**, 201-205 (2003).

[189] White, T. J., Tabiryan, N. V., Serak, S. V., Hrozhyk, U. A., Tondiglia, V. P., Koerner, H., Vaia, R. A. and Bunning, T. J., "A high frequency photodriven polymer oscillator," *Soft Matter* **4**, 1796-1798 (2008).

[190] Kofod, G., Wirges, W., Paajanen, M. and Bauer, S., "Energy minimization for self-organized structure formation and actuation," *Appl. Phys. Lett.* **90**, 081916 (2007).

[191] Luchnikov, V., Sydorenko, O. and Stamm, M., "Self-rolled polymer and composite polymer/metal micro- and nanotubes with patterned inner walls," *Adv. Mater.* **17**, 1177-1182 (2005).

[192] Kelby, T. S., Wang, M. and Huck, W. T. S., "Controlled Folding of 2D Au-Polymer Brush Composites into 3D Microstructures," *Adv. Funct. Mater.* **21**, 652-657 (2011).

[193] He, H. Y., Guan, J. J. and Lee, J. L., "An oral delivery device based on self-folding hydrogels," *J. Control. Release* **110**, 339-346 (2006).

[194] Guan, J. J., He, H. Y., Hansford, D. J. and Lee, L. J., "Self-folding of three-dimensional hydrogel microstructures," *J. Phys. Chem. B* **109**, 23134-23137 (2005).

[195] Bassik, N., Abebe, B. T., Laflin, K. E. and Gracias, D. H., "Photolithographically patterned smart hydrogel based bilayer actuators," *Polymer* **51**, 6093-6098 (2010).

[196] Howse, J. R., Topham, P., Crook, C. J., Gleeson, A. J., Bras, W., Jones, R. a. L. and Ryan, A. J., "Reciprocating power generation in a chemically driven synthetic muscle," *Nano Lett.* **6**, 73-77 (2006).

[197] Py, C., Reverdy, P., Doppler, L., Bico, J., Roman, B. and Baroud, C. N., "Capillary Origami: Spontaneous wrapping of a droplet with an elastic sheet," *Phys. Rev. Lett.* **98**, 156103 (2007).

[198] Bassik, N., Stern, G. M., Jamal, M. and Gracias, D. H., "Patterning Thin Film Mechanical Properties to Drive Assembly of Complex 3D Structures," *Adv. Mater.* **20**, 4760-4764 (2008).

[199] Shah, R. K., Kim, J. W., Agresti, J. J., Weitz, D. A. and Chu, L. Y., "Fabrication of monodisperse thermosensitive microgels and gel capsules in microfluidic devices," *Soft Matter* **4**, 2303-2309 (2008).

[200] Jang, J. H., Jhaveri, S. J., Rasin, B., Koh, C., Ober, C. K. and Thomas, E. L., "Three-dimensionally-patterned submicrometer-scale hydrogel/air networks that offer a new platform for biomedical applications," *Nano Lett.* **8**, 1456-1460 (2008).

[201] Jordan, A., Scholz, R., Wust, P., Fahling, H. and Felix, R., "Magnetic fluid hyperthermia (MFH): Cancer treatment with AC magnetic field induced excitation of biocompatible superparamagnetic nanoparticles," *J. Magn. Magn. Mater.* **201**, 413-419 (1999).

[202] Jordan, A., Scholz, R., Wust, P., Schirra, H., Schiestel, T., Schmidt, H. and Felix, R., "Endocytosis of dextran and silan-coated magnetite nanoparticles and the effect of intracellular hyperthermia on human mammary carcinoma cells in vitro," *J. Magn. Magn. Mater.* **194**, 185-196 (1999).

[203] Guan, J. J., He, H. Y., Lee, L. J. and Hansford, D. J., "Fabrication of particulate reservoir-containing, capsulelike, and self-folding polymer microstructures for drug delivery," *Small* **3**, 412-418 (2007).

[204] Kang, Y., Walish, J. J., Gorishnyy, T. and Thomas, E. L., "Broad-wavelength-range chemically tunable block-copolymer photonic gels," *Nat. Mater.* **6**, 957-960 (2007).

[205] Devaraju, N. S. G. K. and Unger, M. A., "Multilayer soft lithography of perfluoropolyether based elastomer for microfluidic device fabrication," *Lab Chip* **11**, 1962-1967 (2011).

[206] Huang, Y. Y., Castrataro, P., Lee, C. C. and Quake, S. R., "Solvent resistant microfluidic DNA synthesizer," *Lab Chip* **7**, 24-26 (2007).

[207] Truong, T. T., Lin, R. S., Jeon, S., Lee, H. H., Maria, J., Gaur, A., Hua, F., Meinel, I. and Rogers, J. A., "Soft lithography using acryloxy perfluoropolyether composite stamps," *Langmuir* **23**, 2898-2905 (2007).

[208] Niskala, J. R. and You, W., "Metal-Molecule-Metal Junctions via PFPE Assisted Nanotransfer Printing (nTP) onto Self-Assembled Monolayers," *J. Am. Chem. Soc.* **131**, 13202-13203 (2009).

[209] Bong, K. W., Xu, J., Kim, J.-H., Chapin, S. C., Strano, M. S., Gleason, K. K. and Doyle, P. S., "Non-polydimethylsiloxane devices for Oxygen-Free Flow Lithography," *Nat. Commun.* DOI: 10.1038/ncomms1800 (2012).

[210] Liu, K., Ding, H. J., Liu, J., Chen, Y. and Zhao, X. Z., "Shape-controlled production of biodegradable calcium alginate gel microparticles using a novel microfluidic device," *Langmuir* **22**, 9453-9457 (2006).

[211] Yang, Y. L., Motte, S. and Kaufman, L. J., "Pore size variable type I collagen gels and their interaction with glioma cells," *Biomaterials* **31**, 5678-5688 (2010).

[212] Monteiro, O. a. C. and Airoldi, C., "Some studies of crosslinking chitosan-glutaraldehyde interaction in a homogeneous system," *Int. J. Bio. Macromol.* **26**, 119-128 (1999).

[213] Brunel, F., Veron, L., Ladaviere, C., David, L., Domard, A. and Delair, T., "Synthesis and Structural Characterization of Chitosan Nanogels," *Langmuir* **25**, 8935-8943 (2009).

[214] Lv, P. P., Wei, W., Gong, F. L., Zhang, Y. L., Zhao, H. Y., Lei, J. D., Wang, L. Y. and Ma, G. H., "Preparation of Uniformly Sized Chitosan Nanospheres by a Premix Membrane Emulsification Technique," *Ind. Eng. Chem. Res.* **48**, 8819-8828 (2009).

[215] Yang, C. H., Huang, K. S., Lin, P. W. and Lin, Y. C., "Using a cross-flow microfluidic chip and external crosslinking reaction for monodisperse TPP-chitosan microparticles," *Sens. Actuator B-Chem.* **124**, 510-516 (2007).

[216] Shintaku, H., Kuwabara, T., Kawano, S., Suzuki, T., Kanno, I. and Kotera, H., "Micro cell encapsulation and its hydrogel-beads production using microfluidic device," *Microsyst. Technol.* **13**, 951-958 (2007).

[217] Banerjee, A., Nayak, D. and Lahiri, S., "A new method of synthesis of iron doped calcium alginate beads and determination of iron content by radiometric method," *Biochem. Eng. J.* **33**, 260-262 (2007).

[218] Gong, X. Q., Peng, S. L., Wen, W. J., Sheng, P. and Li, W. H., "Design and Fabrication of Magnetically Functionalized Core/Shell Microspheres for Smart Drug Delivery," *Adv. Funct. Mater.* **19**, 292-297 (2009).

[219] Wong, H. L., Wang, M. X., Cheung, P. T., Yao, K. M. and Chan, B. P., "A 3D collagen microsphere culture system for GDNF-secreting HEK293 cells with enhanced protein productivity," *Biomaterials* **28**, 5369-5380 (2007).

[220] Tan, W. H. and Takeuchi, S., "Monodisperse alginate hydrogel microbeads for cell encapsulation," *Adv. Mater.* **19**, 2696-2701 (2007).

[221] Xu, J. H., Li, S. W., Tostado, C., Lan, W. J. and Luo, G. S., "Preparation of monodispersed chitosan microspheres and in situ encapsulation of BSA in a co-axial microfluidic device," *Biomed. Microdevices* **11**, 243-249 (2009).

[222] Yang, C. H., Huang, K. S. and Chang, J. Y., "Manufacturing monodisperse chitosan microparticles containing ampicillin using a microchannel chip," *Biomed. Microdevices* **9**, 253-259 (2007).

[223] Matsunaga, Y. T., Morimoto, Y. and Takeuchi, S., "Molding Cell Beads for Rapid Construction of Macroscopic 3D Tissue Architecture," *Adv. Mater.* **23**, H90-H94 (2011).

[224] Abate, A. R., Poitzsch, A., Hwang, Y., Lee, J., Czerwinska, J. and Weitz, D. A., "Impact of inlet channel geometry on microfluidic drop formation," *Phys. Rev. E* **80**, 026310 (2009).

[225] Gupta, A. and Kumar, R., "Effect of geometry on droplet formation in the squeezing regime in a microfluidic T-junction," *Microfluid. Nanofluid.* **8**, 799-812 (2010).

[226] Shestopalov, I., Tice, J. D. and Ismagilov, R. F., "Multi-step synthesis of nanoparticles performed on millisecond time scale in a microfluidic droplet-based system," *Lab Chip* **4**, 316-321 (2004).

[227] Xu, J. H., Li, S. W., Tan, J., Wang, Y. J. and Luo, G. S., "Preparation of highly monodisperse droplet in a T-junction microfluidic device," *Aiche J.* **52**, 3005-3010 (2006).

[228] Garstecki, P., Fuerstman, M. J., Stone, H. A. and Whitesides, G. M., "Formation of droplets and bubbles in a microfluidic T-junction - scaling and mechanism of break-up," *Lab Chip* **6**, 437-446 (2006).

[229] Christopher, G. F. and Anna, S. L., "Microfluidic methods for generating continuous droplet streams," *J. Phys. D-Appl. Phys.* **40**, R319-R336 (2007).

[230] Dendukuri, D., Tsoi, K., Hatton, T. A. and Doyle, P. S., "Controlled synthesis of nonspherical microparticles using microfluidics," *Langmuir* **21**, 2113-2116 (2005).

[231] Ward, T., Faivre, M., Abkarian, M. and Stone, H. A., "Microfluidic flow focusing: Drop size and scaling in pressure versus flow-rate-driven pumping," *Electrophoresis* **26**, 3716-3724 (2005).